Localization, Sensing, Energy Delivery and Communication in Wirelessly Powered Systems

Yi Zhao

A dissertation
submitted in partial fulfillment of the
requirements for the degree of

Doctor of Philosophy

University of Washington

2016

Reading Committee:

Joshua R. Smith, Chair

Matthew S. Reynolds

Shwetak N. Patel

Program Authorized to Offer Degree:
Electrical Engineering

University of Washington

Abstract

Localization, Sensing, Energy Delivery and Communication in Wirelessly Powered Systems

Yi Zhao

Chair of the Supervisory Committee:
Associate Professor Joshua R. Smith
Computer Science and Engineering, Electrical Engineering

Wirelessly powered sensors are proven as an effective solution for sensing and monitoring in undeveloped, inaccessible environments or where the difficulty of maintaining devices dramatically increases as the network increases in scale [5, 76, 84]. In addition, small low power consumer electronics, such as wearable sensors, are constrained by the properties of their batteries. The use of a battery limits the devices lifetime, size, hardware cost and maintenance effort (charging or replacing the battery). Among the latest battery-free solutions, radio frequency (RF) wireless power is one of the most promising technologies for supplying power, because it not only wirelessly charges passive or semi-passive devices, but also has intrinsic compatibility with existing radio communication systems.

This dissertation will discuss a type of RF wirelessly powered system with extremely constrained available power, that leverages existing infrastructure, such as an RFID reader or a cellphone, for its power source. In general, the power available on these wireless devices is around a few μW to a few mW. However, some applications using these devices require power-hungry computing, sensing or communications, which require much more power than is available from RF harvesting. Therefore, the performance attainable for computation, sensing, and communication is significantly affected by energy harvesting efficiency as well as the duty cycle strategy. This dissertation will use a few application examples to demonstrate how RF energy harvesting efficiency affects the performance of wirelessly powered platforms

using existing infrastructure with regard to localization, sensing and communication. This dissertation categorizes wireless power systems into two types based on the target operation range and available wireless power level. The first type comprises far-field systems whose operating ranges are beyond a few meters and which support harvested power on the order of a few to hundreds of μW. The second type comprises near field systems whose operating ranges are closer than $10cm$, where the available power is greater than a few mW.

The first portion of this thesis addresses the challenges and trade-offs in a far field wirelessly powered sensing system. This dissertation presents a working prototype of an RFID-based system that localizes a custom, battery-free, EPC Gen2-compatible UHF tag, and uses it as an example to discuss the typical features of a far-field system. The presented system detects the 3D position and motion of a battery-free RFID tag incorporating an ultrasound detector and an accelerometer. Combining the tags acceleration with absolute 3D location permits adaptive power management and supports activity recognition. It uses the RFID communication channel for synchronization and inventory, and uses acoustic propagation delays for distance measurement. We characterize the system's localization performance in open space as well as implement it in a smart wet lab application. In the wet lab setting, the system is used to track the real-time location and motion of objects with wireless powered sensing tags, as well as recognize pouring actions performed on the objects to which the tag is attached. This thesis discusses the trade-offs between sensing accuracy, latency, tag power consumption and position.

The second portion of this dissertation presents the NFC-WISP as an example of a typical near-field wireless power system. The NFC-WISP is a programmable, computationally enhanced platform designed to explore new near field battery-free sensing and user interface applications. Not only is the NFC-WISP be wirelessly powered and read by commercially available RFID readers (including NFC-enabled smart phones), but the harvested wireless power is sufficient to power external power hungry sensors and peripherals such as an ac-

tive bistable matrix E-ink display. Firstly, we illustrate possible applications which use the NFC-WISP as a passive display tag, such as a battery-assisted perishable goods temperature display, and a motion monitor with wireless charging features. Secondly, this dissertation discusses how to improve the communication and power harvesting efficiencies by varying the number and the quality factor (Q) of receiver coils. A revision of NFC-WISP is demonstrated with improved communication and energy harvesting performance. Finally, this dissertation discusses how to choose antenna designs to meet the requirements of different systems.

TABLE OF CONTENTS

LIST OF FIGURES

GLOSSARY

IOT: Internet of Things

AI: Artificial Intelligence

ID: Identification data

EPC: Electronic Product Code

TOA: Time of Arrival

TOF: Time of Flight

EPC: Electronic Product Code

RFID: Radio Frequency Identification

NFC: Near Field Communication

PDL: Power delivery to the load

PTE: Power transfer efficiency

NFC-WISP: Near Field Communication Wireless Identification and Sensing Platform, which is a sensing, display and computational enhanced NFC card

UHF-WISP/WISP: Wireless Identification and Sensing Platform using Ultra High Frequency band (915MHz) and is compatible with UHF EPC Gen2 communication standard

ACKNOWLEDGMENTS

The author wishes to express sincere appreciation to everyone in Sensor Systems Lab at University of Washington, where she has had the opportunity to work with the world best researchers and greaduate students like Aaron Parks, Alanson Sample, Vamsi talla, Joshua Smith, Brody Mahoney, Ben Waters, Saman Naderiparizi, James Younguist, Vaishnavi Ranganathan, Zerina Kapetanovic, Artem Dementyev, Liangting Jiang, Xingyi Shi, Greogry More and Patrick Lancaster.

DEDICATION

to my husband , Cifeng Fang, and my family

Chapter 1

INTRODUCTION

1.1 Background

1.1.1 Motivation

The technology which can offer advanced connectivity of physical objects, devices and systems to enable a variety of applications is the initial concept of "Internet of Things" (IoT), which has been discussed as early as 1982 [89]. The nodes of Internet of Things network can either be small electronic devices, like cell phone and smart watch, or non-electrical physical objects, like our clothes, food, office supplies or fashion accessories. If everything we have seen in the physical world can be detected, monitored and managed through an individual network, then a variety of smart applications in both industry (like medical, retail, apparel, logistic, etc.) and our daily life can be enabled. For example, in cold chain management, the ability to track and monitor the temperature of each product can help improve its product delivery efficiency as well as ensure its product quality. In addition, the ability to fully monitor and sense physical objects can help people schedule or manipulate their daily tasks automatically (like finding the keys, automatically generate a shopping list based on detected food storage or expired items).

However, to make that happen, we need to have full knowledge of both people and the physical object. People can be tracked and sensed by more and more available wearable devices or smartphones. However, the technology used to monitor and detect the non-electrical "things" is not well explored yet. In general, it mainly requires three steps to monitor the physical world (we use nodes to represent the target physical objects in Internet of Things network).

a.Connectivity To identify and to connect physical nodes with electronic devices and system in a network.

b.Sensing & Interaction To detect the information related to the physical nodes by sensing itself or its environment (use the nodes as input to the network) or control the objects to better interactive with other nodes, devices or human beings (use the nodes as an output of the network).

c.Integration To integrate communication, sensing and interaction of the nodes into the IoT network and utilize sensor fusion or Artificial Intelligence(AI) technology to build high-level applications.

1.1.2 Existing technology

The network to connect things

The connection between devices and systems can be achieved by using the advanced wireless network such as Wi-Fi, bluetooth or zig-bee(Figure 1.1). However, to connect the physical objects, we may encounter lots of limitations introduced by the large quantity(Figure 1.2), unit cost, size, lifetime and system maintenance effort(such as replacing or charging the battery). A traditional approach is to attach a small, low unit cost device, such as bar-code or Radio Frequency Identification(RFID) /Near Field Communication(NFC) tags to each object and to connect all the objects by reading the devices. In general, in comparison with bar-code, which has limited data size, reading range, and speed, RFID and NFC offer better performance. However none of them have sensing and interaction capabilities.

RFID technology (including NFC) is a modern wireless identification technology which is widely used in inventory management, automatic toll system or access control. Each UHF RFID/NFC tag contains a few kilobytes hard-coded ID data. Based on the operation range and protocol, the RFID technology has mainly two categories, UHF RFID (915MHz) and NFC (13.56MHz). Typically, multiple UHF RFID tags can be accessed together by a nearby

UHF RFID reader at a range(Figure 1.1) up to 10m; a single NFC tag can exchange data or ID information with an NFC reader in its proximity within 10cm. Both the UHF RFID and NFC tag can collect energy from the interrogating radio waves or magnetic waves generated by the reader. Therefore most of them are entirely passive (battery-free). Some of them may use the battery for assisting its reading at a larger range. Another unique feature of UHF RFID / NFC technology is that it uses a ultra-low power communication technology called "backscatter" or "load modulation" to send data back to the reader (tag-to-reader up-link) by modulating its reflecting electrical/magnetic field.

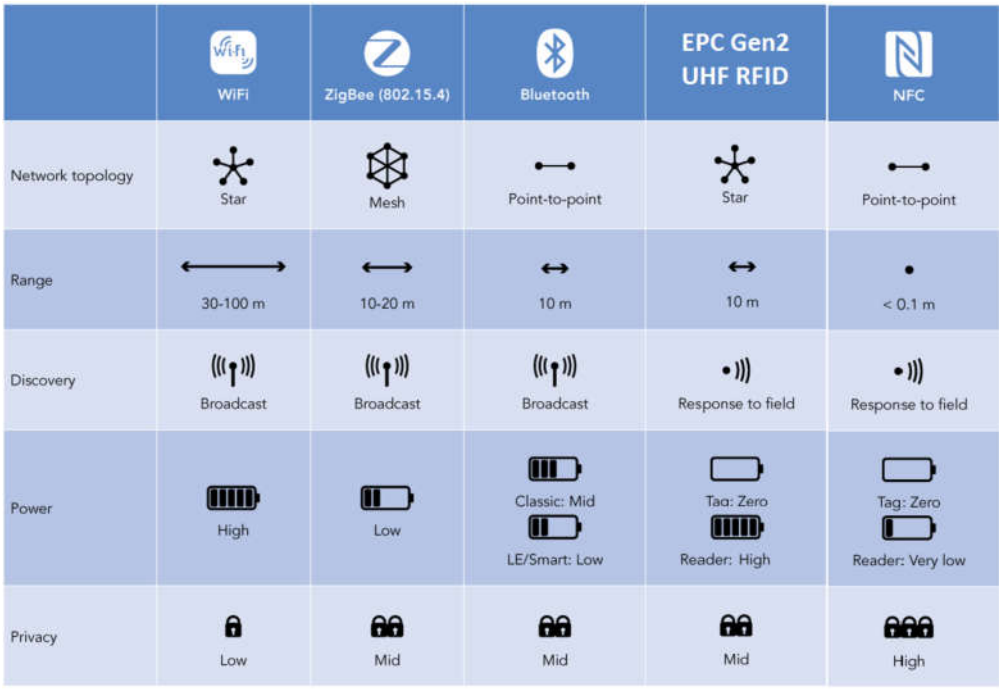

Figure 1.1: Overview of current indoor network system (modified from [25])

Overall, the UHF RFID/NFC tag's hardware architecture is simple, small and requires low power, thereby reducing the total equipment cost. Those three unique features enable its potential to be the ideal device to connect non-electrical "things" in a low-power low-cost way. However, its low-cost and low-power feature is traded by the reduction of communication

data rate and operating range when comparing to other radio systems (See Figures 1.1 and 1.3). Traditionally, RFID tags are only used to send its ID to the readers to build up the connectivity between "things" to the access point in the network (the first step mentioned above) without sensing and interaction capability.

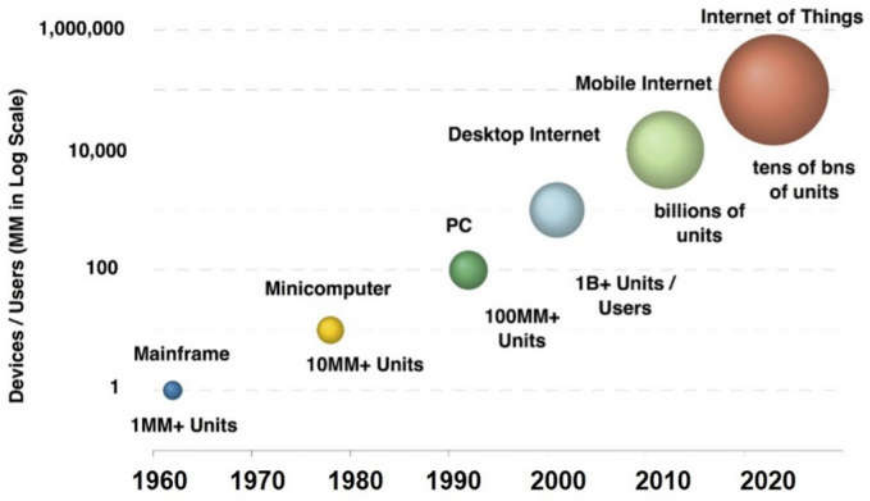

Figure 1.2: Scale of Network Devices, source: Silicon Labs. Thomson Reuters, Morgan Stanley

The technology to sense and interact with things

Battery-powered wireless sensors are traditionally designed to monitor surrounding environment and distribute objects for industrial, agricultural and medical applications [81,85]. The use of battery can enable low-power dedicate sensing, high speed computing and communication when the size, unit cost, lifetime and maintenance effort can be ignored by certain applications. However, for some applications, such as book localization and cold chain management, the target "things" are small, cheap and in large quantity, the use of battery will be a big limitation in term of device size, lifetime, maintenance effort(change or charge the battery) and unit cost.

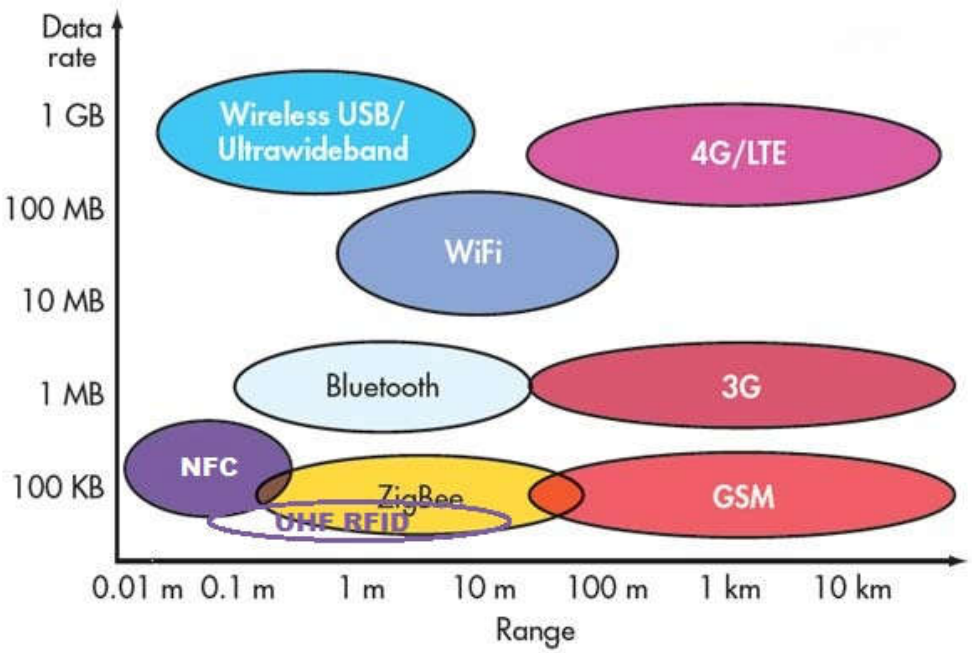

Figure 1.3: A map of data rate and range of modern radio networks (modified from [25])

The energy harvesting technology to power the devices on things

Energy harvesting or scavenging technology can harvest energy from radio waves, vibration, thermal and light [35,46], it can provide a potential energy solution to eliminate the limitation of the battery used by wireless sensors. A system with energy harvester uses a different kind of transducer to convert another type of energy into electrical AC signal and then use AC-to-DC converter(rectifier) to convert AC energy into DC to power rest of the system.

The ideal system

In summary, the RFID/Near Field Communicationtags are the best network to connect physical objects; the wireless sensors can sense and monitor things. The energy harvesting technology can provide power without using the battery. Therefore, in the author's opinion, a system which integrates all the three parts mentioned above can be the best solution to

connect and sense a large quantity of the "Things". This kind of system is called wireless-powered identification and sensing system here, in which a battery-free device is attached on each objects to track and sense the objects and a RFID reader (including NFC reader) is used to retrieve information from different battery-free devices to the other system. In general, the device is self-powered by RF or magnetic wave sent by RFID reader, it is small in size and has low unit cost, infinite lifetime and nearly no maintenance efforts. In this thesis, the author designs two types of wirelessly powered identification and sensing systems for different applications in two distinct use cases to study the relationship amount the performance of power-hungry tasks (like localization or updating display), energy delivery and communication.

1.2 Research Scope

Unlike other wireless sensing systems, the traditional RFID technology has two distinct use cases mentioned above. They are UHF RFID and NFC, which use different energy harvesting mechanism, operation range, and communication protocol. The UHF RFID's operation range is far longer than its wavelength, therefore it's a far-field system, the NFC tag's operation range is far shorter than its wavelength, therefore it's a near-field system. Their unique features are described as follows:

- Far-field UHF RFID: this technology currently uses Ultra High Frequency (UHF) band radio wave (around $915MHz$) to transfer data and power tiny electrical tags for automatically identifying and tracking the tags attached to the objects [91]. This type of system is targeting for reading range larger than $1m$ (see Figures 1.1 and 1.3).

- Near Field Communication (NFC): the power delivery and communication in NFC systems does not rely on radio waves like what the far field RFID system does. It operates at a reading distance of $10cm$ or less [90]. Current NFC system uses 13.56MHz signal in Industrial Scientific and Medical(ISM) band for delivering power and communication

[90] (see Figures 1.1 and 1.3). Besides, those type of system can provide better privacy and more power because of its reading range.

1.2.1 Far field system

There is a well-known far field wireless identification sensing devices (called WISP) which was first introduced in 2005 [47]. It is a software defined passive UHF RFID tag which is compatible with EPC Gen2 RFID protocol and has the sensing capability (this WISP will be called UHF WISP in this thesis). A variety of low power sensors has been added into the WISP to enable different kinds of sensing applications, like temperature sensing, acceleration sensing and touch sensing, etc [58, 61, 92]. However, those sensing tasks may only require a few tens of μW power. A more power hungry sensing task other than simple ADC sampled sensing hasn't been explored yet.

The ability to precisely localize objects with high-speed and low-cost tags are desirable for applications such as inventory, asset tracking and robotic manipulation of tagged items. However, the existing system either can only localize objects precisely using battery-powered devices (like [48]) or localize small objects less accurately([42]) and slowly [83] when using battery-less devices like UHF RFID. Therefore, the author proposes to design a battery-free, low-cost, high-speed localization system base on the UHF WISP and existing RFID infrastructure, and then combine the location and other sensing information, like motion, to accomplish one example of Internet of Thing application - objects' activity tracking. The location sensing consumes more power than traditional sensing tasks and its performance is significantly affected by the delivered power, which is a typical problem for most of the wireless power sensor system. Therefore, a discussion about the trade-off between performance and power is also presented in the thesis.

1.2.2 Near field system

In NFC system, the power harvesting efficiency can be very efficient when comparing to the far-field system, but its power transmission and communication distance is limited within a

few centimeters. However, the traditional NFC system mainly focuses on exchanging identification data by tapping NFC tag to the reader. Nowadays, the NFC reader is ubiquitous due to the booming NFC-enabled smartphone market. It will have more sensing and research opportunity using NFC technology as sensing and human to computer interaction media. However, to customize an NFC chip for sensing or other application is very time-consuming and of high cost. The later work of the thesis is to design a software defined NFC platform (similar like UHF WISP) with sensing and more power hungry computation capability, pushing the existing NFC technology towards a new edge with more universal sensing and human to computer interaction enabled. This work is published and open-sourced online [1]. The future work will focus on researching the relationship amount the power-hungry tasks, energy harvesting performance and communication performance.

1.3 Dissertation Organization

This dissertation is organized as follows:

Chapter 2 will introduce the motivation and design of a far field wireless powered localization system. A primary design and four sets of experiments will be presented, followed by their performance analysis. Then I'll discuss the system performance and limitation. Finally, an illustration of an application on motion sensing will be demonstrated.

Chapter 3 will describe a near field wireless powered software defined Near Field Communication(NFC) platform. It is a sensing and computationally enhanced platform designed to explore new NFC sensing and user interface applications. Three applications using this platform will be demonstrated. An analysis of the system performance and limitation will be discussed.

Chapter 4 will present a simulation work to analyze performance and trade-offs of two possible antenna configurations in an NFC-powered system: 2-coil and 3-coil. Also, the influence of parasitic capacitance effect in both system and cross coupling effect in 3-coil system is simulated. Finally, a detuning method is present to compensate the frequency shifting effect due to those parasitic effects to optimize power delivery efficiency.

Chapter 5 will present a simulation and implementation analysis of a 2-coil or 3-coil NFC wireless power system. In practice, the load impedance of near field wirelessly powered platform changes with a different run-time process. This chapter illustrates the simulation result of each process regarding power delivery to the load and communication. In addition, this chapter implements the switchable antenna method in a revision of NFC-WISP hardware, in which the receiver antenna can be switched between the single coil (the entire system will be 2-coil system) and two coils (the entire system will be 3-coil system) along with the changes of process in run-time to deliver more power and enhance communication in a wider range.

Chapter 2

FAR FIELD - A BATTERY-FREE OBJECT LOCALIZATION AND MOTION SENSING PLATFORM

2.1 Introduction

2.1.1 Motivation

Outdoor localization technologies have enabled a diversity of influential location-aware applications. One of the most dominant localization systems is GPS, which enables locating mobile objects outdoors with meter-scale accuracy. However, due to the complexity of indoor environments, navigation systems that perform well outdoors often work poorly indoors [80].

Considering the range required for indoor localization system, which is around 1-5 meters for room level localization or 5-20 meters for floor level localization, wireless sensor networks [80] is widely explored in indoor localization area. Accurate 3D object location in room level is one of the key context information enabling many smart home and smart office capabilities, such as activity inference, asset tracking, and robot navigation or physical object-to-computer interaction. Most current indoor localization systems are based on either cameras [94] , battery-powered distributed sensing devices [42,48] or battery-free RFID tags.

Camera-based systems create a host of privacy issues and have trouble localizing transparent, reflective and irregular-shape objects. The battery-powered systems typically have better accuracy and identification ability, but don't scale well due to tag size, battery life and monetary and maintenance costs of the active sensors, especially in dense localization sensor network. The current state-of-art battery-free RFID localization can provide sub-meter level coarse localization using RF Signal Strength(RSSI) [68,95] or RF phase [83]. However, most of them [80] are either strongly affected by RF multi-path effects, which limits its accuracy or have to trade position update rate (such as [83]) for improving accuracy by using multiple

readers, reference tags and computing expensive algorithm. Those limitation constrains their implement in some scenario when high update rate or high accuracy is needed.

This work design a battery-free localization system with high accuracy and high update rate using wireless powered sensing tag in order to provide a low cost, high efficent solution for those applications which require less maintanance effort, small and cheap infrastrucutre and high accuracy and update rate.

2.1.2 The performance of exising systems

Most indoor localization systems work by sensing quantities that change with the position of the object. Radio Frequency (RF) signals [42,83], sound waves [48], optical signals [54] or magnetic fields [12] have been used to determine location. By measuring the distance of the object to three or more known reference points, the object position can be estimated.

One appealing RF-based approach is to add localization to existing RFID technology [68, 95]. RFID has readily available infrastructure, low-cost tags, and identification capabilities. However, RFID localization systems based on Received Signal Strength (RSSI) [80] are strongly affected by RF multi-path effects; these effects limit accuracy to meters. Some systems (such as LANDMARC [42,83]) improve accuracy by using multiple readers, reference tags and computing expensive algorithm. However, this increases system cost and time for data analysis, which may be a challenge for high-speed mobile position-aware applications.

Generally, acoustic localization systems have better accuracy than RF-based systems, because it is straightforward to make time of flight measurements on slowly propagating acoustic signals, while distance estimates using RF signals must typically be made via less accurate amplitude (RSSI) measurements. Acoustic systems use Time of Arrival (ToA), Time Difference of Arrival (TDoA) [48] or Angle of Arrival (AoA) [52], and have reported localization accuracies on the order of 1cm. A key shortcoming of existing acoustic systems, however, is their use of batteries, which results in sensor nodes with large size and weight as well as limited lifetimes. Some acoustic systems [48] require the acoustic source to transmit to the receiver node the time that its signal originated; in our system, RFID events provide

synchronization, no transmission of the time of the origination of the ultrasound pulses is needed. Some systems measure acoustic round trip time; RFID synchronization allows us to measure distances using just reader-to-tag measurements. The use of a single timing measurement results in a system that is faster and lower power than systems based on round trip acoustic propagation.

2.1.3 Comparison with prior work

In this work, the author aim to combine the best features of acoustic localization (high precision and technical simplicity) with the best features of RFID-based localization (absence of batteries, unlimited lifetime, light weight, small size, unique identification of tags, as well as compatibility with existing RFID infrastructure). This paper introduces the first battery-free acoustic localization platform based on RFID infrastructure.

Firsly, we will demonstrated that a passive RFID tag augmented with an ultrasonic microphone can accurately estimate its range from three or four ultrasonic transmitter [99], the three or four ultrasonic transmitters were built-into single fully-programmable passive tags (Figure 2.3) named WISPs (Wireless Identification Battery-free Sensing Platform [59]). Thoese two type of tags were augmented with either ultrasound beacons or ultrasound microphones and accelerometers. By having all of the ultrasonic sensing and actuation in a tag, we can make use of commercial RFID readers for power and communication. In this thesis, we will show that this basic acoustic ranging capability can be extended to robust, accurate 3D localization in a lab environment. We do this by having tags perform ultrasound time of flight (ToF) measurements to estimate its range to four ultrasonic transmitters in known locations. These ranging estimates infer the tag's 3D location relative to the transmitters by applying a transliteration method that can mitigate the effect of indirect-path and multi-path acoustic reflections. The result is a scalable, battery-free 3D localization system with the following features:

- $1.9cm$ minimal accuracy overall with $(3.1, 5, 1.9)cm$ accuracy for each (x,y,z) axis for

Table 2.1: COMPARISON OF RFID AND ACOUSTIC LOCALIZATION.

Technology	**System**	**Method**	**Accuracy**	**Feature**
Active RFID	WhereNet [95]	TDoA	2-3 m	Uniquely identifies equipment; Battery-powered tags
	LANDMARC [42]	RSSI	1-18m	Extra active reference tags and multiple readers; Battery-powered tags
Passive RFID	Multifrequency [10]	Phase	80cm@4m	Walls cause errors; system performs much better with no multipath
	Phase [83]	*Phase*	11cm	2D, Use software defineded reader; expensive computing, low update rate
Ultrasound	Active Bat [95]	ToA	3 cm	Subject to reflections by obstacles; Multiple receivers; Battery-powered sensor nodes
Ultrasound + RF	Cricket [48]	TDoA	10 cm	High accuracy; long range; privacy sensitive; Battery-powered tags
RFID + Ultrasound	This work	ToA	min 1.9 cm	3D, Battery-free; RFID-compatible; Combine with accelerometer

line of sight stationary tags.

- 1.5cm presition on distance measurement
- Average update rate of 15 3D location estimates per second (given 1W RF power and 1.8m test range).
- Maximum range of 3.5m (at best orientation for RF sensitivity).
- 252 μJ Energy consumption for positioned tag updating one location measurement.
- Tolerance to ultrasound echo noise.
- Wireless powered acoustic transmitters and target tag that allow more freedom for system set-up.
- Accelerometer data which accompanies location estimates. This enables both motion and activity estimation as well as improves tag's power management

Table 2.1 compares our system to a representative collection of previous localization systems.

2.2 System Overview

Our system is designed to allow a customized RFID tag to detect the time of flight (ToF) or time of arrival (ToA) of ultrasound sent from four ultrasound transmitters. Besides, other sensor data like 3-axis acceleration data can also be measured on each tag to enable other application or locations aware activity tracking. All the tag in this work is a programmable EPC Gen2 UHF tags(WISP) [59].The target tag sends back all detected sensor results back to an commercial RFID reader using its Electronic Product Code (EPC) (tag's ID). Finally, the RFID reader reports all tag readings to a client to compute the tag-to-transmitter distance ranges, and from that estimate the tag's final 3D location and motion state. The basic

system is comprised of three types of hardware components: Sense WISP (Or WISP Rx) which attached to the objects to be localized or sensed, SPY WISP (or WISP Tx) which sends ultrasonic beacons from known locations and a RFID reader which powers the WISPs and coordinate communication(see Figures 2.1 and 2.4).

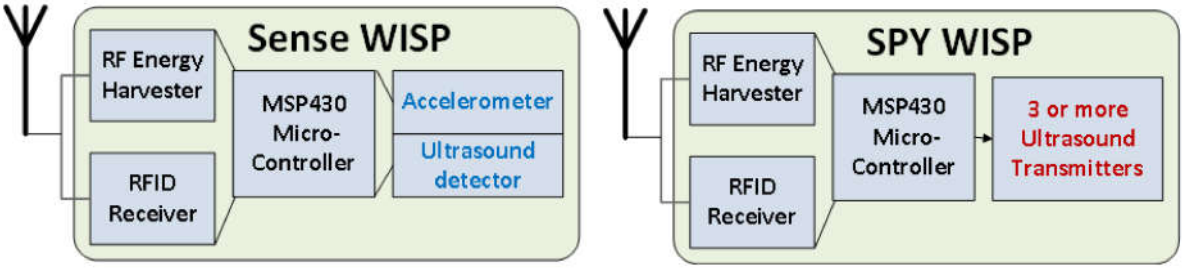

Figure 2.1: Architecture of the Sense WISP (WISP Rx) and the Spy WISP (WISP Tx)

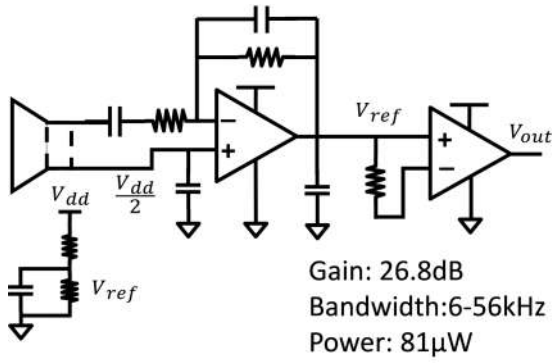

Figure 2.2: 25kHz ultrasound tone detector

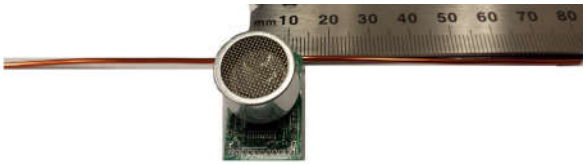

Figure 2.3: Sense WSIP (WISP Rx)

2.2.1 Sense WISP(or WISP Rx)

Objects to be located are tagged with Sense WISPs (equivalent to WISP Rx in some figure). These are battery-free programmable RFID tags (Figure 2.3) augmented with an ultrasound detector and 3D accelerometer. Location is ultimately calculated by measuring the flight

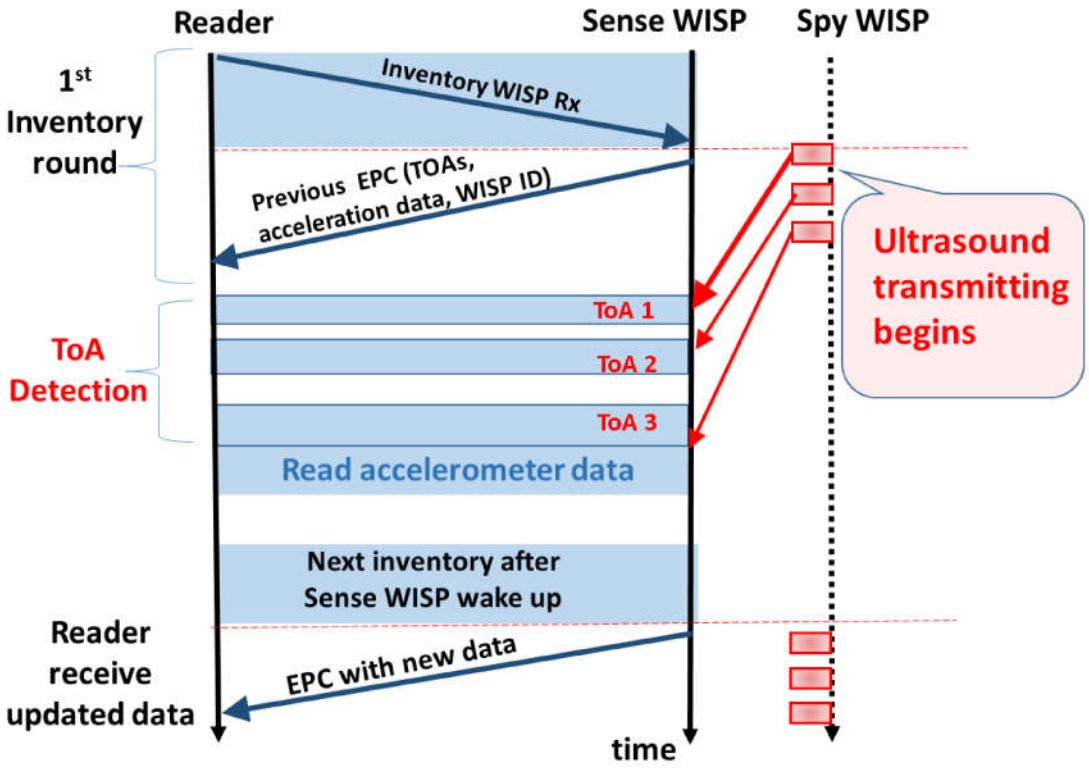

Figure 2.4: Sensing and communication protocol: in the blue area, the Sense WISP is awake; in the white region, it asleep.

time of ultrasonic pulses sent by the Spy WISPs described in the next subsection. Sense WISPs are compatible with RFID UHF EPC Gen2 protocol and are wireless powered by $1W$ RF signals sent from a nearby RFID reader antenna.

The battery-free Sense WISP (or WISP Rx) is integrated with 25 kHz ultrasonic tone detector (see Figures 2.2 and 2.3). The WISP tag harvests energy sending from a RFID reader's antenna during RFID inventory, the harvested power on WISPs ranges from a few ten to hundreds of micro-watts and is used for additional sensing and computation. Due to the limited available power on WISPs, the WISP's firmware is optimized for low power measurement of the ToA of ultrasound signal. The acoustic detection on this tag which

consumes most of the harvested power. The minimum detected Sound Pressure Level (SPL) of the detector is about 71.59 dB with power consumption of 80 μW.

During the step of the RFID protocol called the "Inventory Round", the Sense WISP starts a timer in anticipation of the first ultrasound pulse being simultaneously sent from the Spy WISP. This allows the measurement of the time of flight of all four ultrasound signals that are sent. Time-division multiplexing is used to schedule the ultrasound transmissions within each RFID inventory round. To avoid interference between ultrasound signals from different emitters in different RFID reading rounds, the Spy WISP confines all of its ultrasound signals to a 10 ms window. This is the minimum "inventory period" needed by the RFID reader to update one Sense WISP EPC reading. The intervals between ultrasound pulses are chosen to be long enough that ultrasound collisions cannot occur (details will explains in the following session or can be found [99]). After measuring the ultrasound TOF, the Sense WISP samples its 3D acceleration and send all the data back to the reader. The data encodes TOF to all 4 beacons, 3D acceleration and the tag's unique ID (that is the Electronic Product Code (EPC))(Figure 2.4). The accelerometer in the Sense WISP has built-in activity and inactivity detection circuitry and can measure up to $\pm 2G$ with $16mG$ sensitivity.

2.2.2 Spy WISP (or WISP Tx)

The Spy WISP is in many ways like the Sense WISP: It is also a passive RFID tag and can understand and follow the EPC protocol. Unlike the Sense WISP, however, the Spy WISP tag does not acknowledge any radio responses to the RFID reader, nor does it perform any sensing. Instead, the Spy WISP is equipped with 3 or more ultrasonic beacons(more beacons can improve the detection accuracy). The beacons we used is a 25kHZ narrow band ultrasound beacons placed in known locations. The Spy WISP's function is to transmit an ultrasonic pulse from each beacons at a time known to the Sense WISP (Figure 2.4). The Spy WISP synchronizes with the Sense WISP by listening for information in the RFID protocol inventory round. The details of our synchronization method will be discuss later [99]. In a

brief, both the Sense WISP and Spy WISP listen for the start of the "Inventory Round" of the EPC protocol. On observing the signal, the Spy WISP emits a sequence of ultrasound pulses at known intervals. The Sense WISP using this signal to start a timer and being listening for the ultrasonic chips. Since the EPC protocol signals are sent via radio, both tags will receive and recognize the signal at the nearly the same time and from the perspective of acoustic wave speeds, any difference is negligible. Since the Spy WISP does not send any radio replies, it does not interfere with any tags replying to the reader's read requests. As it turns out, the transmission of ultrasound makes the Spy WISP more power hungry than Sense WISP, thus it has to be placed within 1 m of the RFID antenna. The result, however, is an extremely flexible system with mobile, battery-free tags along with a small number of battery and wire-free reference tags to be placed in the environment, independent from the reader.

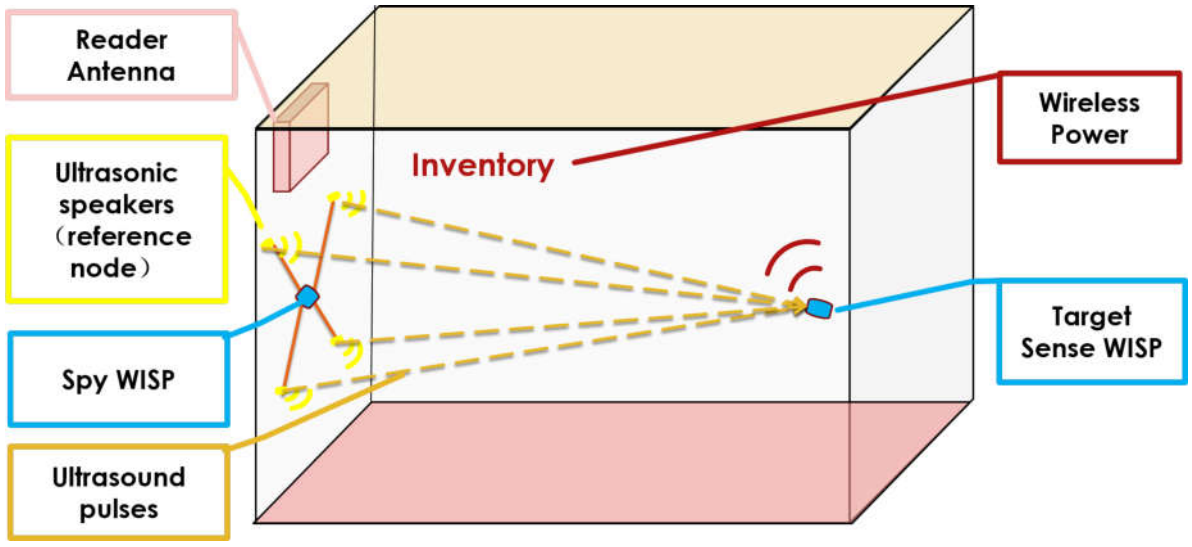

Figure 2.5: Demonstration of battery-free localization system using RFID reader

2.2.3 RFID Reader and Client Application

We use an commercial Impinj EPC Gen2 UHF reader to power and communicate with the Sense and Spy WISPs.Sending inventory commands trigger the acoustic transmission from transmitters in the Spy WISP and measurement of the ToF by the Sense WISPs. In response, a Sense WISP will backscatter to reader its EPC information (include Sense WISP ID, 4 ToA measurement results, 3 axis acceleration data, and motion activity state from previous inventory round) (Figure 2.4), which is used for inferring tag's location and motion state.

A python based RFID localization application GUI is designed to real time process the data and calibrate the 3D localization of target Sense tag and to visualize real time tag tracking result(Figure 2.6). (The GUI uses a python reader client packages from [51]).

2.3 3D Location Measurement Method

2.3.1 Measurement of ToA

To simply the explanation, we bypass the acceleration sample and only use 3 ultrasound beacons to illustration the ToA measurement, and the WISP Rx/Tx will be used instead of Sense WISP and Spy WISP for better demonstration. In general, the WISP Rx is used to detect ultrasonic time of arrival (ToA), the WISP Tx works as a spy to eavesdrop on the communication between the RFID reader and the WISP Rx and emits ultrasound pulses in sequence with known intervals at special RFID events. Because these RFID events are approximately synchronous in both WISP Rx and the WISP Tx, the ToE (Time of Emitting) ultrasonic signal is therefore synchronized. In this way, the power used for actively sending timing information is saved as well. The function of sending back its EPC to the reader is disabled in the WISP Tx, but its duration is reserved to allow ultrasound transmission after the WISP Rx finishes its transmission of its Electronic Product Code (EPC). In this way, the WISP Tx does not interfere with the reader's reading activity, which varies with the tag population.

Figure 2.7 demonstrates how our system receives a packet of ToA data through the

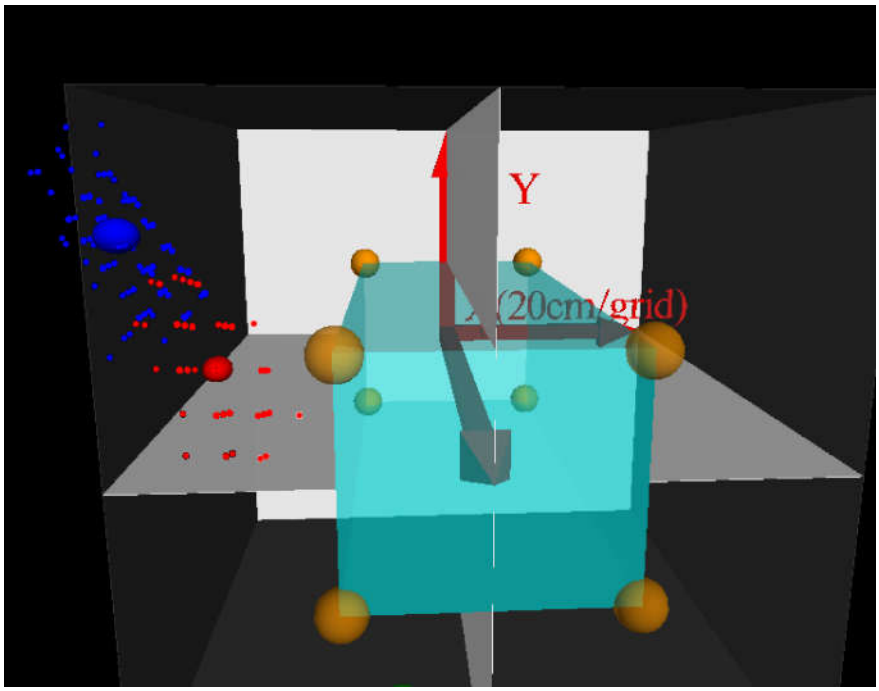

Figure 2.6: A python GUI to process and visualize real time tag 3D localization results: RFID reader's antenna is placed behind the Spy WISP, which is place at the XY plane; the gold ball is the projection of 4 transmitters or them self, those transmitters are centered at the origin and are placed in XY plane facing to Z axis, the cyan colored area is the projection of 4 ultrasonic transmiters; the blue and red dots are detected 2 target tag, size of the blue and red sphere represent its standard deviation of localization result in each axis

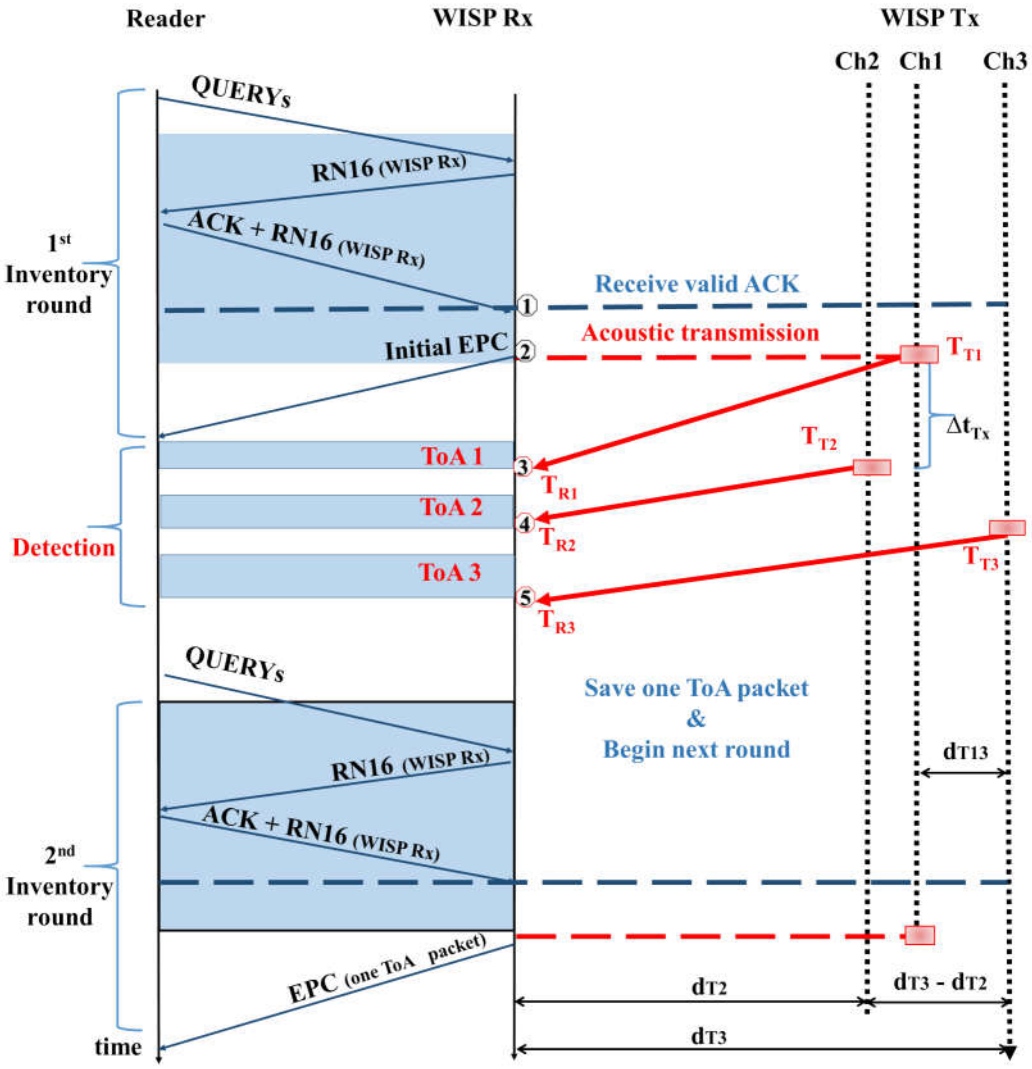

Figure 2.7: Measurement procedure for one ToA packet (3 ToA values), used for computing $d_{T1} - d_{T3}$ in Figure 3. The blue area (left side) under the "WISP Rx" label represents periods when the WISP is active. The red box (right) under the "WISP Tx" label indicates ultrasound transmission events.

RFID protocol. The RFID reader begins sending QUERY, QUERY ADJUST or QUERY REP commands (QUERYs) in order to detect a readable tag at the beginning of an inventory round. Generally, if a tag inside the RF field is ready to respond to the reader, it back-scatters a random 16-bit number RN16 to mark the inventory link between the reader and the tag. In order to synchronize the WISP Rx and the WISP Tx, we assign a special RN16 to WISP Rx and hard-code that RN16 inside WISP Rx's firmware. According to the EPC protocol, when a reader is ready to read the EPC code (the ID code of a RFID tag in EPC Gen2 RFID protocol) from a tag after receiving the tag's RN16, it will issue an Acknowledgment (ACK) command with the same RN16 to the tag (① in Figure 2.7). Typically, only the tag that initiates this RN16 will respond to this ACK by back-scattering its EPC code. However, in our system, the WISP Tx will not directly reply to any inventory commands issued by the reader as the WISP Rx does, instead, the WISP Tx just monitors its nearby RF field, parses detected reader command and triggers ultrasound transmission. Because the RFID related firmware and hardware in both WISP Tx and WISP Rx are similar, the time difference of receiving and processing RF signal between WISP Tx and WISP Rx is ignorable compared to the slower ultrasound propagation. That means the WISP Rx and Tx can almost detect reader's commands, change their RFID-related states at the same time if they are both powered on and thereby synchronizing each other with the RFID events. If the WISP Tx detects a valid ACK command (ACK with WISP Rx marked RN16), the WISP Tx and WISP Rx will process it at the same time (see ① in Figure 2.7). Notes that it is possible that the WISP Rx misses the valid ACK while WISP Tx responds to it, however it will not impact the acoustic detection since the ultrasound detection is only enabled when WISP RX successfully process valid ACK. Compared to other acoustic localization systems [48, 80], our system do not need to actively send timing information to either acoustic receiver or transmitter for synchronization, therefore reducing power consumption and error caused by synchronizing acoustic signal. Plus, both WISP RX and WISP Tx is battery-free. The WISP Tx will transmit ultrasound signal at time $T_{Ti}(i = 1 - 3)$ (i.e. the transmission time (ToE)), which begins at time ② with interval Δt_{Tx} in Figure 2.7. The time ② is one RFID state of WISP

Rx in which the WISP Rx finishes back-scattering its EPC code to the reader. Notes that with known coordinates of three ultrasonic transmitters and the maximum reading range of the WISP tags, the transmission intervals Δt_{Tx} are set to ensure no acoustic signal collisions. In addition, to reduce the power consumption of WISP Rx, the WISP Rx is set to be duty cycled (sleep period is shown between blue area on the left in Figure 2.7). The design of ultrasound emitting interval Δt_{Tx} and the sleep intervals t_{sleep} of WISP Rx during acoustic related events depends on the location of acoustic transmitters, and is explained below:

If d_{Tij} indicates to the space between two transmitters i and j ($i, j \in [1, 2, 3]$ in Figure 2.7) and t_{Tij} is the ultrasound time of flight given distance d_{Tij} (see 2.3), from Figure 2.7, we can see that d_{Ti} refers to the distance between the WISP Rx and transmitter i, and we use $t_{\Delta Tij}$ to represent the time difference of ultrasound propagation between distance d_{Ti} and d_{Tj} (2.2). Generally, the WISP Rx will not be placed in between any two of the transmitters i,j, then because of the trigonometric conditions, it can be easily proven that:

$$|d_{Ti} - d_{Tj}| \leqslant d_{Tij} \tag{2.1}$$

$$t_{\Delta Tij} = |d_{Ti} - d_{Tj}|/v_{sound} \tag{2.2}$$

$$t_{Tij} = d_{Tij}/v_{sound} \tag{2.3}$$

therefore:

$$t_{\Delta Tij} \leq t_{Tij} \tag{2.4}$$

If we set the ultrasound transmission interval Δt_{Tx} larger than $max(t_{\Delta Tij})$, then no two emitted signals will arrive at the WISP Rx at the same time. Similarly, in the WISP Rx, if the interval between each arrival of ultrasound signal is $t_{R_{ij}} = |T_{Ri} - T_{Rj}|$ shown in Figure 2.7, then based on trigonometric conditions, it can be proven that $t_{R_{ij}} \geq -d_{Txij}/v_{sound} + \Delta t_{Tx}$. Since the Δt_{Tx} and the location of acoustic transmitters are pre-configured, the detection

sleep interval should be less than $t_{R_{ij}}$ in order to minimize the time which the WISP Rx spends on waiting for all the ultrasound arriving. Because of the intervals' setting mentioned above, the relative location of each transmitter will limit the timings of ultrasound transmission and detection and thereby affecting the latency of the system. After successfully detecting all three ToA data $T_{Ri}(i = 1, 2, 3)$, the WISP Rx will store them as one packet in its memory and then back-scatter it to the reader in the next inventory round (see in Figure 2.7) if the WISP Rx doesn't power-off. Note that if the WISP Rx can continuously powered on with sufficient power, it then can update the previous stored packet of ToA to the reader and measure new one at each sequential inventory round until powers off.

2.3.2 3D Location Calibration

If the reader obtain one packet of ToA from the without any detection time-out, then we say the reader receives one valid packet of ToA. In general, the time of arrival of ultrasound signals in a given environment is linearly proportional to the distance it propagated. The acoustic transmitter-to-WISP Rx distance d_{Ti} (see Figure 2.7) can then be computed using the speed of sound. However, due to the influence of environmental factors, such as temperature and humidity on sound speed, the ignored RF propagation and processing delay between the WISP Rx and the WISP Tx and the acoustic detecting delay caused by the analog detector, ToA measurement results may have some offset. So in order to improve the system accuracy, we use a first order polynomial line fit model to matching d_{Ti} and T_{Ri}. The line fit model is pre-trained by several tested data with known location and can be expressed as $d_{Ti} = a_i \times T_{Ri} + bi(i = 1, 2, 3)$. Using this model, the small RF synchronization offset and Sense WISP detection clock offset can be modeled in b_i, and the speed of sound variance can be modeled in a_i. After that, we can calculate the position of Sense WISP with these calculated distances d_{Ti} and transmitter position(x_i, y_i, z_i) using a trilateration algorithm [50]. Additionally, a time and tag's motion weighted Kalman filter is used to filter out measurement and environmental noise. A python based RFID localization application GUI allows us to visualize real time tag tracking result (Figure 2.6). (The GUI uses a python

reader client packages from [51]).

2.4 Distance Measurement Performance

To characterize the system, we totally conducted four sets of experiments in a typical lab/office environment, the first two experiments is talked in this section is design to study the relationship between wireless power and distance measurement. Different than other system, the biggest constrains of this system is the limitted harvested power (around 10 100 μW), therefore we conduct two experiment to study the distance measurment performance when the availabe power on WISP Rx(Sense WISP) or WISP Tx(Spy WISP) is ideally infinate.

2.4.1 Experiment A - with power constraint

The WISP Rx(Sense WISP) tag (to be localized) was placed on a grid of $6 \times 7 \times 2$ locations in a volume that extended from 0.6m to 2.2m in the direction perpendicular to the WISP Tx(Spy WISP) plane, from -0.5m to $+0.5$m in the horizontal direction parallel to the WISP Tx(Spy WISP) plane, and from -13cm to $+9$cm in the vertical direction parallel to the Tx plane. A WISP Tx(Spy WISP) was powered externally instead of wireless power and is placed near the RFID reader antenna in order to capture reader's commands. The reader was configured to transmit $1 Watt$ RF signal into a 6 dBi circularly polarized antenna with the receive sensitivity of -80dBm. At each testing location, the reader continuously read the WISP Rx(Sense WISP) and received ToA packets for a period of 2 minutes.

2.4.2 Experiment B - without power constraint

In order to analyze the impact of the limited harvested power on the WISP Rx(Sense WISP), this experiment was conducted. An identical externally powered WISP Rx(Sense WISP) was placed at the same locations as the wirelessly powered WISP Rx(Sense WISP) and similar set of experiments were conducted. as Experiment A This allowed us to ignore the effect of wireless power on system performance.

2.4.3 Power

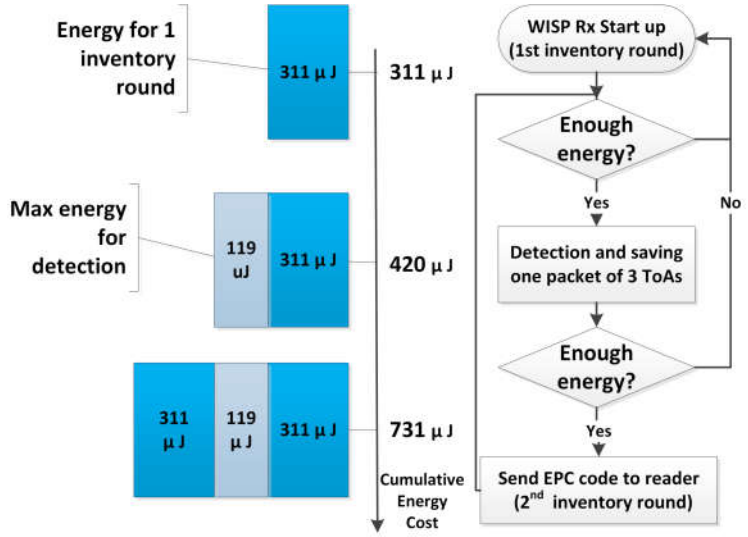

Figure 2.8: Left side: energy used in each step of the of the ToA measurement process. Right side: Flowchart of the ToA measurement process.

Figure 2.8 (right side) shows a flowchart of the events that occur when the battery-free WISP Rx(Sense WISP) measures the ToA. The left side of the figure shows the energy cost of each event. The initial state in the flow chart (at the top of the right side) is the "WISP Rx(Sense WISP) start up" event, in which the WISP Rx(Sense WISP) is initially powered up using harvested RF energy, and sends its initial EPC code without ToA to the reader. This event happens before any acoustic detection. If enough energy is available, an acoustic detection event happens next (middle box in the flowchart). In this event, the WISP Rx(Sense WISP) measures the ToA information (three ToA value) and saves them. In the next inventory round, which is called the Send event (bottom box in the flowchart), the saved EPC is sent back to the reader. The start-up event is similar to the send event and costs roughly the same amount of energy. An upper bound on the energy required for a detection event is given by the energy cost of a detection timeout, which in the present system occurs at 10 ms (about 3 m range). The power consumption of the acoustic detector

is 81 μW, so the overal energy consums by 3 acoustic detection events is 2.4μJ. This energy is small compared to the communication costs shown in Figure 2.8. Most of the energy is consumed by RFID communication.

2.4.4 Precision

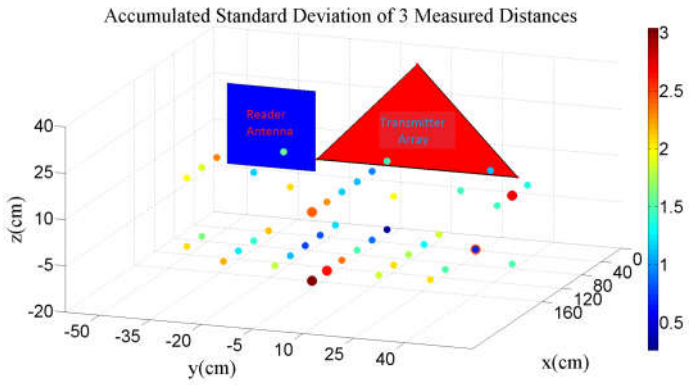

Figure 2.9: The accumulated standard deviation across three measurements is shown at each location in 3D space by both the size and color of each point. The blue rectangle represents the reader antenna, and the vertices of the red triangle represent the three ultrasonic transmitters.

In spite of the environmental factors, the accuracy of the presented system depends mainly on three factors: the precision of the WISP Rx(Sense WISP)'s detection hardware and firmware, the accuracy of the line fit matching model, and the software algorithm that calculates the final location. In this paper, we mainly discuss the second factor (i.e. the precision of this technique). So we will analyze the variance in the measured raw distance data after using line fit. In theory, the precision of the localization prototype is primarily limited by the accuracy of the acoustic tone-detector and the resolution of the digital clock used for measuring ToA. Hence, the higher the frequency of the clock, the higher the precision of the detected distance. The WISP has a built-in low-power 32.768 kHz digital crystal which

is used ToA measurement clock and results in a detection resolution of 1 cm. Additionally, the variance of attenuation of the acoustic signal during propagation and the variations in detection circuit affect the precision as well, however, these offsets can be roughly accounted in the line-fit model by training the distance-ToA data.

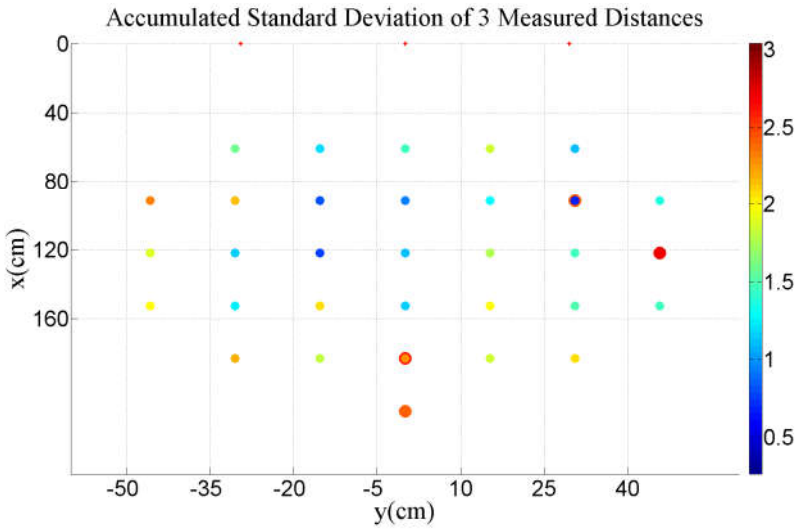

Figure 2.10: The accumulated standard deviation of 3 measured distances at each location(2D) is shown by the point size and color. The three red dot on the top is the three transmitters

Assuming we use an ideal line-fit model, the standard deviation of estimated acoustic transmitter-to-WISP Rx(Sense WISP) distance is used to indicates the precision of the prototype. In Experiment A, the WISP Rx(Sense WISP) is able to measure single acoustic transmitter-to-WISP Rx(Sense WISP) distance with the precision of 0 cm to 1.5 cm within the testing distance range of 0.6-2.2 m. Figures 2.9 to 2.11 show the accumulated precision of the measured distance based on raw ToA data (without signal processing) measured in each test location in Experiment A.

In principle, the precision of the distance measurement should be uniform in all test locations. However, experimentally we observe that precision changes with variation in measured

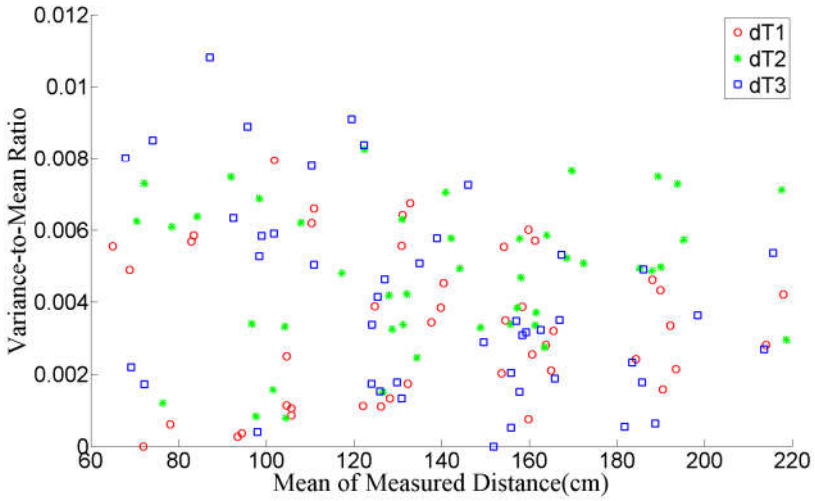

Figure 2.11: The ratio of standard deviation to mean for 3 measured distances at each location.

distance. That is due to the fact that the received RF signal and the relative location and orientation of the acoustic sensors also have some impact the system precision. Generally, (see Figures 2.9 and 2.10), as the WISP Rx(Sense WISP) moves away from the reader antenna, the harvested power reduces making the WISP power supply unstable. Since the ultrasound detecting circuit is vulnerable to the power supply, longer WISP Rx(Sense WISP)-to-reader antenna distances experience larger variance in ToA measurement. Please note that since all data points are obtained within 2 mins window, when the WISP Rx(Sense WISP) was closer to the reader antenna, due to higher harvested power (and hence lower latency/duty cycle) more samples are collected. However, when the WISP Rx(Sense WISP) was very closed to the antenna (the blue rectangular area in Figure 2.9), the strong transmitted RF signal interferes with the detecting circuit and decreases the detection precision (can also be seen in Figure 2.11). Additionally, due to RF multi-path effects and reflection from obstacles in the environment, higher RF power was received at some locations (such as the test point (170,17) in Figure 2.10) which improved the precision of the detection. Finally, the relative

location between the WISP Rx(Sense WISP) and the ultrasonic transmitter plane also influences the performance. As the orientation of the WISP Rx(Sense WISP) departs from the vertical direction of the acoustic transmitter plane (the red triangular area in Figure 2.9), the arriving ultrasound signal is not robust enough since it may fall outside the boundary of beam/ reactive pattern of the acoustic sensors. This results in increase in the variance of the measured distance.

2.4.5 Latency

The latency of distance measurement refers to the time taken by the reader to receive an updated valid packet of ToA from the WISP Rx(Sense WISP). In literature, to scale the measurement speed, update rate, which is the reciprocal of latency has been used as well. In this work, we define the update rate as the number of updated valid ToA packets read by the reader within one second. Both latency and update rate in principle are limited by: WISP Rx(Sense WISP) inventory rate determined by the reader, the acoustic transmitter-to-tag distance (see Section 2.3.1) and the amount of harvested RF energy by WISP Rx(Sense WISP).

In theory, the inventory rate of the WISP Rx(Sense WISP) is determined by the RFID communication protocol which varies with the reader (protocol) configuration and the tag population. Ideally, if only one RFID tag is present, there are no collisions and given sufficient RF power, the minimum latency t_d in our system can be written as

$$t_d = t_{WISP}(d) + d_{Tx}/v_{sound} + (n-1)\Delta t_{Tx} \times d_{Tx} \tag{2.5}$$

where t_{WISP} is the duration of one WISP inventory round, which is determined by WISP Rx(Sense WISP)-to-reader antenna distance d and is limited by the RFID protocol used by the system. d_{Tx} is defined as the maximum acoustic transmitter-to-receiver distance. Since the acoustic transmitter array (placed at the vertices of the red triangle as shown in Figure 2.9) is placed near the reader's antenna, the acoustic transmitter-to-WISP Rx(Sense

WISP) plane distance is approximately equal to d.

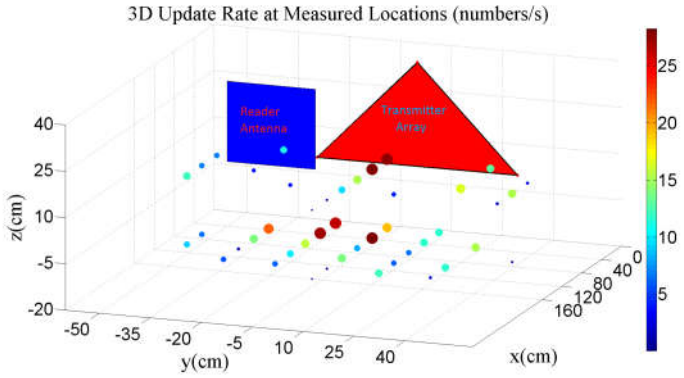

Figure 2.12: Valid ToA measurement update rate for 3D test locations, with both color and point size indicating update rate.

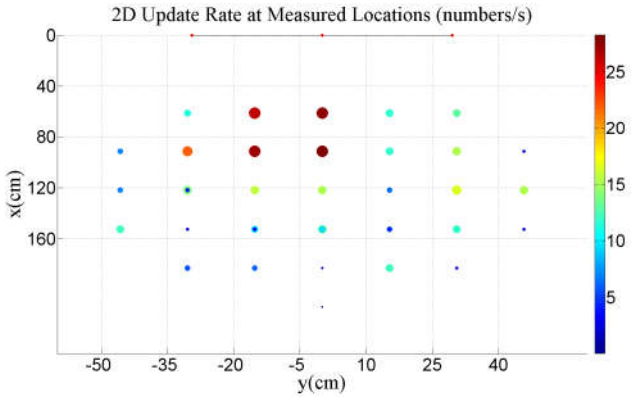

Figure 2.13: Valid ToAs measurement update rate for test locations (2D) with both color and point size indicating update rate. The vertical tested locations are overlapped. The three red dot on the top is the three transmitters

From our experimental results (see Figures 2.12 and 2.13), we observe that at each location, the available RF power constrains the system latency/update rate. Generally speaking, as the distance between the WISP Rx(Sense WISP) and the reader increases, the latency

increases or equivalently, the update rate is reduced. Additionally, in some locations, the RF multi-path effects affect the latency by increasing the power available to the WISP (see Figures 2.12 and 2.13). Please note that the harvested RF power also strongly depends on the relative orientation between the WISP antenna and the reader, thereby, affecting latency. Finally, since the orientation and location of acoustic sensors limit the detectability of the acoustic signal, in certain regions which correspond to detection boundary of the sensor, the update rate is very small (see test point (70,45) in Figure 2.13).

In Experiment B, we analyzed the relationship between available power and latency by comparing the latency and ToA event-detection count for a battery-free WISP Rx(Sense WISP) (passive) and a power supply-powered WISP Rx(Sense WISP) (active). Table 2.2 shows the degradation of latency and detection rates due to lack of power during the ToA measurement. As the distance between the WISP Rx(Sense WISP) and the reader increases, it is more likely for the WISP Rx(Sense WISP) to power off and reboot during a ToA measurement. This effect degrades the latency of the system (the successful detection in Table 2.2 refer to the event when the reader receives valid ToA measurement data). Please note that since the RF multi-path and antenna orientation determine the power harvested by the WISP Rx(Sense WISP), the trend in latency or update rate is not consist with change of distance (see test point (170,17) shown in Table 2.2). If the efficiency of the RF harvester and WISP antenna is improved, more power can be harvested, thereby better latency can be obtained by our system.

2.4.6 Range

We define the range of our system as the maximum orthogonal distance between the WISP Rx(Sense WISP) and the WISP Tx(Spy WISP) plane at which the system is operational. This is mainly limited by the harvested energy and the zone/area of the acoustic signal detection. The goal of the two conducted experiments was to analyze the limitations caused by harvested energy. Hence, to ensure acoustic detectability at the range of 5 m, we transmitted sufficiently high acoustic signal (97.1 dB SPL). The tested maximum operating range for our

Table 2.2: comparison of detection performance of passive WISP Rx(Sense WISP) and active WISP Rx(Sense WISP)

coordinates (cm)	**start-up (count)**	**Successful detection (count)**		**Success rate**		**Latency (s)**		**Update Rate (numbers/s)**	
	passive	***passive***	***active***	***passive***	***active***	***passive***	***active***	***passive***	***active***
(53.0,0,6.3)	550	215	843	0.92	0.71	0.56	0.14	1.79	7.03
(73.4,0,6.3)	329	176	2186	0.93	0.61	0.68	0.05	1.47	18.22
(103.9,0,6.3)	587	202	875	0.77	0.72	0.59	0.14	1.68	7.29
(134.4,0,6.3)	482	97	3721	0.45	0.96	1.24	0.03	0.81	31.01
(164.9,0,6.3)	745	29	3304	0.26	0.84	4.14	0.04	0.24	27.53
(195.4,0,6.3)			1259		0.76		0.10		10.49

battery free prototype was 2.2m. If the prototype is optimized for long range operation, and placed at locations where the WISP Rx(Sense WISP) has optimal RF and acoustic sensitivity, the maximum achieved localization range is 3 m. Please note that in these experiments, the beaming and reactive angle (80 °) of acoustic sensors also limit the ultrasound detection 3D area and therefore limits the range in some other directions.

According to the Friis Transmission Equation, if we assume a line-of-sight propagation of the transmitted RF signal from the reader with no RF interference, using Equations (2.6) and (2.7), we can compute that the maximum achievable measurement range is 6 m with a latency of about 3 minutes:

$$P_r/P_t = G_t G_r(\lambda/4\pi R)^2 \tag{2.6}$$

$$E_{locate} = \alpha\eta(P_r)t \tag{2.7}$$

Where P_r (-10 dBm) is the receive sensitivity of the WISP and P_t (30 dBm) is the transmitted RF power of the RFID reader. G_t and G_r are the antenna gain of the reader and the WISP, which are 6 dBi and 2 dBi respectively. The minimum efficiency η of the energy harvester of the WISP (within 5 m of the reader) is 5%. The leakage tolerance parameter α is estimated as 85%. The estimated total energy E_{locate} used to update one packet of ToA information is 731 μJ. If the energy harvesting capability of the WISP is improved using

better harvester and antenna design, the operating range can be extended.

2.5 Distance Measurement Summary and Power Optimization

The power consumption of the WISP Rx(Sense WISP) and its energy harvesting efficiency during measurement are two significant factors that determine our system's properties. The power consumed by digital computation is the most significant contributor in our prototype. The relationship between power consumption, precision, range, and latency and our tested system performance are shown in Figure 6.2. If the power available to the WISP Rx(Sense WISP) increases, the overall performance of the system improves. Reducing the latency of the system would average out the measurement noise in a given period and thereby, increase precision. However, increase in detection distance would increase acoustic propagation, energy harvesting time, and the WISP inventory time, thereby increasing the latency.

As the digital circuits scale down, the digital processing on the WISP Rx(Sense WISP) will consume less power, thereby reducing the WISP Rx(Sense WISP)'s power requirements. Alternately, instead of digital backscattering, we can use zero/low power analog backscatter method [78] to transfer the measurement of ToA on the reader side, thereby increase the operating range and latency of our system. Additionally, deployment of more efficient energy harvesting topologies and implementation of an Integrated Circuit, would offer an increased energy budget. Using these techniques, we can further improve the performance of our system.

Please note that our localization system is based on the RFID EPC Gen2 protocol, which is not designed for high communication data rates. Currently, the upper limit of our system's latency is limited by the protocol. However, with the development of the RFID protocol, our system can achieve higher RFID data rates and therefore achieve better localization latency and precision. However, as the protocol improves, the latency of our localization system will be limited more by the acoustic propagation range rather than the RFID protocol, so better acoustic transmission or detection methods, such as frequency hopping and phase detection, will be be researched to reduce the limit.

In addition, the ultrasound transducer used in this paper is fairly large, and not compatible with the thin "sticker" form factor of RFID tags. An open question is whether flat acoustic transducers, such as ultra-thin piezo-electric films or MEMS sensors, could be used to create acoustically localizable RFID tags with the same thin form factor as today's conventional RFID tags.

2.5.1 Power Optimization

Because the available power of the system is the biggest constraint of the distance measurement performance. We then optimized the firmware and hardware of the Sense and Spy WISP to consume lower power than before during RFID communication and ultrasound detection (Figure 2.4). The Sense WISP only consumes about 80 μW during a wake up cycle and 10 μW for a sleep cycle. As an optimization, stationary tags don't need to perform their location estimation continually since they are not moving. We use the accelerometer data on Sense WISP to implement this power-savings. Once the tag is detected to be stationary, a Sense WISP will increase its sleep cycle length, once motion is resumed, will increase the localization update rate to track its new position. The overall energy cost for update one package of ToAs data is improved from $420\mu J$ to $252\mu J$.

2.6 System Optimization and 3D Localization Performance

Based on the first two experiment, we improve our hardware and location process algorithm and did another two experiment to evaluate whole the system. We test the overall system and its 3D localization performance in a practical configuration, in which the Spy WISP(WISP Tx) is totally wireless powered by the RFID reader. The use of wireless powered Spy WISP may reduce the overall sample update rate, however will offer more freedom for system setup and system expansion.

2.6.1 Experiment C - study of system accuracy

We use single wireless powered Spy WISP(WISP Tx) and single Sense WISP(WISP Rx) in an open $1.2m * 1.2m * 1.8m$ space to test the overall performance in a real scenario. In this experiment, the same reader and reader configuration is used, the Spy WISP is battery-free and drives four ultrasound transmitters which are placed at the 4 verticals of a 15cm-long square with known locations, all of which are in line of sight of the Sense WISP. The use of 4 transmitters instead of 4 is to reduce the error caused by TOA measurement. This powers Sense WISPs up to 3.5m away in the most sensitive direction. The total energy used by a Sense WISP to update one 3D location is below $252\mu J$. The experimental results are shown in Figure 2.14 and Figure 4.2. In theory, using the RFID synchronization and acoustic TDMA method [99], the system can support localizing up to 65535 Sense WISPs, however, the localization update rate for each tag will relatively decrease if the system scales up.

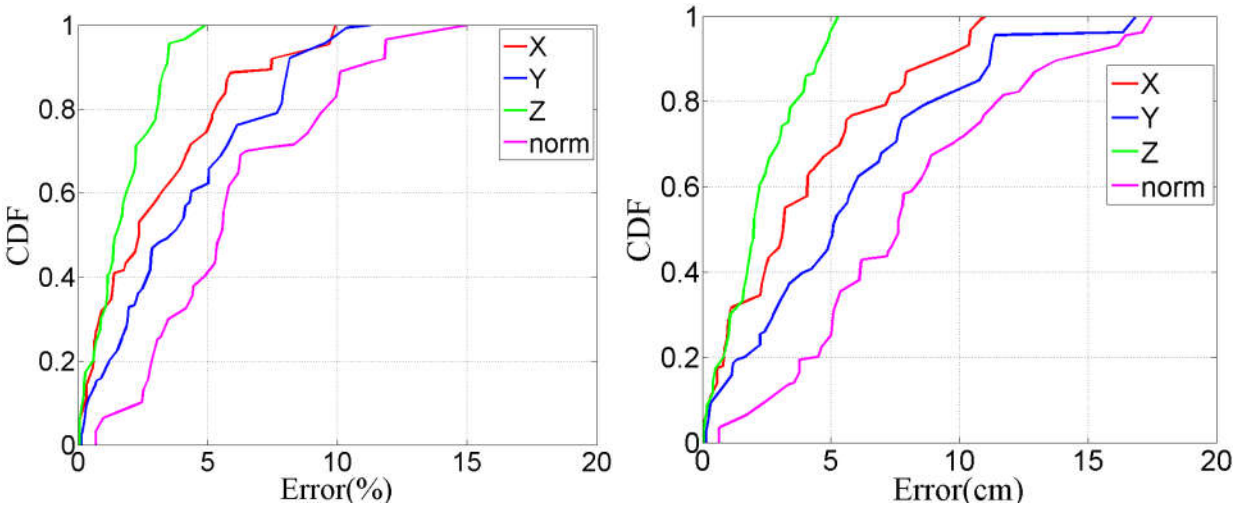

Figure 2.14: Free space localization performance: CDF of localization error distribution, in percentage and absolute units.

Accuracy: Because of the geometry of the ultrasounds transmitters, the system can obtain better accuracy in the z axis, which is perpendicular to the planes of transmitters.

3D geometry setup of those transmitters would improve the accuracy for other axes. Figure 4.2 shows that accuracy decreases as the Sense WISP-to-transmitters distance or ultrasound angle of arrival increase. Because the attenuation of ultrasound and directional ultrasound sensor introduces non-liner noise which can not be modeled well using line-fitting model at those circumstance. The average accuracy is $(3.1, 5, 1.9)cm$ for each (x, y, z) direction within testing range.

Range: The system maximum localization range is $3.4m$ (when $x = 0, y = 0, z = 3.4m$). The range of the system is limited by the amount of available power for Sense WISP, that means when the Sense WISP is out of the range, it is not able to powered up or complete detection.

Update Rate: The update rate for this system is limited by the available RF power for Sense WISP, its energy harvesting efficiency and RFID protocol (maximum 45 S/s for Sense WISP), and is $5S/s$ $31S/s$ for this experiment. It will decrease as the population of Sense WISP increase. The average update rate is 15 S/s and can be adjusted by changing the sleep time of either Spy WISP and Sense WISP. High-gain omni-directional antennas can offer better power density, and thereby improve the update rate if needed.

Acceleration detection: the system is able to detect the movement of Sense WISP tagged objects. When grasping tagged objects, the system has 90% confidence of detecting the movement within $1m$ tag-to-reader range. In order to capture tag movements like being grasped, the reader has to poll Sense Tags with a relatively higher rate than the movement. Our ability to do so is limited by the RFID protocol and available RF power near the Sense WISP. For static tags whose orientation is already known to the system, our system can detect the change of its orientation even at a lower Sense WISP update rate at a range of 1.8m. More antennas deployed in the test space extend that range.

2.6.2 Experiment D - application and implementation

One high-value application of context-awareness (and one of the largest challenges facing science) is the documentation and replication of scientific lab experiments. A 2012 study, for

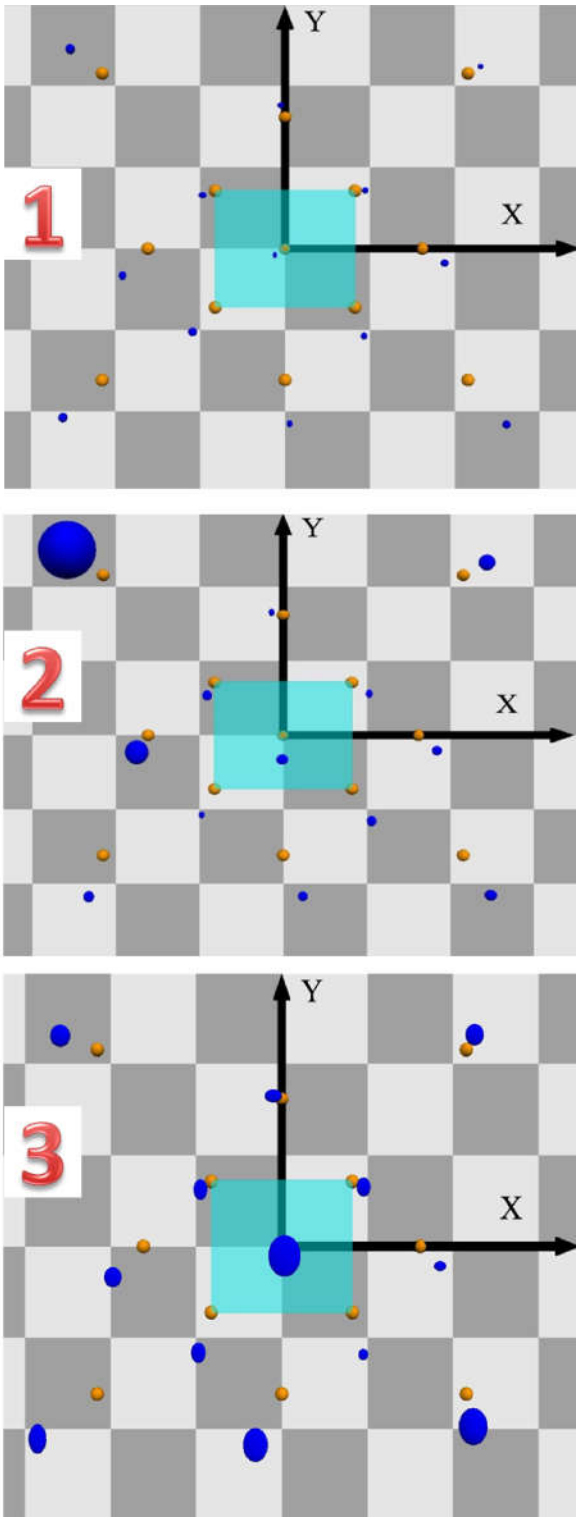

Figure 2.15: Localization accuracy in 3D open space: sub-figures $1-3$ show results at $z = 94cm, z = 134, z = 174cm$. The 4 ultrasound sources in are placed at the vertices of the $16cm \times 14cm$ cyan squre in the center of the chess plane ($20cm$/grid, origin at the center). The yellow ball is the ground truth location with sensor's acutal size (radius= $8mm$). The

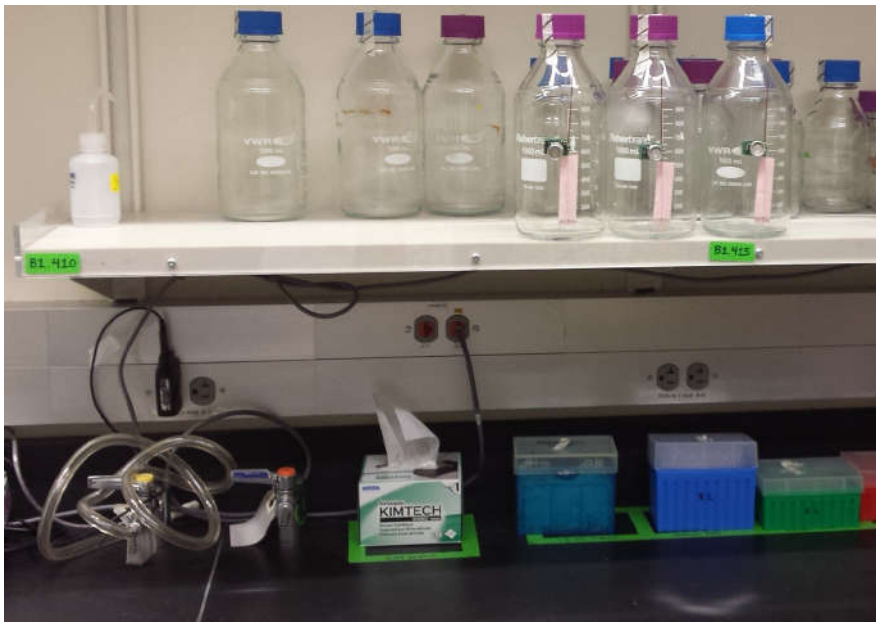

Figure 2.16: Wetlab. We are exploring the use of the localization tags for activity inference in a wetlab scenario.

example, showed that 47 of 53 key cancer biology results could not be replicated, in some cases even with the help of the original researchers [14]. Part of what makes documentation and replication difficult is the large number and subtlety of the steps performed during a lab experiment. Another factor is that often documentation is performed after the fact since both hands are needed to perform experiment, and lab technicians often wear protective gloves that make writing or typing difficult.

Accordingly, we are using a self-documenting smart wet lab as a guiding application of our location system, using a cluttered lab bench as our deployment environment (Figure 2.16). We are RFID-tagging key objects in the lab (e.g.: bottles of reagents and glass containners) and tracking their location and motion as experiments progress. Using accurate, high-update rate location readings from our tags, we aim to not only infer which specific objects are present on the bench, but when, where and how they are used. With this detailed object location and motion data, coupled with representations of the experimental protocols we

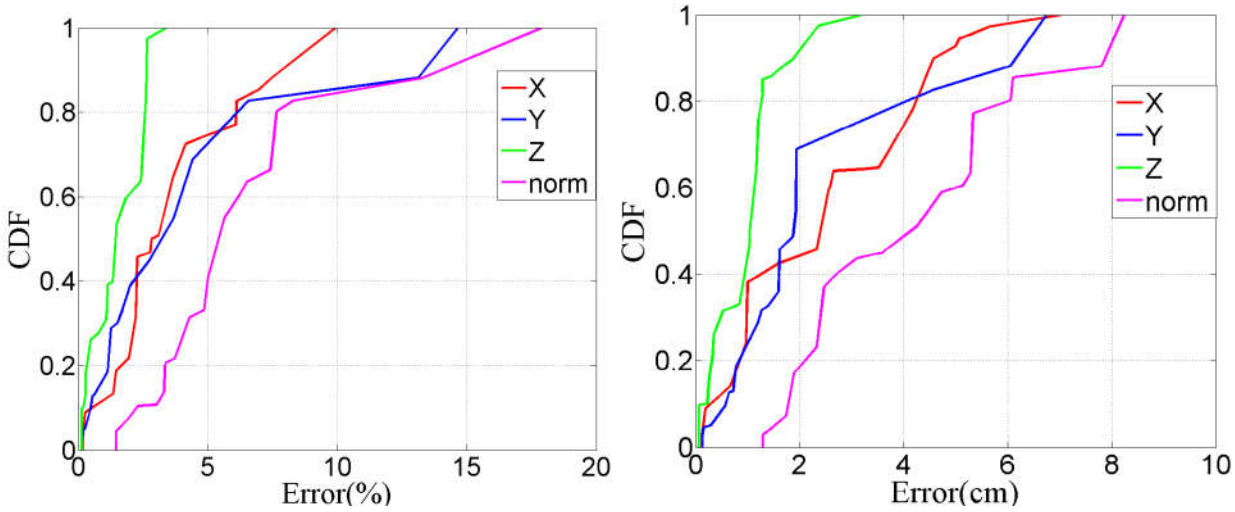

Figure 2.17: Wetlab localization performance: CDF of localization error distribution, in percentage and absolute units. The performance is not significantly different than the freespace case.

hope to be able to infer and document the objects being used, actions performed on/with them, and recognize the experiment being performed.

We implement this system in an $(0.8m \times 0.5m \times 1.2m)$ lab bench (one table and one shelf above) in the smart wet lab (Figure 2.16) and attach Sense WISP tag to several bottles of reagents, the system can then infer the current state and activity of those bottles by measuring its location and movement(such as it is on the shelf or in media preparing area) and infer their activity and state. An experiment is designed to report the current static location of 1 object, 2 objects or three objects in 14 different locations. The average accuracy can be seen from Figure 2.17.

A second lab experiment was conducted to try to recognize a pouring event, when the contents of a WISP-tagged bottle is poured into another container. Two identical containers are placed the same distance from a tagged bottle. During the test, the researcher grasps the tagged bottle from the table and pours its content into one of the two containers (in known locations). Once any movement of the bottle is detected and the bottle's orientation

is horizontal, the system computes the current location of the bottle. The system then can estimate which container the tagged bottle is pouring into. Placing the pair of container in 5 different places, the system can detect the correct pouring destination container with 90% confidence for 8 times the pouring event for each location. However, in this single antenna system, the reading update rate of the Sense WISP by the reader depends on the available RF power and RFID inventory protocol, therefore limiting the motion sampling rate. More antennas and readers can help to improve the update rate as well as motion recognition ability by increasing available RF power in the space. Besides pouring action, other position-related object movement can be detected in theory as long as the required accelerometer sampling rate is within tag's reading rate.

Chapter 3

NEAR FIELD - A SENSING AND COMPUTATIONAL ENHANCED NEAR FIELD COMMUNICATION PLATFORM

3.1 Introduction

Near-field Radio Frequency Identification (RFID) technology has achieved wide spread adoption in traditional application spaces such as access control, inventory management, and secure payment [7]. The recent inclusion of Near-Field Communication (NFC) readers in to smart phones has enabled a resurgence in near-field RFID technology with applications focused on human computer interaction, smart living spaces, and healthcare [16, 22, 33]. With high quality, mobile NFC readers readily available, there is the opportunity to develop new tag hardware with enhanced capabilities to enable further innovation in these application spaces.

At its core near-field RFID tags are wirelessly powered computing devices with basic communication capability, and are activated in the presents of RFID readers. They are small, thin, and low in cost allowing for easy integration into many types of objects used throughout daily life. Although the read range is typically on the order of 1cm to 10cm these tags are able to harvest relatively large amounts of power through inductive coupling compared to UHF RFID tags. However, existing commercially available near-field RFID tags are fixed function devices that only report an ID along with a small payload of data. For many usage scenarios the retrieval of the tags ID is simply a means of obtaining a digital pointer to online content or to activate a user application. Although useful in its own right, the usage metaphor of "tap to activate" is rather limited and does not harness the full potential of the core capabilities of near-field RFID technology.

There are several notable projects that push beyond this simple usage model. Marquardt

et. al. [40] describe several ways to add user input and output capabilities to NFC tags in the form of LEDs, vibrating motors, audio beeps as well as touch switches. In all these examples the 13.56MHz RF signal is directly manipulated to provide enhanced functionality rather than using the digital logic inside the commercial RFID ICs. Alternatively, IC manufactures have begun offering NFC chips with a greater range of capabilities [8, 74]. These devices operate as dual interface memory modules where data can be stored and retrieved from non-volatile memory through either a RFID interface or through a microcontroller bus such as I2C or SPI. Although these chips are limited in functionality and fixed to a single protocol when paired with an external microcontroller basic sensing tasks can be accomplished.

In contrast, researchers specializing in integrated circuit design have been able to take full advantage of the capabilities of near-field RFID technology by customizing circuit blocks for peak performance and adding new circuits that extend functionality. One example is a fully implantable, NFC enabled blood glucose monitor [23]. This chip is wirelessly powered through a 13.56MHz inductive link and communicates via an extension to the ISO15693 protocol. On board LEDs and an integrated photo sensor are used to create a fluorimeter which measures blood sugar levels and reports data transcutaneously back to a mobile device. This example shows the potential of near-field RFID technology. However, the process of manufacturing custom integrated circuits presents a significant barrier to entry when considering the high cost of development, chip fabrication, as well as long fabrication cycles.

In order to take full advantage of the unique technology traits of near-field RFID and to allow researchers to rapidly explore new NFC related applications we present the NFC-WISP (Near Field Communication - Wireless Identification and Sensing Platform), which is shown in Figure 3.1. The NFC-WISP is a fully programmable sensing and computing platform designed to explore new RFID sensor and human interface applications. At its core it is a software defined RFID tag built around an ultra low power microcontroller (TI MSP430), which handles all the NFC protocol, sensing and I/O tasks in firmware. The NFC-WISP is fully powered and read by commercially available RFID readers (including NFC enabled smart phones) using the ISO-14443 protocol. Extra harvested power can be stored in an

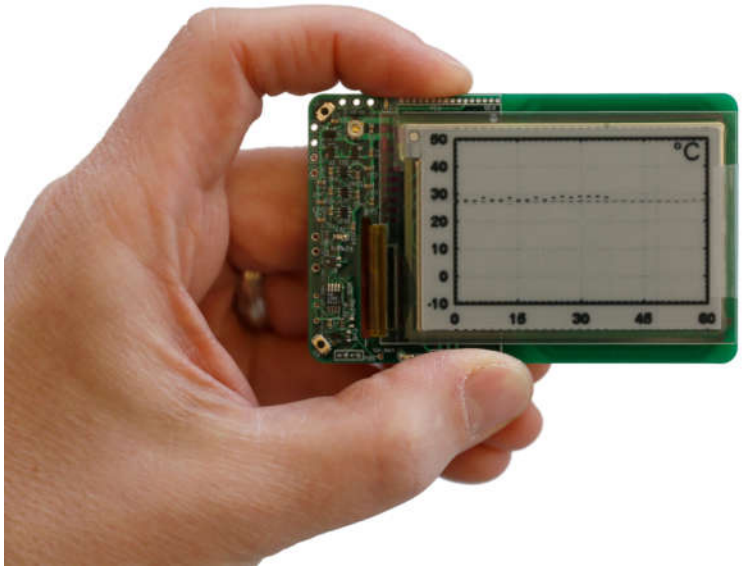

Figure 3.1: Image of the NFC-WISP 1.0 with the optional E-ink screen installed.

optional super-capacitor or thin-film battery enabling operation away from the reader. The platform includes temperature and acceleration sensors, 2MB FRAM, LEDs and an optional E-ink display as well as header pins that interface with the onboard microcontroller for rapid prototyping of new applications.

The NFC-WISP is similar in design and construction to its predecessor the WISP 4.1 DL [67], which for the sake of clarity will be referred to as the UHF-WISP. The key difference is that the UHF-WISP is designed to be a far-field RFID tag operating in the 915MHz ISM band and compliant with the EPC Gen 2 protocol. Another NFC related research effort is the OpenPCD project which has developed a PCB based sniffer tag, but it requires a battery for operation and does not have sensors or display capabilities [36]. Previous work demonstrated the concept of a "Display Tag" which used a E-ink screen as a wirelessly powered, secondary display for smart phones [26]. We extend prior work with a new and more robust hardware and firmware design, as well as a thorough description of the operation and performance characteristics of the NFC-WISP, and demonstrate new applications including: perishable

goods temperature and motion monitoring and the use of wireless power transfer based on magnetic coupled resonance for high power recharging of multiple NFC compatible devices.

3.2 Hardware Architecture

The NFC-WISP consists of a four layer Printed Circuit Board (PCB) with surface mount components on both sides. The overall dimensions are the same as a standard banking and personal ID card, although slightly thicker ($85.60 \times 53.98 \times 4.8mm$). The near-field antenna is printed on the PCB and consists of a four turn square spiral, with outside dimensions of 42mm by 53mm and a trace width of 1.27mm. Its inductance is 1.2nH and a tuning capacitor is added to make the antenna resonant at 13.56MHz. The matching network is tuned such that the loaded quality factor of the coils when in the presence of the reader is approximately 20, allowing for enough bandwidth to support the 106kbit/s data rate of the ISO 14443 protocol.

A block diagram of the NFC-WISP is shown in Figure 3.2. The coil antenna and tuning network feed the power harvesting block which rectifies the incoming RF energy into DC voltage to power the system. Since near-field RFID tags receive more power than far-field RFID tags an optional high-density storage element in the form of a battery or super capacitor can be used for long-term storage. The demodulator follows the envelope of the RF carrier wave to extract the amplitude shift-keyed data stream from the NFC-RFID reader. This baseband waveform is read by the TI MSP430F5310 MCU and a 13.56MHz external crystal is used for data recovery. An additional low power and low frequency 32.768kHz watch crystal is used to enable realtime clocking functionality with lower power cost. Uplink data is sent back to the reader from the tag via load modulation. Onboard peripherals such as LEDs, the MSP430s internal temperature sensor, FRAM and an Analog Devices ADXL362 3D accelerometer are powered and managed by the MCU. Finally an optional 2.7 inch Pervasive Display E-ink screen with a resolution of 264×176 ($117dpi$) can be used via the Hirose Electronic's 40 pin ZIF connector.

The primary advantage of the PCB implementation is that it allows designers to quickly

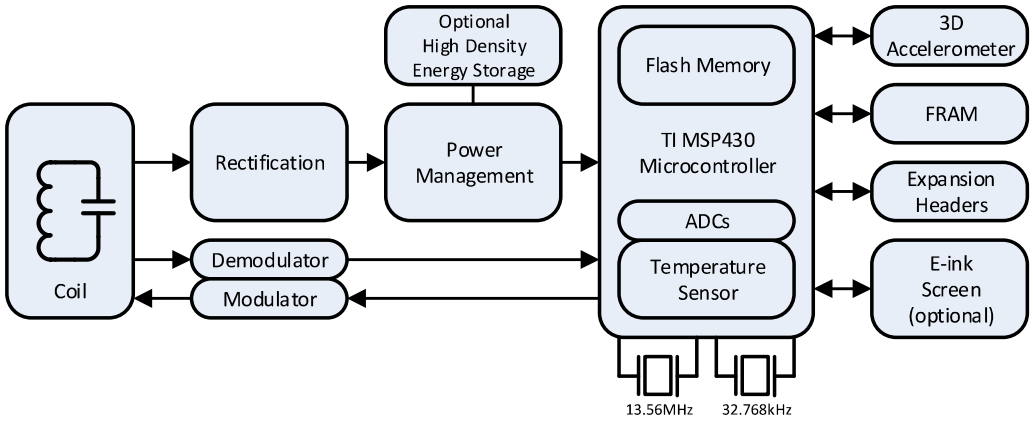

Figure 3.2: Block diagram of the NFC-WISP.

and easily modify the hardware and firmware to create new applications. For example if a researcher wants to add a new sensor to the NFC-WISP the exposed header pins allow for easy access to the microcontroller's ADCs and/or digital communication ports (SPI, I2C, or UART). Once the new sensor is added to the NFC-WISP the microcontroller can quickly be reprogrammed to interface with the new device by using one of the many commercially available and supported IDEs. Finally testing can be done with bench top lab equipment and a JTAG debugger.

3.3 Energy Harvesting and Power Management

From a power harvesting perspective one of the key advantages of inductive coupling (as compared to far-field energy harvesting methods used on the UHF-WISP) is that the relatively high power levels and the voltage multiplying effect of the multi-turn receive coil means that the NFC-WISP is not inherently voltage constrained. Clearly the system is still power constrained and it must be heavily duty cycled to avoid browning out. However, if the NFC-WISP is placed into sleep mode such that the quiescent current is 9.7μA, it is quite easy to harvest 4-5 volts on the 300μF capacitor bank (or given enough time 4-5volts on

the high density storage element). Another way to view this power harvesting optimization problem is to realize that the source resistance of the inductive coupled system is typically much lower than in far-field systems.

Figure 3.3 panel A shows a detailed block diagram of the power management circuitry. A three-stage full wave rectifier is used to convert the 13.56MHz RF wave into un-regulated DC voltage, which is stored on a 300μF bank of ceramic capacitors. A 5.6v Zener diode is used to provide over voltage protection. The unregulated power is passed to a 2.5v linear regulator, which was chosen for robustness, fast start up time, and low headroom. When the rectified voltage is under the 2.5v threshold the linear regulator stays open and passes unregulated power to the system. Under most circumstances the NFC-WISP can harvest more power from the reader than it consumes (a detailed analysis of power consumption is presented in section 3.6). This power can be stored in an optional high density storage device for use with high current peripherals or for prolonged sensing and computing tasks were the NFC-WISP must operate away from the RFID reader.

The LTC4071 shunt battery charger was chosen since it is a linear trickle charger that does not induce switching noise on its $V_{Rectified}$ supply line. Additionally, the LTC4071 provides a simple two pin interface (power and ground) and current can flow bidirectionally, mimicking the functionality of a large capacitor. When extra charge storage is needed either a thin-film battery such as the Power Stream 30mAh, 3.7V PGEB014018 or a super capacitor such as the Kanthal 0.1F LX055104A can be used. If the use of a battery is not needed, the user can easily disable the charger IC in the hardware.

Figure 3.3 Panel B shows a conceptual diagram of the operating points of the NFC-WISP based on the rectified voltage. Assuming the system starts from a cold start (i.e. $V_{Rectified} = 0v$, when the NFC-WISP is with in range of a RFID reader the rectifier will start storing charge on the 300uF capacitor bank. When the rectified voltage reaches 4.2V the main supervisor block enables the 2.5v linear regulator and the system begins operating.

If a thin-film battery or supercap is installed, the supervisor will also enable the LTC4071 at 4.2v. It should be noted that once the LTC is enabled the $V_{Rectified}$ node will essentially

be "pegged" at the operating voltage of the charge reservoir. This means that it may take a long period of time to charge up the battery / supercap. However, passive operation is guaranteed since the LTC4071 will disconnect itself from the system at 2.7v, thus leaving 2.7v of charge on the 300μF capacitor bank which is enough energy for passive RFID reads and simple sensing task. As a point of reference the storage cap on the UHF-WISP is only 10μF.

As power is consumed the stored voltage will decrease resulting in a number of warning signals and ultimately the shut down of the system. At 2.3v a second supervisor warns the MSP430 that stored power is limited and is below the minimum voltage requirement for updating the E-ink display. At 1.8v the main supervisor block disables the linear regulator and the system is power down to avoid the MCU entering a prolonged and uncontrolled brown-out state. The NFC-WISP also includes a voltage measurement circuit consisting of a pass transistor network and a voltage divider. Thus, at anytime the MSP430 can measure the rectified voltage to determine if there is enough stored charge to complete a given task.

3.4 Demodulation, Data Recovery and Load Modulation

The task of demodulating and interpreting the amplitude modulated data from the RFID reader, is particularly challenging given the limitations of discrete components and an off-the-shelf microcontroller. Thus, the power consumption and timing constraints of the MSP430 must be carefully considered so that the system does not "brown out" when operating in fully passive (i.e. battery free) mode.

Figure 3.4 shows a simplified circuit diagram of the analog front end of the NFC-WISP. It has been designed to demodulate both the ISO-15696 (1:256 & 1:4) protocols as well as the ISO-14443 (A & B) protocols. However, at the time of this publication only the ISO-14443B protocol has been fully implemented in firmware on the MSP430. Returning to Figure 3.4, the raw RF signal from the antenna is fed into an envelope detector which consists of a single stage full wave rectifier. The resulting signal is shown in Figure 3.5 and is labeled "Bit Line".

One challenge is that the ISO-14443 Type-B protocol uses 10% carrier modulation depth

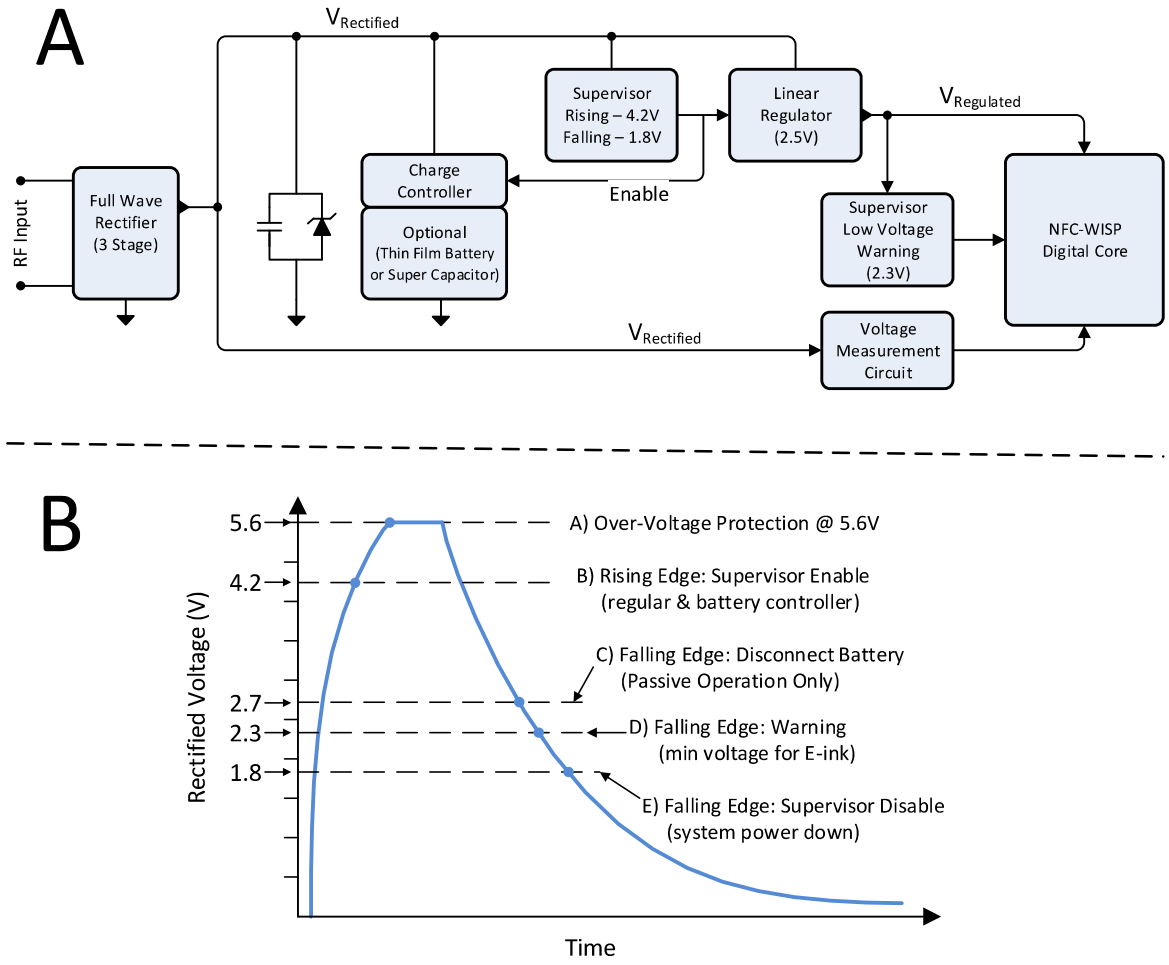

Figure 3.3: Panel A shows a detailed block diagram of the power management circuitry along with optional thin-film battery or super-capacitor. Panel B shows activation thresholds based on harvested power.

as apposed to both ISO-14443A or EPC Gen 2 which both use a modulation depth of 90% or greater. This means that once the RFID signal from the reader is demodulated, the data symbol difference on the "Bit Line" (that is the voltage difference between symbol "1" and symbol "0") is typically between 2mV to 20mV. Further complicating the task of bit recovery is that the DC bias level of the "Bit Line" changes as a function of RF input power (i.e.

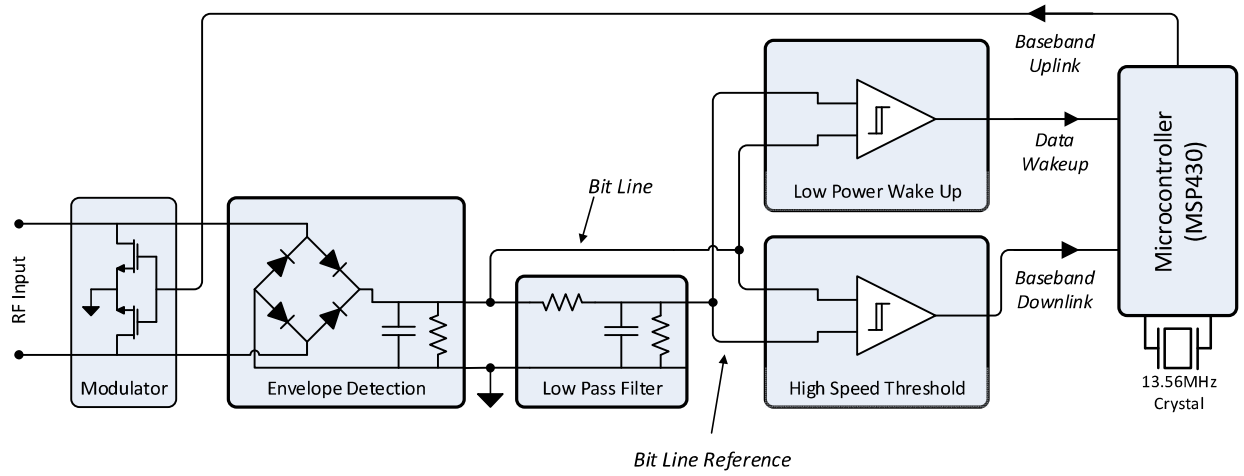

Figure 3.4: Simplified circuit diagram of the demodulation and data recovery blocks, along with wake up and load modulation circuitry.

reader to tag distance), and fluctuations in the system load can cause low frequency load modulations that ripple back to the antenna and can also change DC bias points.

To overcome these challenges, a low pass filter is used to track the mean amplitude of the "Bit Line". This signal is shown in Figure 3.5 and is labeled as "Bit-line Reference". These two signals ("Bit Line" and "Bit Line reference") are sent to a high speed comparator which thresholds and level shifts the data so that in can be interpreted by the MSP430. Since the quiescent current draw of the high speed comparator is ∼10uA, it is power gated by the MSP430 and only used when demodulating data from the reader. The rest of the time the low power (and lower speed) comparator is used to wake up the system when RFID data is detected. The low power comparator consumes ∼10nA of current and the complete NFC-WISP consumes 9.7μA of current when in low power sleep mode.

Both the ISO-15693 and ISO-14443 protocols are designed to allow the RFID tags to use the 13.56MHz ($\pm 7kHz$) RF carrier as a clock for their digital logic blocks. Additionally the data transmitted from the reader to the tag, has timing requirements such that the symbol

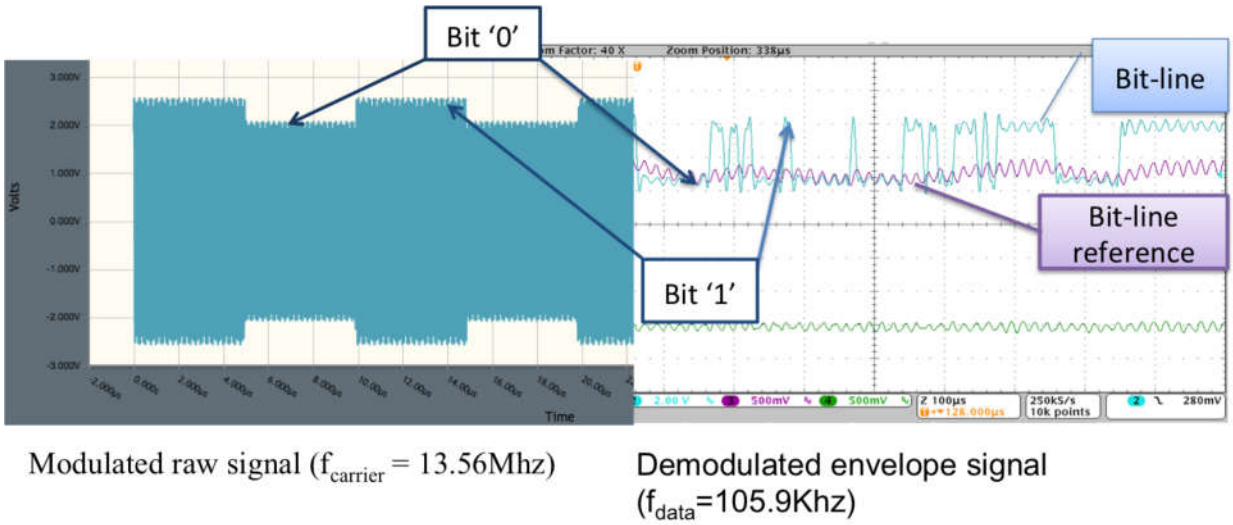

Figure 3.5: The right panel shows ASK modulated data from the RFID reader. The left panel shows the demodulated envelope labeled "Bit Line" and the average amplitude labeled "Bit Line Reference". These two signals are sent to the high speed comparator for thresholding.

rate = carrier frequency / 128. This has two important implications for conventional tag design: 1) the tag does not have to use extra power or die space for clock generation circuitry, and 2) recovering the timing of the data signal (i.e. data clock) is implicit in the protocol making data recovery a much simpler task. Essentially a normal NFC tag can simply use a timer, that is clocked by the RF carrier, to record the time interval between data edges in order to recover the raw bits.

In contrast the NFC-WISP uses an external 13.56MHz crystal as a clock source when communicating with the reader, instead of the RF carrier itself. This architectural choice was made to avoid the potential of a corrupted "RF clock" halting code execution on the MSP430. A further decoding challenge imposed by the discrete analog-front-end is that the bit width is not always constant as a function of input power due to the RC time constant of the envelope detector. Also small shifts in the symbol rate occur since it is tie to the carrier frequency which can deviate $\pm 7kHz$ from 13.56MHz.

To address these issues and increase the timing tolerance, a new interrupt based data recovery subroutine has been implemented on the MSP430 using a mixture of assembly and C. In this approach the the 13.56MHz clock generated by the crystal is divided by 8 and used to clock Timer A. The MSP430 is placed into sleep mode (LPM3) and a wakeup interrupt is set on the demodulated data edges from the high speed comparator. When triggered the interrupt routine starts/stops the timer and compares its values to expected thresholds for 0 and 1 bits. Although this approach results in a small increase in power consumption as compared to the previous method [26], it significantly increase the robustness and usability of the platform as the timing tolerance is increased by $\pm 30\%$

Communication from the NFC-WISP to reader (the uplink) utilizes BPSK (Binary Phase Shift Key) load modulation. Two uplink transistors are controlled by the MSP430 to encode NRZ-L data on a 847.5 kHz load modulated subcarrier. Since the NFC-WISP can generate fully custom data packets in software, data can be sent to the reader as part of the tags ID or as part of the read command.

3.5 Firmware

The firmware of the NFC-WISP is optimized for minimum power consumption and as such the system is heavily duty cycled. Figure 3.6 depicts the firmware state diagram implemented on the NFC-WISP. After the NFC-WISP is powered up from a cold start, all communication functions and user applications are initialized and the NFC-WISP will enter a NFC reading waiting sleep mode. In this sleep mode, only the 13.56MHz crystal and the wake-up comparator mentioned in 3.4 are enabled, other hardware peripherals are either disabled or put into standby mode. The MSP430 in NFC-WISP waits for an interrupt from the low power wake-up comparator indicating that NFC traffic is present. If valid NFC data is detected, the system enters the NFC event handler routine which interprets ISO-14443 Type-B commands sent from the RFID reader, formulates packets, and responds back to the reader via load modulation. Any other tasks or interrupts required for user applications are either disabled or blocked to avoid interfering with NFC communication.

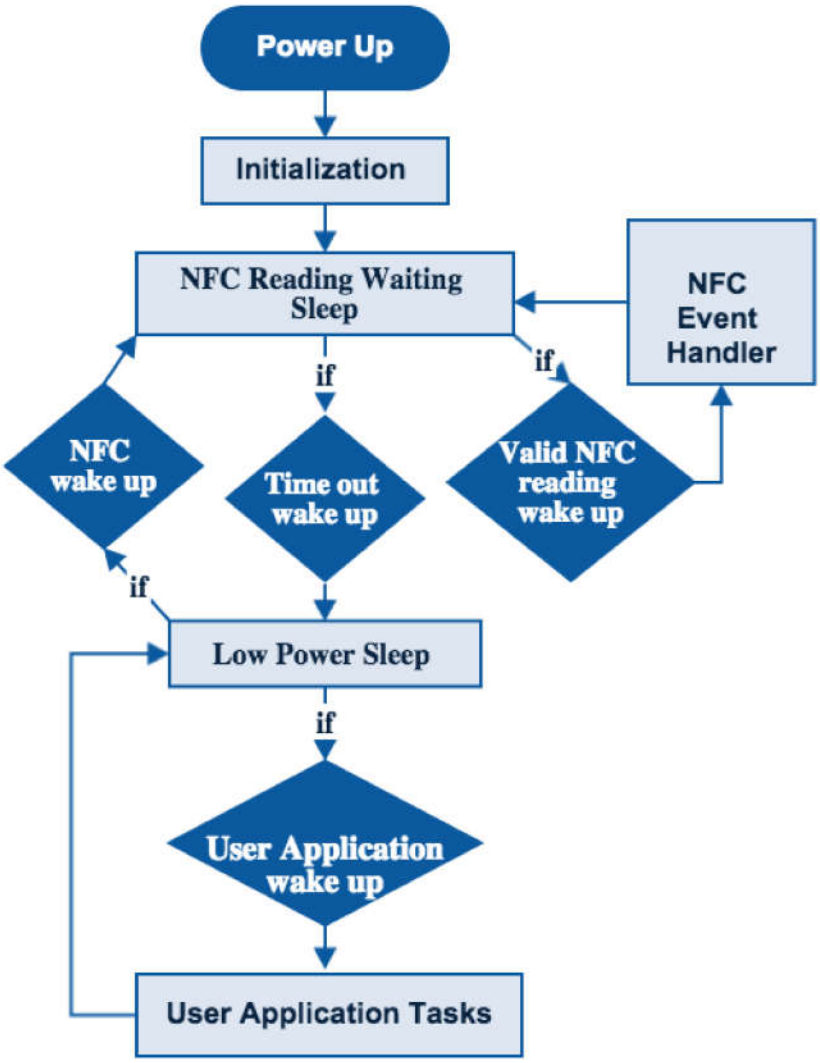

Figure 3.6: Firmware diagram with API interface.

However, if no NFC traffic appears within a pre-defined timeout, the NFC WISP will enter a low power sleep mode in which the 13.56MHz crystal is disabled to further save power. All interrupts from either the wake-up comparator or user applications are enabled in this mode. Typically, user applications are heavily duty cycled to conserve power. Sleep functionality is handled by the user application which allows the programmer to specify

wakeup intervals and events. Once in this low power sleep mode, the system can either be woken up by NFC traffic interrupts from the low power comparator or by the applications. In order to simplify programming tasks for the users, the application function is decoupled from the NFC communication. As such while the application task are running, all NFC communication interrupts are halted until the system returns to the low power sleep state. If NFC traffic wakes up the system in this low power mode, it will enable and stabilize the 13.56MHz crystal and jump into the previous NFC reading waiting sleep mode to further decode the NFC commands.

Note that all data can be passed between the application and NFC event handler via a data structure that can be stored in SRAM or non-volatile memory. The RFID reader or cell-phone can also send commands directly to the application space triggering actions such as configuring sensing tasks, taking sensor readings, preparing data for off load or updating the E-Ink screen.

3.6 Performance and Measured Results

The NFC-WISP's read performance and power harvesting characteristics were tested using the Texas Instruments TRF7970A evaluation board and the Nexus 5 smart phone (which uses Broadcom's BCM20793M NFC controller). The TI NFC reader is configured to repeatedly query the NFC-WISP using the REQB command at a known peak power level of $200mW$. The Nexus 5 smart phone allows for a more real world testing scenario but offered limited control over the NFC communication. The "NFC Research Lab" Android application was used to read the NFC-WISP. In this case it was observed that the Nexus 5 continuously scanned for tags using multiple NFC protocols at an unknown output power level.

The results for passive read range (without a battery) and semi-passive read range (with a 30mAh thin-film battery) are shown in Table 3.1. Since the NFC-WISP operates in a duty cycled fashion it can take several read cycles to harvest enough voltage for tag operation. In passive mode charge up time is less than a second and the latency is not apparent to the user. As described early, if there is not enough charge on the battery in semi-passive mode

the NFC-WISP defaults to passive mode. It should also be noted that the read rate and tag alignment are more robust in semi-passive mode since the presence of the battery stabilizes load current pulses which can corrupt the demodulator signal.

Table 3.1: NFC Reading and Harvesting Performance

Category	**Reader Type**	**Value**
Read Distance: Passive Mode	TI NFC reader	3cm
	Nexus 5	0.5cm
Read Distance: Semi-Passive Mode	TI NFC reader	11.5cm
	Nexus 5	1.2cm
Extra harvested current: Sleep Mode	TI NFC reader	4mA
	Nexus 5	1.9mA
Extra harvested current: Read Mode	TI NFC reader	3.7mA
	Nexus 5	1.65mA

Table 3.1 also shows the amount of excess current that can be harvested (at 3.7V) for different operating modes. In this test the tag was place directly next to or on the reader to show the maximum amount of harvestable current. Clearly, if the tag is place at its maximum read distance no excess current will be available for harvesting. It should be noted the polling rate of the reader significantly effects the amount of average power that is transferred to the tag, while peak reader power is most useful for increasing tag read range.

The energy consumption of the NFC-WISP for different tasks is shown in the Table 3.2. In Sleep Mode (which is also used for Charging Mode) the MSP430 goes to sleep and all

peripherals such as FRAM, accelerometer, and E-ink screen are placed into standby mode as described in section 3.5. The average transmit and receive power consumption for a ISO-14443B communication round is also shown. A detailed screen shot of the demodulation and modulation power consumption is shown in Figure 3.7. Here the demodulated REQB command from the reader is shown in blue (labeled: RX) and the tags ATQB response packet is shown in purple (labeled: TX). Real time power consumption is plotted in red (labeled: Power). The energy consumption of other tasks depends on the peripherals used and how they are configured. A few examples such as temperature sampling and accelerometer measurements are reported in table 3.2.

The new generation of E-ink screens from Pervasive Displays uses a new driver that reduces the power consumption and update time compared to our previous work [26]. It is useful to remember that E-ink technology is bi-stable meaning that the image remains without consuming any active power. Thus, the power consumption numbers reported are for changing the image on the screen. The quality of the updated image on the E-ink display depends on how many times the new image is loaded to the screen (referred to as frame cycles). If only one frame cycle of a new image is applied, ghosting of the old image can remain. Thus more frame cycles will improve the new image quality but will also increase the energy cost. Additionally, individual lines of the E-ink screen can be updated greatly reducing power and update time. This is particularly useful when updating a plot of sensor data since most of the screen will remain the same.

3.7 Applications

The NFC-WISP is a programable NFC tag and has an ultra-low power display, large data storage, as well as computing and sensing capability. A user can either create customize applications using current hardware or add other peripherals through the extension headers to add new functionality to the base platform. Below we introduce some application examples which use the stock NFC-WISP hardware.

Table 3.2: NFC WISP Power Consumption

Category	**Power Consumption**	**Duration**
Sleep/Charging Mode(disable FRAM)	9.7μA*	N/A
Sleep/Charging Mode(enable FRAM)	12.7μA	N/A
Demodulation(REQB command)	2.6μJ	783μs
Modulation(ATQB command)	11.4μJ	1.6ms
E-ink Update(1 frame cycles)	8.1mJ	0.57s
E-ink Update(4 frame cycles)	9.72mJ	0.98s
Accelerometer (single sample)	267nJ	45μs
Temperature sensing (single sample)	369nJ	94μs
Temperature sensing and single line E-ink update	3.6mJ	0.57s

*Quiescent current draw

3.7.1 Cold Chain Data Logging

Below,we demonstrate the use of the NFC-WISP as a data logger and display for a cold chain monitoring application. Since the tag needs to operate away from the RFID reader a high density storage device (in the form of a $30mAh$ thin-film battery) is included as shown in Figure 3.8 panel A. Panel B shows the NFC-WISP mounted to a milk container with the optional E-ink screen included. It should be noted that the E-ink screen does not have any noticeable effect on the performance of the coil antenna. In this experiment the milk container is sent on a simulated shipment around our office; and temperature, 3D

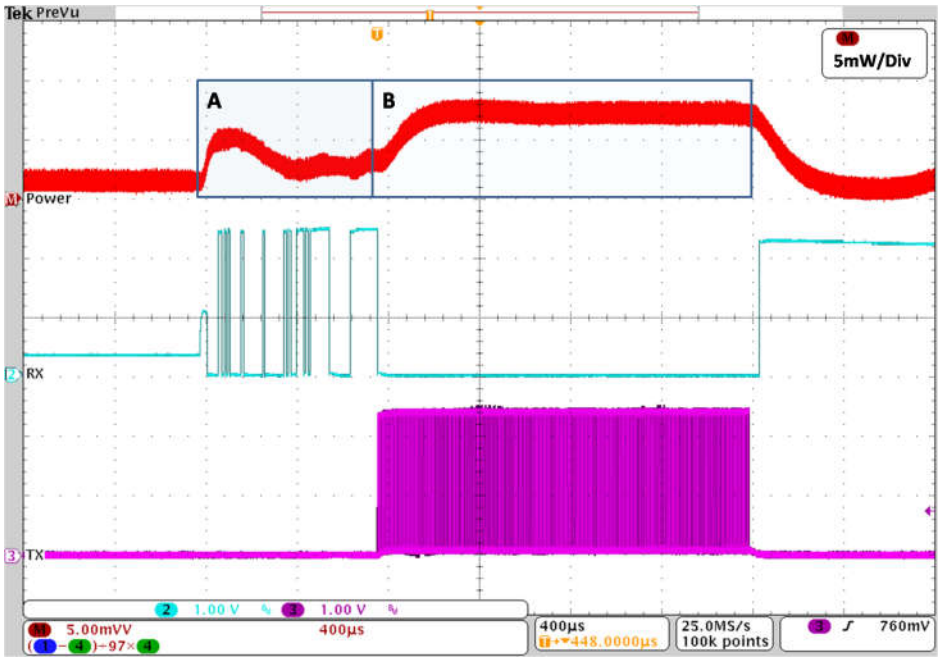

Figure 3.7: Power consumption of NFC communication: The red line is the overall power consumption of the system during NFC demodulation and modulation. It is obtained by measuring the voltage across a 97Ω resistor which is series connected to the power supply feeding the system. The blue line (RX) is the demodulated digital signal(bit rate is $105.9kHz$, it is decoding the 5 bytes REQB (including CRC bytes) command in the figure), the purple line (Tx) is the modulated digital signal (bit rate is $847.5kHz$), it is responding 14 bytes ATQB (including CRC bytes) to the reader. The block A represents the period of demodulation, and block B refers to the period of modulation.

orientation, and motion events are recorded. Once the container and tag is returned to the RFID reader, the recorded data is downloaded via a RFID interface to a host computer for post processing. Additionally, the latest 30 temperature samples are displayed on the E-ink screen. The temperature and 3D acceleration sample intervals can be modified in software, here it is configured for 5 seconds for demonstration purposes.

The operation of the NFC-WISP is similar to the UHF RFID based passive data logger

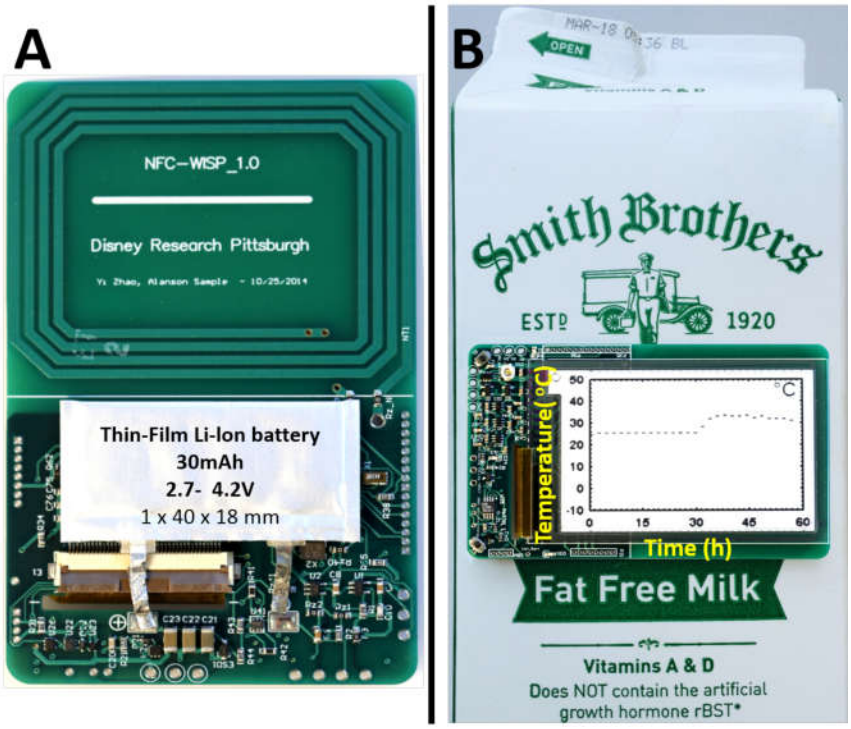

Figure 3.8: Image of a NFC-WISP configured with the E-ink display and rechargeable thin-film battery for monitoring and displaying the temperature of milk, in an example cold supply chain monitoring scenario.

described in [63, 93]. The key difference is that the NFC-WISP allows personnel to both download the food temperature history using a NFC enabled smart phone, as well as visually check the E-ink screen. This is important in cold chain monitoring applications where a person can immediately see the temperature history of a product and can take immediate steps to prevent further food born contamination down the line, rather then waiting for post processing needed for typical data loggers.

The data collected by the NFC-WISP data logger is shown in figure 3.9 which depicts the temperature, 3-axis acceleration, and motion events recorded by the tag over a 15min period. The sampling rate for the temperature and 3-axis acceleration data was 5 seconds and was stored in the internal flash memory on the MSP430. Future implementations could

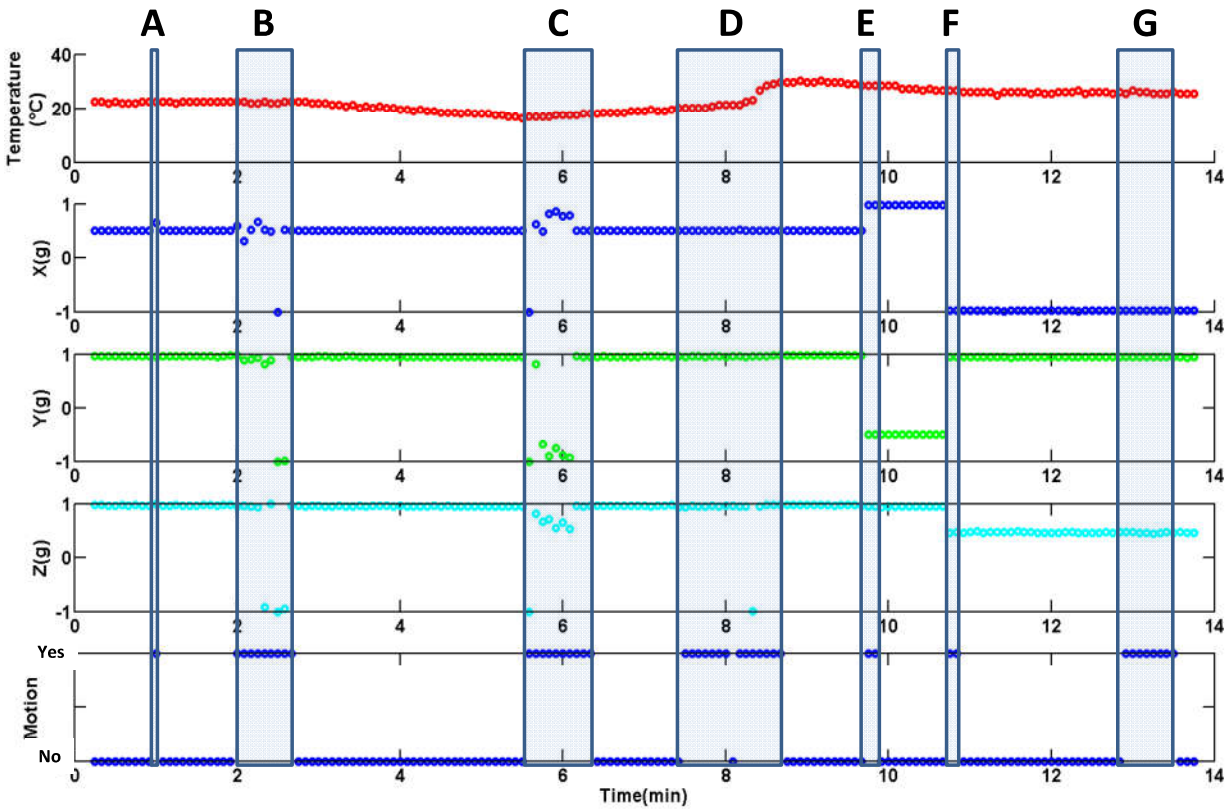

Figure 3.9: Data collected by the NFC-WISP operating in semi-passive mode while monitoring a milk carton.

take advantage of the 2MB onboard FRAM chip to increase the record length. Additionally, the ultra low power motion detection functionality of the ADXL362 was enabled to detect the motion from subtle vibrations to large movements.

As a point of reference figure 3.9 also shows scripted event labels highlighted in light blue. Events A, E, F and G show motion events and changes in orientation, which are correctly detected by the plots of the X, Y, and Z acceleration data and the motion detection plot. During event B the milk carton was placed in a refrigerator and cooled until it was removed

at event C. During event D the milk carton was heated with a hair dryer to simulate a temperature increase that would be seen during transport. Finally, when the experiment was completed the NFC-WISP is place back on the reader and the data is downloaded to a host PC.

3.7.2 NFC RFID + WPT Magnetic Coupled Resonance

One of the key benefits of near-field RFID technology is the ability to wirelessly transfer power from the reader to the tag. Commercially available RFID readers are limited to an output power of 100mW to 200mW due to the modulation of the uplink and downlink data as required by FCC part 15 [27]. However, if data is not modulated on the RF carrier, FCC part 18 [27] regulations state that the permissible output power is unlimited as long as health and safety limits are met in terms of Specific Absorption Rate (SAR).

Recent work on magnetic coupled resonance has shown the ability to transfer 10s of watts, at greater than 80% RF to RF efficiency, over medium distances, in uncontrolled and dynamic environments. This type of wireless power is best suited for the 1-30MHz range and many systems have converged on the 13.56MHz ISM band. Additionally, recent work by Christ et. al. [20] has shown the wireless power transfer based on magnetic coupled resonance can transfer as much as 45-280 Watts (for certain coil configurations) before SAR limits are met. This suggest that it is possible to merge NFC RFID technology with wireless power technology to produce a hybrid solution that can communicate and send low amounts of power in "RFID mode" and then send large amounts of power in "wireless power only mode" to enable fast and multiple device recharging.

A prototype system is shown in Figure 3.10 which depicts four NFC-WISPs being charged wirelessly by a magnetic resonator, with the drive coil and RF amplifier under the table. The wireless power system used is described in detail in [65]. Although the two systems share the same physical layer based on the 13.56MHz ISM band there are significant differences in the near-field coil design and tuning that effects wireless power transfer efficiency. Near-field RFID coils are optimized for data transfer resulting in the need for a higher bandwidth link

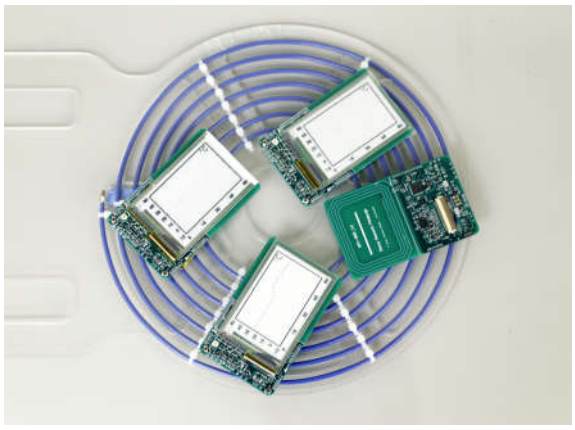

Figure 3.10: Image of four NFC-WISP placed on a magnetically coupled resonant charging coil.

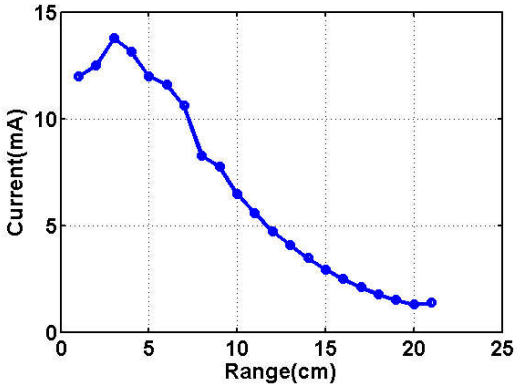

Figure 3.11: Plot showing the amount of current that can be harvested from the wireless power transmitter as a function of distance.

and thus a relatively low quality factor, typically around 20 to 30. This is opposed to high power Magnetically Coupled Resonators (MCR) systems that operate on a single tone and use coils with a quality factor of 100 to 300. The result is that when low Q coils, such RFID tag coils, are used in MRC it is difficult for the combined system to enter the over-coupled regime and optimal power transfer may not be possible.

The NFC-WISP was placed into sleep mode and the rectified current delivered to the $10mAh$ thin film battery was recorded. The Wireless Power (WP) transmitter was set to output a single 13.56MHz tone at 1Watt. The tag was then moved towards the transmitter such that the center of the WP transmitter's coil and the NFC-WISP's coil are aligned. Figure 3.11 shows a plot of harvested current as a function of distance from the WP transmitter. The plot shows that as the NFC-WISP is brought closer to the WP transmitter the amount of current that is delivered to the thin-film battery increases till 4cm when the system becomes over-coupled and the amount of current decreases. It should be noted that the charging current was limited to approximately 10mA to protect the battery.

Chapter 4

SIMULATION OF POWER DELIVERY EFFICIENCY AND COMMUNICATION OF NEAR FIELD WIRELESS POWER PLATFORM

Ubiquitous Near Field Communication (NFC) readers are able to wireless power passive NFC tags with mW power. However, reliable and efficient power-transfer with robust communication in the cm reading range is critical to enable more NFC wireless power applications, and it is vulnerable to the variations of tag reading distance and antenna misalignment. To mitigate these challenges, we present two simulation-based investigations to study this kind of system with considerations of various parasitic effects. Near Field Communication (NFC) readers, ubiquitously embedded in smart-phones, buses and other infrastructures, are able to wirelessly deliver mW-level power to ultra-low power, passive NFC tags via a coupled magnetic field. Additionally, an NFC reader can leverage the coupled communication channel to support relatively heavy computational applications, such as sensing, visual displays, etc. Consequently, reliable and efficient power-transfer with robust communication in the cm reading range is required to enable various more demanding NFC-WISP applications. However, there is a fundamental tradeoff between wireless power delivery and resonator bandwidth, which are critical to NFC communication. Another common trait of magnetically coupled systems is the vulnerability to variations in tag reading distance and antenna misalignment. To mitigate these challenges, we present two simulation-based investigations to study the power transfer and bandwidth performance given different NFC reading range with consideration of parasitic effects. Firstly, we compare a 2-coil NFC system with a 3-coil NFC system via theoretical analysis utilizing a simplified simulation model by ignoring the cross-coupling effect. Secondly, we present the influence of cross-coupling effects of a 3-coil

system using a complex model. Thirdly, we demonstrate the effect of parasitic capacitance across coils for both 2 and 3-coil systems. Final, we compare the performance of both 2-coil and 3-coil system in a practical where the receiver load impedances changes with tag's run-time state. we conclude that the 3-coil system can enable better power delivery at longger range, 2-coil system can enable better reliable communication in most ranges and power delivery in very close range.

4.1 Introduction

Traditional wireless-power systems often target power delivery above 1W of power [56, 88]. Nowadays, as consumer electronic devices demand smaller form-factor and lower power, there is a natural demand for them to be wirelessly powered, due to the consumer applications that require longer battery-life or little to no maintenance effort. Recently, RFID [41,100] and Wi-Fi signals were successfully demonstrated to wirelessly power ultra-low power devices using existing infrastructure. However, the μW level of power transferred by these RF system may not be sufficient for many devices and applications where charging time is critical and power consumption is high. The growing financial payment and access control market utilizing Near Field Communication (NFC) has driven the ubiquitous embedding of NFC readers in smart phones, stores and other infrastructures. A mobile NFC reader normally transmits a few mW power at 13.56 MHz for wireless identification within approximately 3 cm. Our previous work presents a software defined NFC tag called NFC-WISP [101, 102], which not only has an on-board 16-bit micro-controller but also provides sensing ability, display capability and application extendibility. In short, the NFC-WISP harvests RF power from the NFC data generated by the NFC reader, and uses it to operate various applications on the custom NFC tag, such as updating a 2" E-ink display on the NFC-WISP without a battery, nor does it require charging an on-tag battery for the operation of sensing and visualization when the NFC reader is not in its proximity. The available space for the transmitter (Tx) antenna in a mobile NFC reader, such as in NFC-enabled smart phone, is extremely limited; therefore, the Tx antenna normally has an intrinsic quality factor (Q) of around 15 and can generate

around $300\mu W$ of RF power at 13.56 MHz. However, the NFC protocol requires a minimum of approximately 2 MHz of bandwidth to ensure successful communication (it requires a sub-carrier of 847.5 kHz to transmit data at 106 kHz or above). Most near-field wireless power systems are very sensitive in terms of the change in range and antenna alignment. Therefore normal human use, which causes significant range and antenna alignment variation, can severely limit the performance of the system.

However, we don't have the freedom to modify the mobile NFC reader, especially for space-limited NFC-enabled phones, to suit an arbitrary tags power and communication budget. Thus, this paper presents an analytical and simulation-based study discussing optimization of power and communication given design freedom of only the receiver (Rx) with a 1-coil NFC transmitter (Tx).

In Section 4.2, we compare the use of 1 Rx coil or 2 Rx coils given different Q of Rx coil, frequency, range or coupling coefficient. In Section 4.3, we simulate and discuss the effect of indirect coupling between the coil 3 and coil 1 in the 3-coil (1 for Tx, 2 for Rx) system and the parasitic capacitance between each coils. In addition, we concludes about how to optimize the Rx design in terms of maximizing power delivery to the load(PDL) and bandwidth(BW) over the entire reading range.

4.2 Simulation of 2-coil and 3-coil NFC Powered System Using Ideal Model

The circuit model of a 2 or 3-coil NFC wireless power system is presented in Figure 4.1. We simulate the system with three different Rx configurations (one is a 3-coil system and the other two are 2-coil systems) given the same Tx and receiver load (V_s,R_s,C_1,R_{p1},L_1,R_{load} remain constant). The R_{load} is the impedance measured when NFC-WISP in cold start state while using a phone's antenna. The parameter of Tx antenna is measured from google Nexus phone. The overall Q of the wireless coupling link is dominated by the highest Q of the coil in the Rx. In the simulated 3-coil system, the highest-Q Rx coil is L_2, which has a high Q of 70, the 3rd coil connected to the load has a low Q of 45. The two compared 2-coil systems have, respectively, a high Q of 70 and a low Q of 45 in the Rx. The simulation result

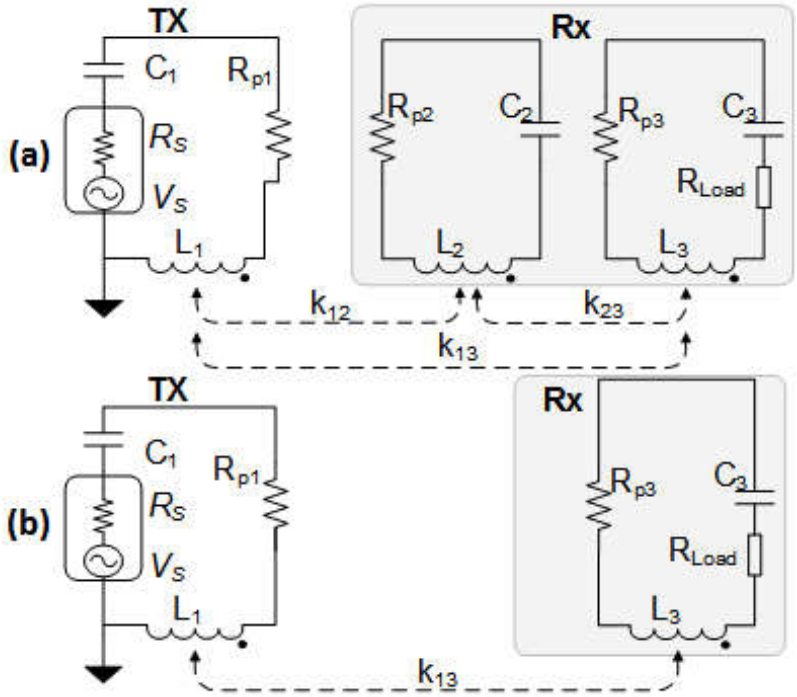

Figure 4.1: Block diagram of NFC wireless power system: (a),(b) refer to 3-coil and 2-coil systems respectively. Tx is the NFC reader, RX is the NFC tag. R_{pi} and C_i are the equivalent resistance and tuning capacitance of the coil i with inductance of L_i. R_s and R_{load} are the source resistance of NFC reader and the equivalent resistance of the loaded hardware in the NFC tag. k_{ij} is the coupling coefficient between coil i and coil j.

given the three configurations is presented in Figure 4.2. The coupling coefficient k_{12} in the 3-coil system and k_{13} in the 2-coil system are indicative of the NFC reading distance and antenna alignment. In the 3-coil system, k_{23} is optimized for maximizing the average Power Delivered to the Load (PDL) over a 3cm Tx-to-Rx range, while k_{13} is ignored to simplify the theoretical analysis. We will discuss the effect of k_13 and other parasitic effects in Section 4.3 the following section.

From maximum power transfer theory, the optimization of the PDL in wireless power system requires conjugate matching between the source impedance of the Tx and the reflected

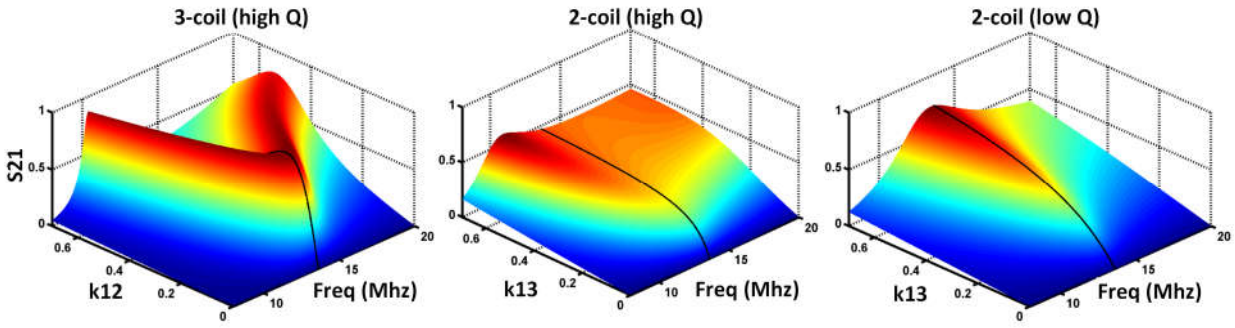

Figure 4.2: Comparison of 2 and 3-coil systems: high/low Q refers to the highest Q of the coil in the Rx. The black line marks the NFC frequency: 13.56 MHz

impedance from Rx coils. Given that all the coils are tuned to resonate at the target NFC frequency, reflected impedance from second coil to the first Tx coil can be represented as follows:

$$\begin{aligned} Z_{ref21_3} &= \frac{w^2 k_{12}^2 L_1 L_{2_3} z_3}{z_2 z_3 + \omega^2 k_{23}^2 L_{2_3} L_3} \quad (3-coil) \\ Z_{ref31_2} &= \frac{w^2 k_{13}^2 L_1 L_{3_2}}{z_3} \quad (2-coil) \end{aligned} \tag{4.1}$$

Z_{refij_n} is the impedance reflected from the coil i to coil j in n-coil system. If the all the coils are tuned to resonate at the target NFC frequency, from (4.1) we can obtain:

$$\begin{aligned} R_{ref21_3} &= \frac{k_{12}^2 Q_1 Q_{2_3} (R_s + R_{p1})}{1 + k_{23}^2 Q_{2_3} Q_{3L_3}} \quad (3-coil) \\ R_{ref31_2} &= k_{13}^2 Q_1 Q_{3L_2} (R_s + R_{p1}) \quad (2-coil) \end{aligned} \tag{4.2}$$

$$
\begin{aligned}
Z_{ref21_3} &= \frac{w^2 k_{12}^2 L_1 L_2}{Z_2 + Z_{ref32_3}} \\
Z_{ref32_3} &= \frac{w^2 k_{23}^2 L_2 L_3}{Z_3} \\
Z_{ref31_2} &= \frac{w^2 k_{13}^2 L_1 L_3}{Z_3} \\
Z_1 &= R_s + R_{p1} \\
Z_2 &= R_{p2} \\
Z_3 &= R_L + Rp3 \\
\eta_{3-coil} &= \frac{Z_{ref21_3}}{Z_1 + Z_{ref21_3}} \frac{Z_{ref32_3}}{Z_2 + Z_{ref32_3}} \frac{R_L}{Z_3} = \eta_1 \eta_2 \eta_3 \\
\eta_{2-coil} &= \frac{Z_{ref31_2}}{Z_1 + Z_{ref31_2}} \frac{R_L}{Z_3} = \eta_1 \eta_3
\end{aligned}
\tag{4.3}
$$

$$
\begin{aligned}
PDL_3 &= \frac{Vs^2}{Z_1 + Z_{ref21_3}} \eta_1 \eta_2 \eta_3 \\
PDL_2 &= \frac{Vs^2}{R_s + Z_{ref31_2}} \eta_1 \eta_3
\end{aligned}
\tag{4.4}
$$

z_i is the total impedance of antenna coil i. If we take the derivative of each equation in 4.1, we can find that both the Z_{ref31_2} and Z_{ref21_3} are increasing function of k,Q_1. Q_{i_n} and Q_{iL_n} are, respectively, the intrinsic and loaded Q of coil i in a n-coil system.

Given the fixed transmitter antenna embedded in NFC enabled phone and NFC-WISP load, we simulate the S21 with two different receiver design in Figure 4.1. To simplify, the 2-coil system (one Rx coil) we talk about later will use the same diagram and subscripts in Figure 4.1, but without the use of center coil 2 (L_2,C_2,R_{p2}). Therefore, in 2-coil system, the k13 represents the coupling between the coil 1 (in Tx) and the single receiver coil 3. k13 in 3-coil system is the indirect coupling between the coil 1 (in Tx) and the second receiver coil 3 (which directly connected to the system load in Rx). We simulates 3 Rx design as shown in Figure 4.2 with a range of k. The center loop, which includes components with subscript of 2, is a purely coupled circuit, which enables data and power optimization of a NFC system. In the two-coil case, this loop is absent from the system, along with its couplings k12 and

k23. The rightmost Rx loop is the output loop of the NFC system. Power and data are recovered from this loop at Zload.

From the second figure of the high Q 2-coil systme, we can see that because the reflected impedance is too high at close range (small k), a matched impedance cannot be achieved using a high Q Rx coil. Therefore the best resonant frequency shifting off the target frequency. Similarly, the best resonant frequency splits into two distinctive modes in a 3-coil system at smaller k. The third subplot shows that a lower Q Rx design of 2-coil system has better power-transfer performance at the $13.56MHz$ than high Q due to its lower reflected impedance.

The maximum PDL (PDL_{max}) over the entire range of k at the operating frequency $13.56MHz$ can be calculated as follows [38] ($\eta_n - coils$ and PDL_n respectiviely refers to the power transfer efficiency and the actual power delivery to the load of n -coil system), η_i means the power transfer efficiency at each single coil i:

Please note that, the Equations (4.1) to (4.4) are modeled in an ideal model where the cross coupling effect in the 3-coil system and parasitic capacitive effect in both system are ignored. In the next section, we simulate and analyze the influence of those effect.

4.3 Simulation of 2-coil and 3-coil System with Parasitic Effects

When the distance between the 2nd and 3rd coil in the 3-coil system is large compared to the axial separation of the 1st and 2nd coil, or they are loosely coupled, we can assume $k_{13} = 0$. However, in the NFC wireless-power applications, especially when using an NFC-enabled cell-phone, the NFC reading range (Tx-to-Rx) is within around $3cm$. Therefore, the 1st and 3rd coil separation can be comparable to that of the two Rx coils' distance in 3-coil system. Therefore, we cannot ignore k_{13} anymore. In addition, as the NFC reading range decreases in the 3-coil system, not only does the k_{13} increases, but also does the parasitic capacitance between the coils, which will influence the magnetic-field coupling. In this case, we use a more general model, with consideration of k13 and parasitic capacitance, to reanalyze the 3-coil (See Figure 4.5). (the 2nd-to-3rd coil distance is empirically below $1mm$ to maximize

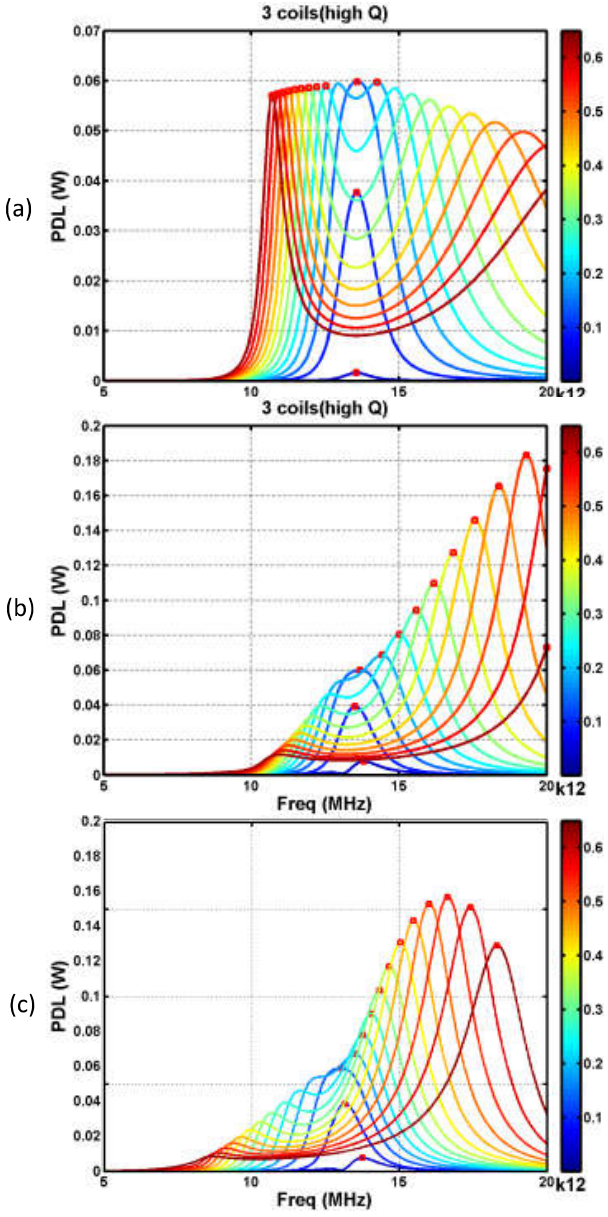

Figure 4.3: 3-coil system

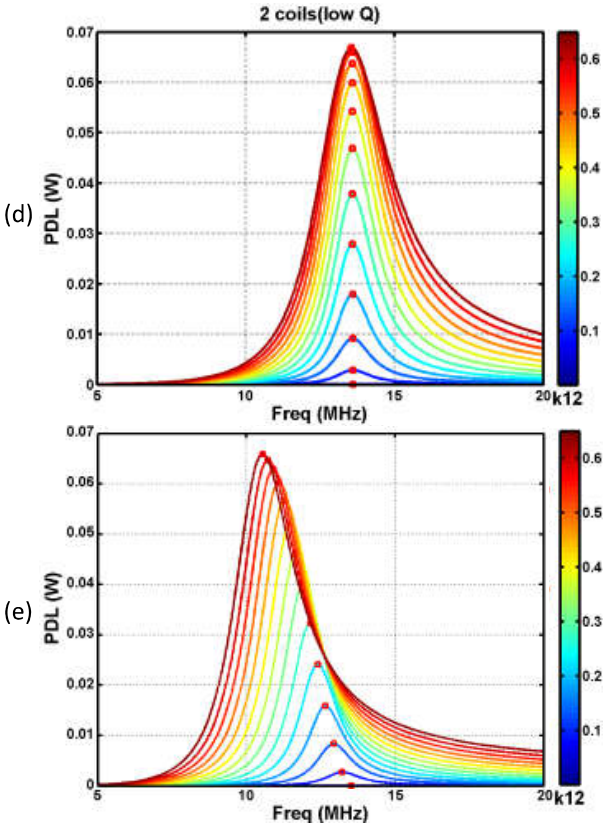

Figure 4.4: 2-coil system

Figure 4.5: PDL for 3-coil and 2-coil systems. (a) PDL ignoring k13,(b)(d) includes k13, but without parasitic capacitance effect, (c) and (e) includes k13 and parasitic capacitance effect

the PDL in our application)

By comparing (a) with (b) in Figure 4.5, we can see that with the inclusion of k13 there is an increasing of the PDL at f_0 given same k12 as well as the PDL_{max} given the frequency higher than $13.56MHz$ (f_0). Besides, the resonant frequency is shifted a few MHz above f_0 at a larger k12 and the PDL when the frequency lower than f_0 is inhibited significantly. It means the coupled current introduced by k13 enhances the higher frequency and diminish the lower frequency, which become more obvious as the reduce of reading range.

Different than the analysis in Section 4.2, the maximum PDL that can be obtained from the high Q 3-coil system over the entire frequency spectrum is larger than that of the low-Q 2-coil system. If we can obtain the maximum PDL using adaptive tuning method [88], a 3-coil system is likely to generate more power than a two coil system even given the same Q, but at a smaller k. In the absence of adaptive tuning, different k will result in different comparison result of 2 and 3-coil system. Adjusting the Q of the coil in either 2-coil and 3-coil system will change the absolute comparison result, but in general, the PDL of 2-coil system is higher than 3-coil system at larger k, but lower at smaller k. The fundamental reason is analyzed in the Section 4.2. In general, the impedance reflection of 3-coil system is more efficient than 2-coil system given same wireless power range. Therefore, the 3-coil system can match the impedance with smaller coupling coefficient comparing the 2-coil system, which requires stronger coupling (higher k) to match the same impedance.

In addition to the effect of k_{13}, the parasitic capacitance introduced by each coil pair generates a strong influence on both 2-coil systems and the 3-coil system with the decreasing reading range (Tx-to-Rx distance). It can be shown by (b)(c) and (d)(e) in Figure 4.5. In both systems, the parasitic effect shifts the entire resonant link as k12 increases. In addition, the maximum PDL of simulated frequency range will be reduced significantly given an equivalent large k12 compared to what if ignores the effect. Although a different estimation of parasitic capacitance on each coil may yield a different amount of frequency shifting and a diminishing of the PDL, the trend is consistent. Due to this effect, the maximum PDL can normally be obtained with a different resonant frequency other than f_0 for both 2 and

3-coil systems. In practice, we normally detune the Rx coils at a lower frequency (12.5 MHz) to obtain the best PDL at a particular NFC reading range. Even considering the effect of parasitics, the maximum PDL of a 3-coil system over a simulated frequency spectrum is still larger than that of a 2-coil system. However, since the 3 coil system is normally shifted more than the 2-coil system, it may be more sensitive to the variations in the NFC reading range and therefore require a larger initial detuning frequency.

4.4 System Performance Analysis and Optimization

When consider all parasitic effects, we dutune the receiving coils of both 2-coil and 3-coil system to the same frequency lower than the operating frequency in order to optimize the power and communication performance at NFC operating frequency. figs. 4.6 and 4.7 shows the simulated system performance after detuning. In general, 3-coil system performs better at longer range while 2-coil system is better at close range.

From the fig. 4.6, we can find that the 3-coil system has better resonant bandwidth as well as PDL_{fc} at smaller k12. However, as the k12 increase, the bandwidth of the 2-coil system become larger than 3-coil's. As what we mentioned in Section 4.3, the higher the k12 the larger the shifting of the resonant frequency is. Therefore, to ensure NFC communication robustness given k12 larger than 0.3, a larger bandwidth is critical, otherwise, the communication may fail at particular close reading range. In general, low Q 2-coil system performs better in terms of communication at close range. In addition, from the PDF_{fc} plot, we can see that, 2-coil system has better power delivery performance at larger k12, too. In general, slightly increase of the Q of the receiving coil in 2-coil system can improve the maximum PDF_{fc} at critical coupling [56], but it will still smaller than the comparable 3-coil system. Besides, it will then limit the maximum bandwidth and push the critical coupling coefficient k12 smaller. Therefore, in theory, if we can combine the feature of the two system, such as, swithching between one of the system at runtime, we can obtain better PDL at wider range.

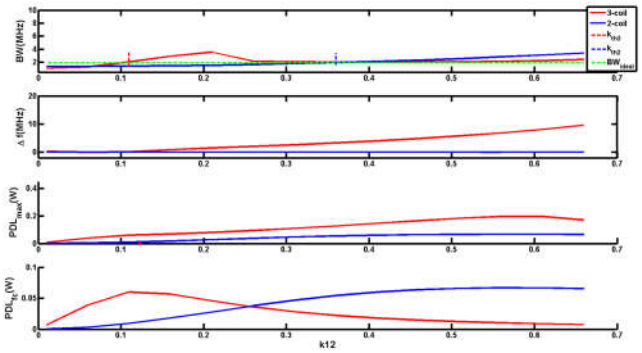

(a) tuned at 13.56MHz, without parasitic effect

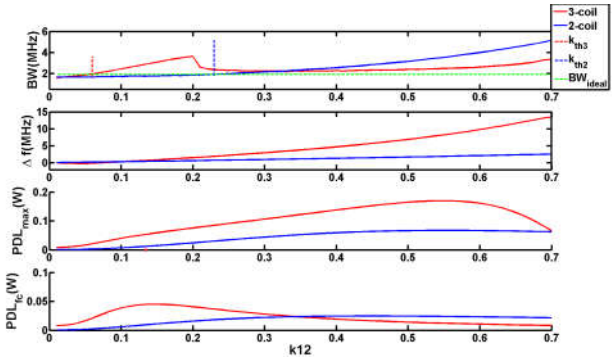

(b) detuned at 12.5MHz, with parasitic effect

Figure 4.6: System performance with/without parasitics and detuning receiver antenna:BW_{ideal} refers to ideal 2MHz bandwidth required by NFC communication; the BW referes to the minimal bandwith of highest resonant frequency instead of NFC operating frequency, it will shift away from the NFC frequency as the increase of k_{12}; k_{th2},k_{th3} point out the k12 when the BW becomes above BW_{idea}; the vertical range of k_{th2},k_{th3} indicates the total bandwidth range of each system. Δf is the frequency offset of highest resonant frequency to 13.56 Mhz (NFC operating frequency). PDL_{max} is the maximum PDL at the resonant freqnecy. The PDL_{fc} refers to the PDL at NFC operating frequency 13.56MHz

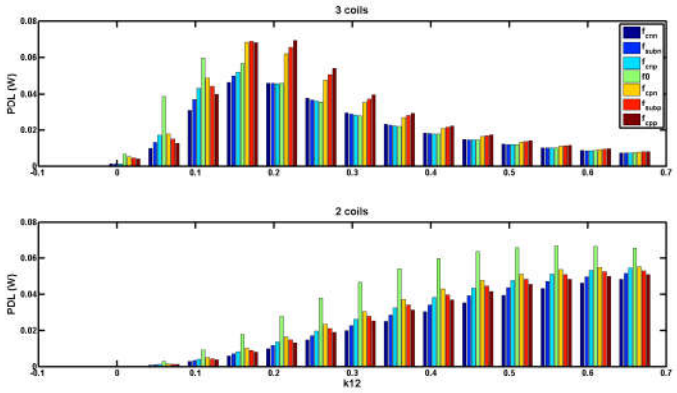

(a) tuned at 13.56MHz, without parasitic effect

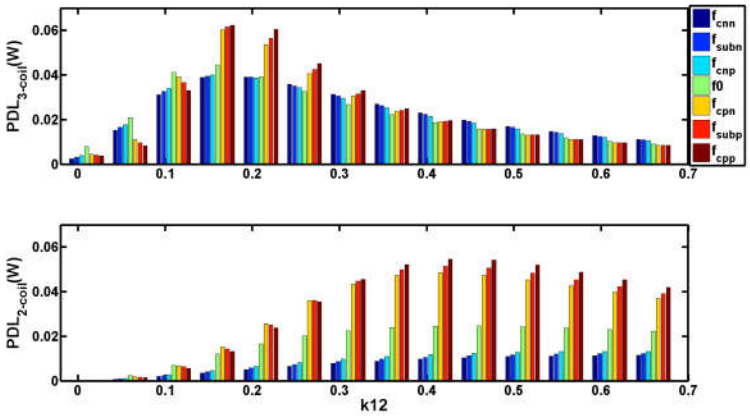

(b) detuned at 12.5MHz, with parasitic effect

Figure 4.7: PDL of NFC communication spectrum (with cross coupling), $f0 = 13.56MHz$, $f_{sub} = 847.5KHz$, $f_{data} = 105.9KHz$, $f_{subn} = f0 - f_{sub}$, $f_{subp} = f0 + f_{sub}$, $f_{cnn} = f_{subn} - f_{data}$, $f_{cnp} = f_{subn} + f_{data}$, $f_{cpn} = f_{subp} - f_{data}$,$f_{cpp} = f_{subp} + f_{data}$.(k12 refers to the Tx-to-First Rx coil in all systems)

Chapter 5

EXPERIMENT AND ANALYSIS OF A NFC PHONE POWERED SYSTEM

Near Field Communication (NFC) readers, ubiquitously embedded in smartphones, buses, and other infrastructures, can wirelessly deliver mW-level power to ultra-low power, passive NFC tags to enable applications, such as access control, inventory management, and financial payment. Traditionally, one multi-turn loop coil is used in both NFC transmitter (reader or phone) and receiver (tag) to establish magnetic coupling for power delivery as well as in-band communication. In our previous work [101], we prove that the NFC power obtained from the cell-phone can enable more power-hungry computation and sensing applications compared to conventional approaches. Additional simulation of multi-coil wireless power systems [98] in the previous section prove that we may be able to detune a two-receiver-coil tag in a 3-coil system to achieve higher power delivered to the load (PDL) given a certain range. However, its small communication bandwidth may result in limited communication range due to the large frequency shift. The single-receiver-coil in a 2-coil system can enable robust communication, but it will lead to limited PDL compared to 3-coil system. Therefore, we propose a switchable receiver coil design embedded in NFC-WISP, which can dynamically adapt to the requirement of each task in run-time by switching between 2-coil and 3-coil modes, to optimize PDL and communication for demanding, power hungry NFC phone powered applications.

5.1 Introduction

In traditional near-field wireless power systems [86], using different numbers of coils (generally 2-4 coils in total) will result in different power transfer properties. In a nutshell, the more

coils used, the more parameter knobs are available for system optimization, such as to obtain the highest power deliveried to the load. From the analysis in the previous section, we find that, in general, the 3-coil system (with one high Q loop and one low Q load connected coil on the receiver) can deliver more power at smaller k (far range). However, the 2-coil system (single low Q receiver coil) has wider resonant bandwidth and better performance when k is very high. However, a high k larger than 0.65 may not be even achievable in practice using the antenna embedded in a typical cellphone and that in the NFC-WISP. In addition, a common assumption of wireless power system used in the literature is that the load impedance in the receiver is constant [38] and normally ignore the limitations of in-band communication. Therefore, the optimized antenna design in these literatures [38, 86] only talks about optimization method given a fixed load or range. However, those assumptions in prior wireless power research can not be true for passive near field communication-powered sensing or computing applications.

The work presented in this dissertation uses NFC-WISP as an example to illustrate the challenges of NFC phone powered wireless power systems and a method to ensure high power delivery as well as high bandwidth communication in different operation states. Unlike conventional wireless power system, The NFC reader (or NFC-enabled smartphone) powered NFC-WISP platform has distinct features and limitations because of the usage of mobile reader and NFC communication protocol, particularly when the reader is also implemented by a typical highly-constrained smartphone. Firstly, the max coupling coefficient k between the smartphone reader and NFC-WISP is estimated below around 0.42. Secondly, the NFC protocol (here we use ISO-14443) requires a resonant bandwidth as low as 1.908MHz [6], which is much higher than conventional wireless power systems [86]. Thirdly, if considering actual NFC reader use case, the wireless power range varies with humans' usage. Therefore the design of the coils should be less sensitive to the change in relative antenna location. Finally, because the load impedance of the NFC-WISP varies with different hardware and software operation states, the design of the inductively coupled wireless power system should ideally be less sensitive to the change of load.

In general, in order to enable more applications, the passive computationally-enhanced NFC platform (NFC-WISP) normally has to be heavily duty-cycled in order to store enough energy for running tasks whose power consumption is much higher than its incoming charging power. Insufficient harvested power when NFC-WISP is running high power (above 3mW) tasks will result in a brown-out event. For example, updating an active E-ink display may require buffering a large amount of energy in a large capacitor and maintaining high PDL (power delivered to the load) during run-time, because the maximize power consumption during display updating is around $30mW$, while the previous NFC-WISP is only be able to obtain an average of 3mW power. Maintaining the power supply of NFC-WISP at sufficient levels using duty cycling is essential for finishing power hungry and long duration applications. Therefore, PDL has to be optimized to obtain the highest power to enable power-hungry applications. However, when the NFC-WISP exchanges data with the reader, especially during up-link (NFC-WISP to reader) communication, the performance of communication link has a higher priority than wireless power performance. Keeping larger communication bandwidth and better S11 is important during NFC-WISP communication; Large bandwidth will make the inductive coupling of the NFC system become less sensitive to the changes in relative antenna position and better S11 will result in better SNR (signal-noise-ratio) in decoding load modulation in up-link. Therefore, the bandwidth or Quality factor (Q) optimization requirements varies with different processes in run-time.

In addition to the fact that the power and bandwidth requirements vary between tasks, the load impedance of the NFC-WISP varies in run-time as well. Adaptive tuning methods typically implemented in the power transmitter uses frequency tuning [86, 88] or impedance tuning to compensate for the change of load impedance or k (coupling coefficient). In the application using NFC-WISP, the change of load typically occurs within a short period (a few ms). The deployment of adaptive tuning methods in NFC readers would not only be expensive but would also lead to a long control delay. In addition, frequency tuning violates both the NFC protocol and FCC regulations. Therefore, we propose a low cost receiver antenna design in this chapter to adaptively adjust to the different system requirements and

variance of performance.

In this section, we present a method which utilizes switchable receiver coil to improve the wireless power delivery efficiency and obtain reliable NFC communication with different running processes and receiver loads. Firstly, a theoretical analysis of power delivered to the load in both 2-coil and 3-coil system is discussed. Secondly, a simulation work considering the variation of receiver load is presented. Thirdly, we implement the proposed method in a new version of passive NFC-WISP which uses two receiver antennas in a flexible PCB and the 2-coil/3-coil switching method to allow updating a larger display 2.7 inch given a tunable range.

5.2 Theoretical Analysis with Load Impedance Variation

From Equation (4.2), we can simplify the reflected impedance from the load to the transmitter antenna in both 2-coil and 3-coil systems as follows: The Q_{2L_3} refers to the loaded Q of the load-connected receiver coil in a 3-coil system, the Q_{3L_2} refers to the loaded Q of the only receiver coil in a 2-coil system. As long as Q_L is not too big, in general, the Q_{2L_3} is larger than Q_{3L_2}. Only when the RL is much smaller than the antenna parasitic resistance R_{p1}, the Q_{2L_3} will become larger than Q_{3L_2}. That means, in general, by adding a coil, the same load on the receiver of a 3-coil can result in a higher reflected impedance as seen by the transmitter, compared to a 2-coil system. That explains why, in the previous simulation, the 3-coil system has better wireless power efficiency in the far range (small k) while the 2-coil system has better performance in close range(large k). The maximized power delivery efficiency happens when the reflected load impedance matches the source impedance of the transmitter. We call the coupling coefficient and Tx-to-Rx distance where the n-coil system can match the transmitter source impedance as k_{mn}, d_{mn}. Since the reflected load impedance is an increasing function of k (k_{13} in 2-coil system, k_{12} in 3-coil), the 3-coil system is likely to match the same source impedance at smaller k (longer distance). However, when the receiver load R_L is too small (similar or smaller than R_{p1}), Q_L becomes extremely large and dominant than Q_{L3}, therefore resulting in larger reflected impedance in 2-coil system rather

than 3-coil sytem at smaller k. However, in this case, the best impedance matching happens at much smaller $k_m n$ with large d_{mn}, where, the absolute power delivery to the load (PDL) become much smaller due to the long signal propagation distance. Compared to the case where the R_L is medium and large, the PDL of when R_L is too small over the same NFC reading range (0 3cm) is much smaller. A medium R_L can achieve impedance matching at bigger k_{mn} or smaller $d_m n$, thus resulting in large PDL.

$$
\begin{aligned}
R_{ref21_3} &= k_{12}^2 Q_1 Z_1 \times \frac{Q_{2_3}}{1 + k_{23}^2 Q_{2_3} Q_{3L_3}} \quad (3 - coil) \\
&= k_{12}^2 Q_1 Z_1 \times Q_{2L_3} \\
Q_{2L_3} &= \frac{Q_{2_3}}{1 + k_{23}^2 Q_{2_3} Q_{3L_3}} \\
Q_{3L_3} &= \frac{Q_{3_3} Q_L}{Q_{3_3} + Q_L}
\end{aligned} \tag{5.1}
$$

$$
\begin{aligned}
R_{ref31_2} &= k_{13}^2 Q_1 Z_1 \times Q_{3L_2} \quad (2 - coil) \\
Q_{3L_2} &= \frac{Q_{3_2} Q_L}{Q_{3_2} + Q_L}
\end{aligned}
$$

In most wireless power systems, the receiver antenna is designed to not only optimize the impedance matching to the transmitter, but also to match the load impedance, which determines the optimal distance d_{opt} where PDL is maximized. In the 2-coil system, not all possible values of impedance for the transmitter and receiver can be matched given particular load R_L within the range d. In the 3-coil system, because of the use of one additional coil, we have more knobs to turn (k_{23}, Q_2) to optimize the impedance matching given any load R_L within the same range d. The desired NFC reading range is within 3cm. Therefore, in the revision of NFC-WISP design, we use an empirical k_{23}, which is optimized for obtaining better impedance matching over the target NFC-WISP reading range.

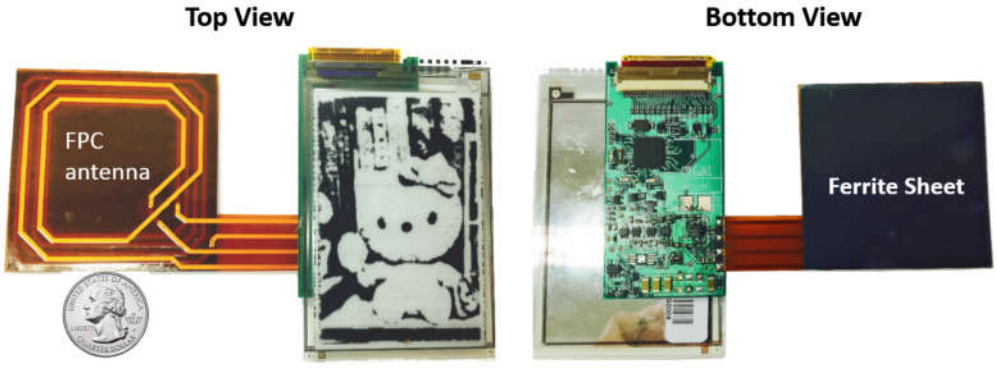

Figure 5.1: Prototype of new passive NFC-WISP with flexible 2-coil receiver antenna and 2.7" E-ink display

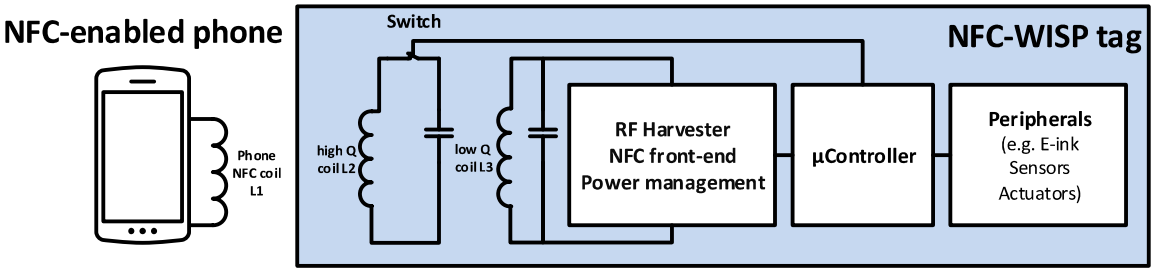

Figure 5.2: Architecture of passive NFC-WISP 2.0

5.3 NFC-WISP with Switchable Receiver coils

In the simulation work presented in the previous section, the load impedance R_L is a constant value. However, in practice, the load impedance R_L changes between different tasks. For example, in the cold start state, the NFC-WISP begins from zero power to powered on after harvesting enough energy. The load impedance R_L of the NFC-WISP in this state is represented as $R_{L_{coldStart}}$ (around 1 ohm in our measurement). However, after the NFC-WISP is been charged up and enters sleep mode, waiting for NFC reader interaction, the load impedance R_L of the NFC-WISP becomes $R_{L_{sleep}}$, which is larger than $R_{L_{coldStart}}$ in our measurement. When the NFC-WISP is running power-hungry tasks, such as updating E-ink display (E-ink updating mode) or transmitting data to the NFC-enabled phone (Tx mode), it will draw a lot of current (typically around $1 - 5mA$) from the on-board power supply, the R_L of the NFC-WISP then becomes $R_{L_{E-ink}}$ and $R_{L_{Tx}}$, which are bigger than $R_{L_{sleep}}$. (Please note that all the load impedance R_L mentioned above is equivalent serial impedance measured from Vector Network Analyzer given 13.56MHz transmitted frequency and the imaginary impedance is matched with tuning capacitor).

Therefore, the problem becomes: Given a particular R_L, how does one choose the receiver antenna configuration (single receive coil or two) to optimize power delivery efficiency as well as keep communication performance within the targeted NFC-WISP-to-Reader range (around 3cm). We design a revision of NFC-WISP with switchable flexible antennas which can be switched to a low Q receive mode with a single receive coil (2-coil system) by opening the middle coil $L2$, and be switched to high Q receiver mode with two receive coils (3-coil system) by closing the middle coil loop $L2$ (see Figure 4.1). The architecture and prototype of the new NFC-WISP are shown in figs. 5.1 and 5.2. We use a Google Nexus phone as our NFC reader. The measured parameters of the smartphone and NFC-WISP is presented in Table 5.1.

Considering all the parasitic effects mentioned in the previous chapter, the simulated power delivered to the load (PDL) when the NFC-WISP is in different states is illustrated

in Figure 5.3. From the simulation result, we can find that when $R_L = R_{L_{coldStart}}$, the PDL value becomes very small because we use a parallel-connected tuning capacitor for tuning the NFC-WISP, which results in a small equivalent serial $R_{L_{coldStart}}$. A better matching network is suggested in the future work section to convert the load impedance to an optimized R_L in order to improve the overall PDL.

5.4 Simulation and Measurement Results

Table 5.1: cell phone and NFC-WISP measurements

R	Ω	**R**	Ω	**L**	μH	**coil Q**		Q_{3L}	
$R_{L_{coldStart}}$	1	R_{p1}	7.7	L_1	1.48	Q_1	16.4	cold start	13.5
$R_{L_{sleep}}$	18	R_{p2}	6	L_2	1.56	Q_2	22.2	sleep	1.9
$R_{L_{Tx}}$	34	R_{p3}	1.77	L_3	0.44	Q_3	21	tx	1
$R_{L_{E-ink}}$	43	R_s	18					E-ink	0.8

From Figure 5.3, we can conclude that, in general, given similar R_s as in Table 5.1 and when the R_L is around 18-43 ohm, the 3-coil system (two receiver coils) has better PDL when k_{12} is around $0 - 0.45$, and the 2-coil system has better PDL when k_{12} is above 0.45. The theoretical reason is explained in the previous section. The measured reading range between NFC-WISP and phone $(0 - 3cm)$ results in a calculated k_{12} of $0.42 - 0$. This suggests that the NFC-WISP is best configured as a two receiver coil (to form a 3-coil system) when power performance is a higher priority than communication. But if a certain application requires highest PDL when the achievable $k12$ is around $0.42 - 0.65$, then 2-coil low Q system is suggested. Note that the increase of R_L will change the threshold of k_{12} where the PDL of the 3-coil system and the 2-coil system are equal. The simulation model used in Figure 5.3 is based on Figure 4.1, which doesn't include the nonlinear behavior of the rectifier and switch nor the interference of the smartphone substrate. Therefore, the measurement result is a

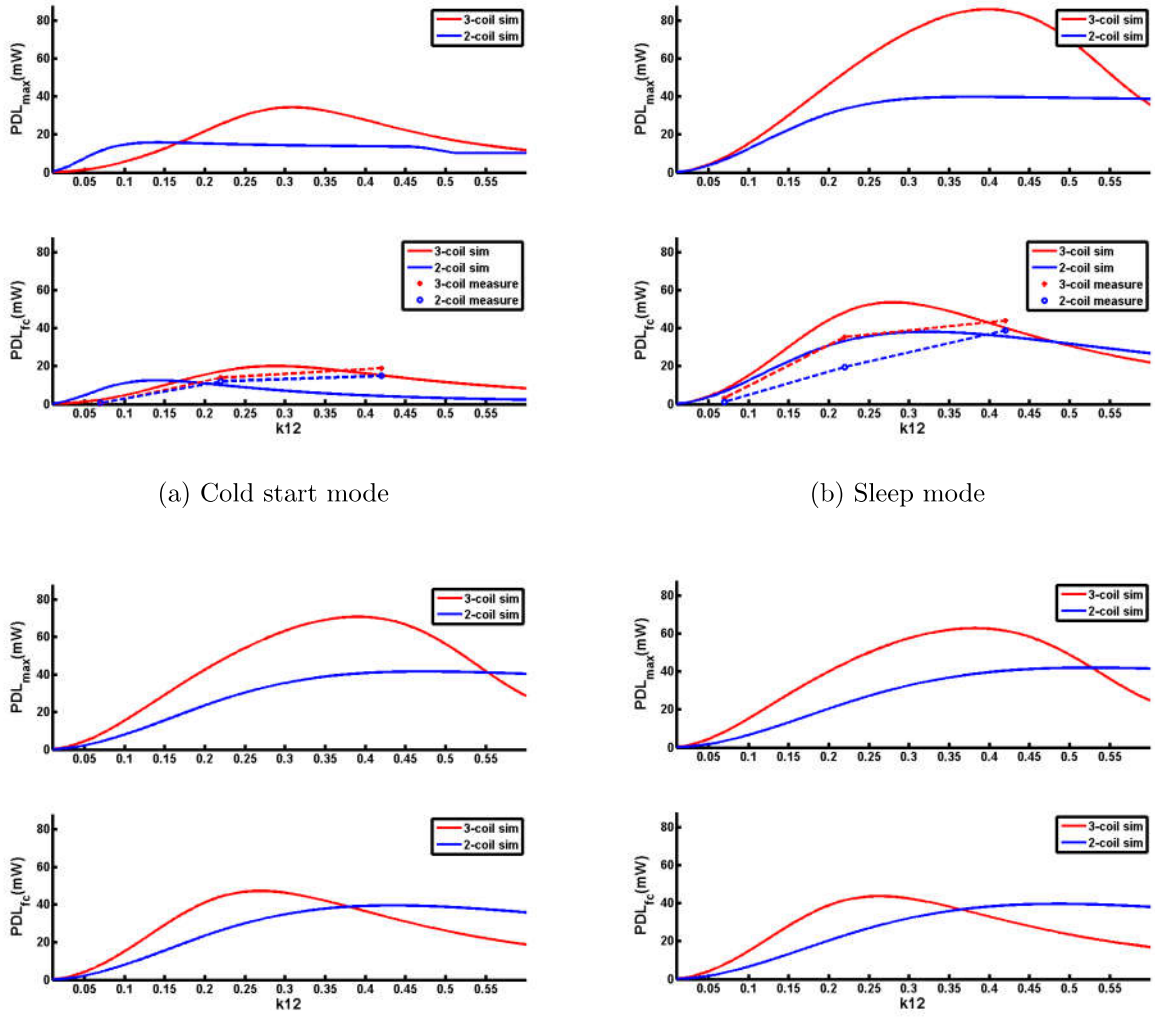

(a) Cold start mode

(b) Sleep mode

(c) Tx mode

(d) E-ink updating mode

Figure 5.3: new NFC-WISPs simulated and measured PDL (includes antenna parasitic effects and detuned L_2): PDL_{max} is the maximum PDL at the resonant frequency, not always 13.56MHz, when using frequency tuning. The PDL_{fc} refers to the PDL when only transmitting a 13.56MHz signal from the NFC reader. The simulated k_{12} is between $0-0.6$, however, in the NFC-WISP system k_{12} is around $0-0.42$ in practice; the cell phone case and substrate lead to a reduction in the practical maximum of k_{12} to less than 0.42

little different than the simulation.

In general, the frequency of the max PDL will shift away from its original tuning frequency with an increase in k_{12}. That is because the parasitic capacitance effect and cross coupling effect become dominant as the range reduces. By detuning the 3-coil system to a lower frequency rather than to $13.56MHz$, we can shift the NFC-WISP working range. In our experiment, if we detune the receiver coil to 12MHz, we can shift the NFC-WISP reading range from $2.8-3cm$ to $0.8-1.65cm$. Typically, the PDL and communication performance, particularly the up-link, are very position-sensitive in 3-coil system, mainly because of the larger frequency shifting caused by higher Q. An empirical suggestion is to detune the NFC-WISP at 12MHz given small k_{12} in order to optimize the PDL within the entire range of $0.5-2cm$, which is sufficient for updating the 2.7" inch display (more than 16mJ energy consumption). In conclusion, decreasing the tuning frequency of only high Q receiver coil can shift the optimization distance of power and communication in 3-coil systems. But the high Q 3-coil system in general is very sensitive to changes of relative antenna position.

Typically, the NFC-WISP communication range is mainly limited by its up-link. During the up-link (from NFC-WISP to Phone), the 3-coil system experiences a bigger frequency shift compared to the 2-coil system, because the 2-coil system has lower system Q. Lower system Q is not good for maximizing PDL, but lower Q can ensure more robust communication because of its wide bandwidth as well as smaller frequency shift. From Figures 5.4 to 5.7, we can also see that the 2-coil system normally has better S11 even when considering the frequency shifting effect in Tx mode. At least 1.908 MHz bandwidth is required by NFC protocol. Better S11 will result in higher SNR (signal to noise ratio) during load modulation. Therefore, the 2-coil system has better communication performance in terms of good SNR as well as being less sensitive to change of relative antenna position.

Different applications may have distinct priorities in regard of power and communication performance. From our simulation and measurement results (Figures 5.3, 5.6 and 5.7 and table 5.2), we can see that we can switch to a 2-coil configuration in Tx mode and enable a 3-coil configuration in other modes to achieve both higher PDL and better communication.

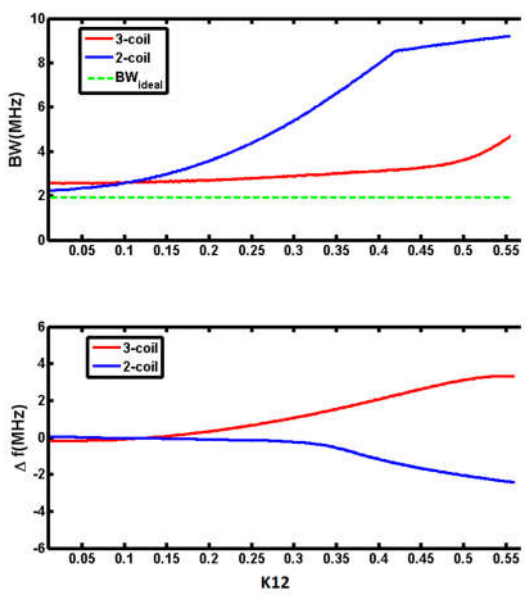

(a) Resonant bandwith and frequency shifting in Tx mode(simulated)

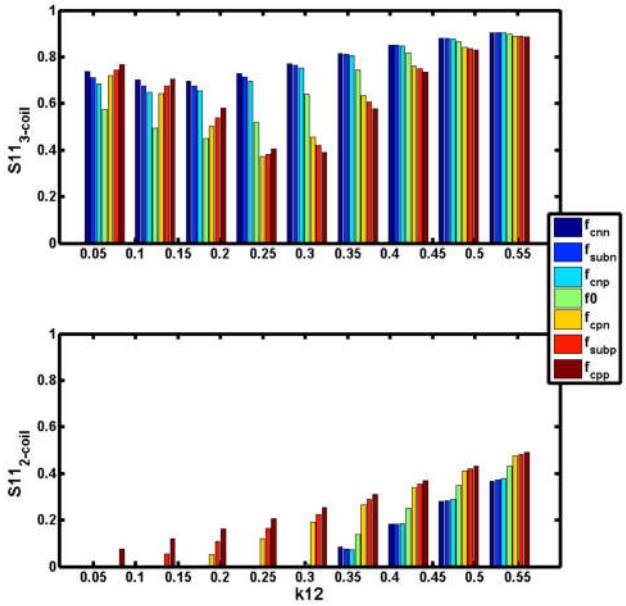

(b) S11 of NFC-WISP in Tx mode (Simulated)

Figure 5.4: (a) is the bandwidth performance (includes antenna parasitics and detuned L_2: BW_{ideal} refers to minimum bandwidth required by NFC protocol; the BW refers to the bandwidth of highest PDL (even when two resonant frequency appears) at resonant frequency, the resonant frequency normally shift away from the NFC frequency as the increase of k_{12}; Δf is the frequency offset of the highest resonant frequency to 13.56 MHz. In NFC-WISP system, it is around $0 - 0.4$. (b) is the S11 of NFC load modulation spectrum, $f0 = 13.56MHz$, $f_{sub} = 847.5KHz$, $f_{data} = 105.9KHz$, $f_{subn} = f0 - f_{sub}$, $f_{subp} = f0 + f_{sub}$, $f_{cnn} = f_{subn} - f_{data}$, $f_{cnp} = f_{subn} + f_{data}$, $f_{cpn} = f_{subp} - f_{data}$,$f_{cpp} = f_{subp} + f_{data}$. (k12 refers to the Tx-to-First Rx coil in all systems)

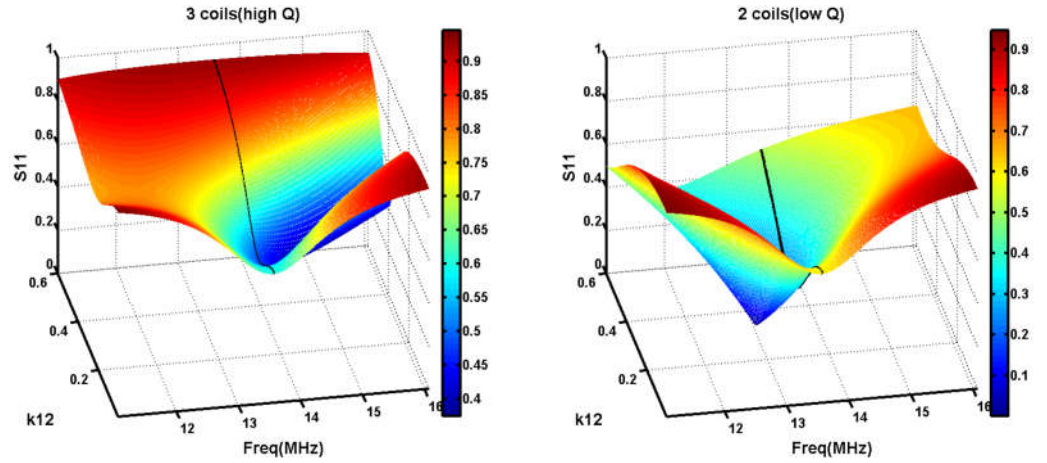

(a) S11

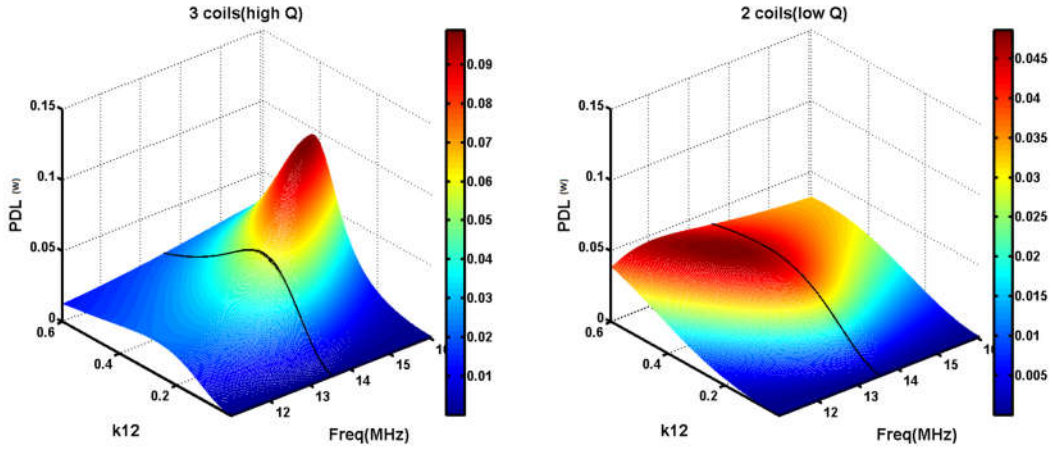

(b) PDL

Figure 5.5: S11 and PDL comparison in Tx mode

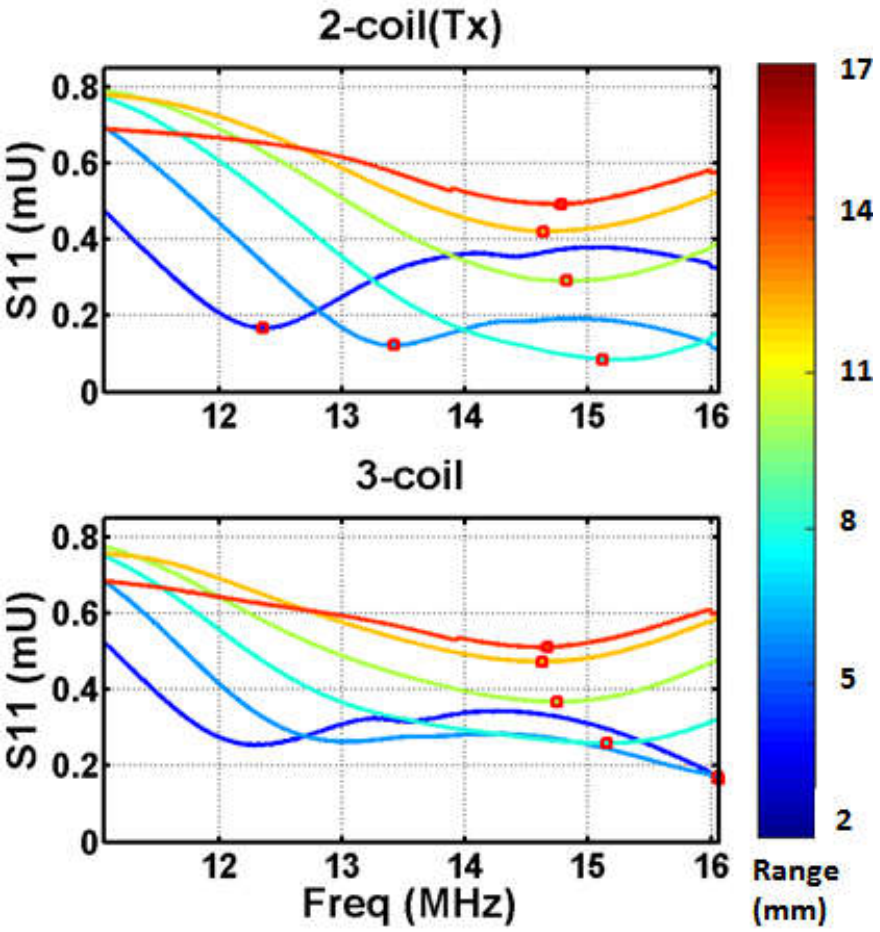

(a) Measured S11

Figure 5.6: Measured S11 when the NFC-WISP is in Tx mode (given constant VNA output power instead of constant transmitted voltage), d12 is phone-to-NFC-WISP reading distance, estimated k12 is 0.42,0.36,0.3,0.25,0.16 when d12 is 2,5,8,11,17 mm

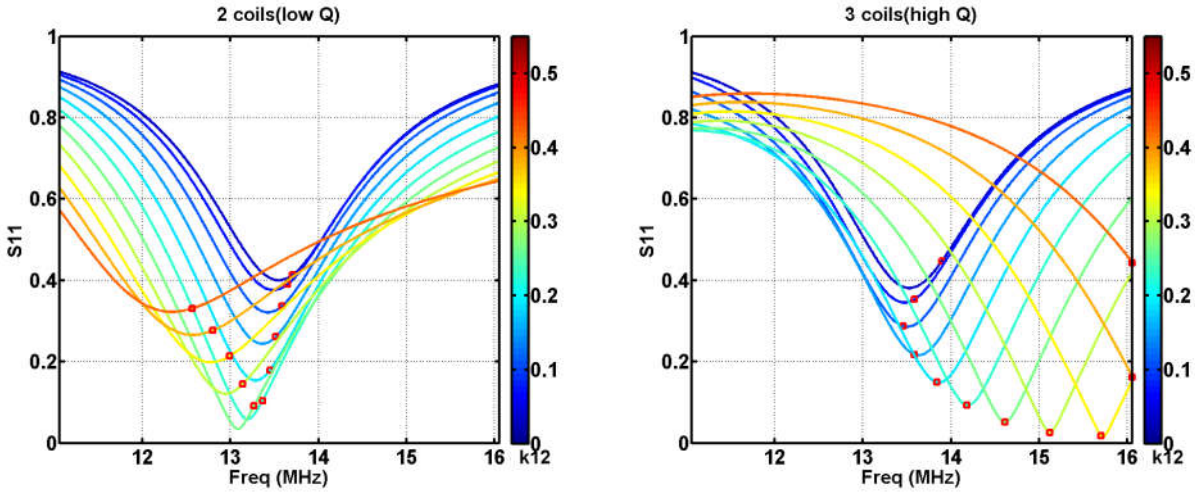

(a) (b)

Figure 5.7: Simulated S11 of the 2-coil and the 3-coil system in Tx mode (when $R_L = R_{L_{Tx}}$)

Table 5.2: PDL measurement comparison between the 3-coil and the 2-coil configurations in sleep mode

Reading range	**Estimated k_{12}**	**Sleep mode (3-coil)**	**Sleep mode (2-coil)**
$0.2cm$	0.42	44.16mW	39mW
$1.25cm$	0.22	35.4mW	19.57mW
$3cm$	0.07	3.1mW	1.0mW

By implementing this proposed method, we can use the newly revised NFC-WISP to update a 2.7 E-ink display within $0 - 1.5cm$ range while keeping robust communication. The old NFC-WISP hardware can only provide sufficient power to update a 2.0 E-ink display within $0 - 0.5cm$. The 2.7 display consumes around $16mJ$ energy, which is two times higher than the 2.0" display. In conclusion, a low Q 2-coil system generates low PDL at far range, is less position sensitive, and has good communication performance because of lower Q. However,

the 2-coil system, in general, is very sensitive to changes in load R_L. The high Q 3-coil system can ensure higher PDL and communication at long range, and is less sensitive to changes in load R_L. But the 3-coil system is very sensitive to changes in relative antenna position. Detuning the high Q coil can change the optimal reading position where the power performance can be maximized. By switching between low Q 2-coil and high Q 3-coil configurations in a application, we can obtain both optimized power and communication performance.

Chapter 6

CONCLUSION AND FUTURE WORK

This dissertation has focused on developing two kinds of RF wirelessly powered computation enhanced system using existing commercial infrastructure; one is far field RFID reader powered self-localized WISP tag, and the other is NFC phone powered software defined NFC-WISP tag. For each of these platforms the operating distance and the deliverable power are very different. The dissertation analyses the feature, challenge and trade-off of typical RF wirelessly powered applications in both far field and near field. This analysis can offer potential to enable more battery-free applications by using RF wireless power or provide a reference to optimize the system design of RF wirelessly powered systems in both far field and near field.

6.1 A Comparison of Far Field and Near Field Systems

In RF wireless power systems, such as sensing, display and computation enhanced RFID or NFC systems, the limited harvested power is the critical constraint, especially when power-hungry tasks and high-accurate sensing or high update-rate are required. In general, in near field systems, the tag's reading range is within a few centimeters, like the NFC-WISP. It can harvest much more power than the far field system (Figure 6.1) given same transmitted power. This is due to different properties of wireless power between near and far field systems. Figure 6.1 roughly demonstrates the power relationship between the near field wireless power system (uses the NFC-WISP as an example) and the far field wireless power system (uses the UHF WISP as an example). Some task examples with their power consumption are marked in the Figure 6.1, too.

In the far field system, the harvested power decreases at a rate of $\frac{1}{r^2}$ when the range r

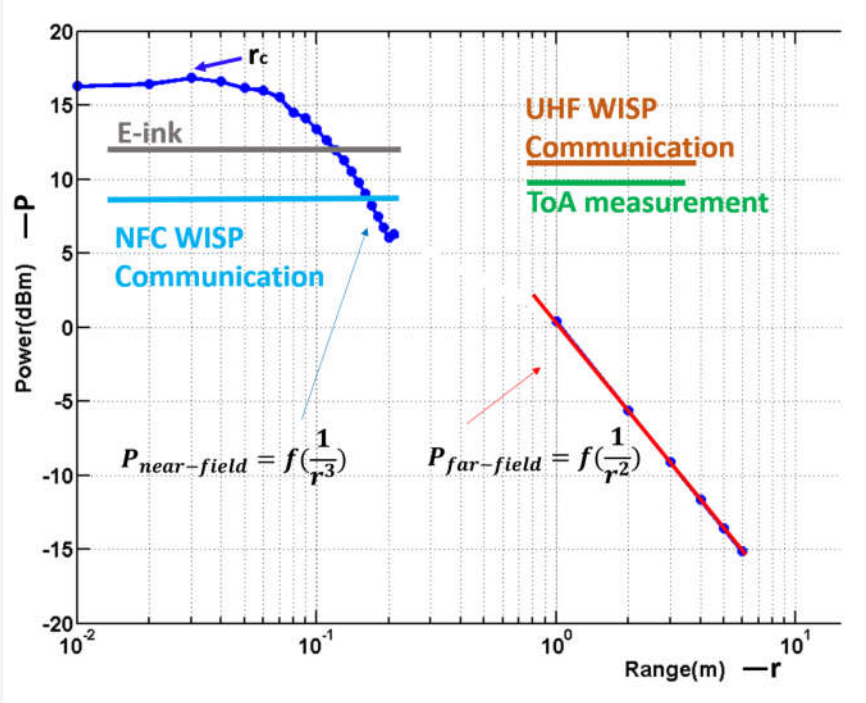

Figure 6.1: Demonstration of the harvested power and power consumption of the UHF-WISP and NFC-WISP given 30dBm transmitted power, the horizontal line indicates the power consumption for different tasks

increases. But, in general, the power decreasing rate of the far field system is slower than the near field system [57]. However, the overall harvested power is a few tens to hundreds of times smaller than the near field system. The far field system uses electrical fields while the near field system uses electrical field for transmitting energy. Besides, the communication is relatively expensive within the UHF WISP reading range in regard of power. Other sensing tasks (like the ToA (Time of Arrival) measurement in Sense WISP) is power-expensive, too. Therefore, small duty-cycled sensing or operation is essential for far field system. In general, the update rate and performance of power-hungry tasks are strongly correlated with the maximum available power, which is proportional to the $\frac{1}{r^2}$ ($r = Range$). In our analysis, we uses UHF acoustic localization WISP to show the trade-off of a typical far field RF wireless

power system (which is showed in Figure 6.2).

From Figure 6.1, we can see that NFC communication only application consumes less than harvested power within the certain range r_x [101]. Within that range r_x, as long as the wireless power is continuously available, no duty cycle or large duty cycle is sufficient to provide enough energy for communication operation. But when the range is above r_x or the application requires much more power, a properly designed duty-cycled strategy and a larger storage media is needed.

In spite of the range, antennas' misalignment in both systems, the multi-path effect in far field system and the magnetic interference in near field significantly impact on the wireless power transfer performance. Ideally, for both systems, the duty-cycle strategy should be adaptive to change of harvested power to prevent the entire platform from brown-out, which is extremely power and time expensive. In another word, the schedule of the duty cycle should be determined by the balance of the available power and consumed power in run-time instead of a constant design given different range and relative antenna position. Therefore, the real-time measurement of harvested power level and the adjusted duty-cycle is suggested for the future wireless power application.

6.2 Far Field System and Future Work

In far-field systems, such as UHF-WISP, the power consumption of the WISP Rx(Sense WISP) and its energy harvesting efficiency during measurement are two significant factors which determine system's performance. The digital computations, such as ToA measurements, are the most power hungry processes. The relationship between power consumption, precision, range, and latency and our tested system performance are shown in Figure 6.2. If the power available to the WISP Rx(Sense WISP) increases, the overall performance of the system improves. Reducing the latency of the system would average out the measurement noise in a given period and thereby, improve precision. However, increase in detection distance would increase acoustic propagation, energy harvesting time, and the WISP inventory time, thereby increasing the latency.

Instead of using the digital method to sample sensors and backscatter measurement result digitally to the power transmitter, we can use a low power analog-backscatter method [78] to modulate the sensor data on the receiver load. It will decrease the digital process power as well as the communication payload, thereby increase the operating range and bit-rate in far field systems.

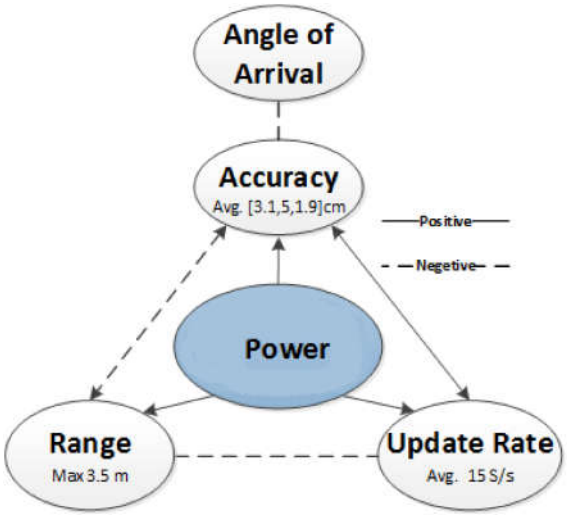

Figure 6.2: Effect of each factor in far field localization system. Solid line refers to positive correlation, dashed line refers to negative correlation.

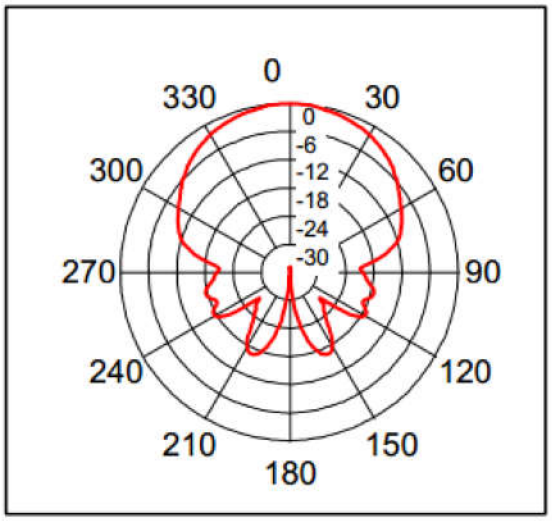

Figure 6.3: Beam angle of 25kHz ultrasonic transducer used in localization system

Firstly, analog backscatter method can improve system latency. Because the RFID EPC Gen 2 protocol we used is inherently used for polling and is highly limited in data rates. Using analog-backscatter with customized protocol can improve communication latency. In addition, by using analog backscatter, the abundant time and energy used for digital communication and computation can be saved and transfered to the power transmitter, which is typically not power and computation constrained. Besides, by using analog-backscatter, the latency of our localization system will be improved and limited by the acoustic propaga-

tion range instead of the protocol. Therefore, a multi-channel acoustic communication and detection methods, such as using wide-band acoustic frequency or code division multiplexing modulation, can be explored to achieve multi-channel distance measurement in parallel, which can further reduce the power consumption in the Sense WISP.

Other than using analog-backscatter, more accurate sensing measurement method should be explored to remove the noise of ToA measurement in order to improve sensing precision. The design of ultrasound ToA measurement should be optimized for high accuracy and lower power consumption. The low power ToA measurement method we currently use doesn't include high-speed timer and high precision hardware. In our UHF-WISP localization system, we use 32.768kHz low power clock to time the 25kHz ultrasound signal, therefore introducing average 1.5 cm distance measurement variation. This small variation can lead to large location estimation error after triangulation, because this system uses a Time-Division Multiplexing (TDM) approach for multi-channel ToA measurement, the clock variation can accumulate over time. However, there is a trade-off between obtaining high speed clock and low power cost. Therefore, instead of using digital measurement, by using analog analog-backscatter method to sense the ultrasound signals can improve the measurement accuracy and receiver power consumption, since it transfers the analogy-to-digital conversion and computation to the transmitter.

In addition, using sophisticated processing filters can be another approach to improve the system localization accuracy. The use of directional ultrasound beacon and receiver (see Figure 6.3) will introduce large non-linear noise to the ToA measurement, but isn't being modeled and filtered out by our design. Therefore, in the future, a better filter design can be explored to remove the non-linear noise if using directional sensors. One possible approach is to build a better statistic model of the non-linear noise, which is caused by angle of arrival and system noise, then uses the particle filter to improve the system accuracy. The ultrasound transducer used in this paper is relatively large, and not compatible with the thin "sticker" form factor of RFID tags. An open question is whether flat acoustic transducers, such as ultra-thin piezoelectric films or MEMS sensors, could be used to create acoustically

self-localized RFID tags with the same thin form factor as today's conventional RFID tags.

6.3 Near Field System and Future Work

This thesis describes the design and operation of the NFC-WISP which a reconfigurable platform designed to explore enhanced near-field RFID tags and applications. The platform is compatible with the ISO-14443 protocol and can communicate with wired near-field readers and NFC-enabled smartphones. Numbers of sensors have been included into the design including temperature, 3D acceleration, and rectified voltage as well as LEDs and 2M of FRAM. To the best of the author's knowledge the NFC-WISP is the first passive/semi-passive RFID tags to include an active metrics bi-stable E-ink screen that is completely powered from harvested power. Additionally, we show that the NFC-WISP can be used for cold chain monitor applications as an RFID tag logger and provide immediate temperature history to personal reading via the E-ink screen without the need for post-processing. Additionally, the use of magnetically coupled resonant wireless power transfer is demonstrated for recharging multiple NFC-WISP higher power levels.

Furthermore, this work argues that the NFC-WISP fundamentally lowers the barrier of entry to RFID research and will allow people from a wide variety of fields to develop new and innovative near-field RFID technologies. Whether it is students as part of a class project, security specialists, consumer electronics designers, or artists, it is believed that a diverse group of people will be able to push RFID technology and find new and useful usage models. The hope is that this will lead to the discovery of compelling applications and that IC tag designers will be able to draw upon the lessons learned from the NFC-WISP. As such the NFC-WISP has been open sourced and all design files, firmware and reader example code can be found online [1] or by contacting the authors.

In addition, to enable NFC-WISP to support more power hungry application, we simulated the coil design of an NFC receiver in order to optimize both its power transfer performance and bandwidth is given a particular NFC receiver model. In our analysis, we find that a 2-coil system (ideally low Q) normally has better performance at close range while a

3-coil system (two coils in Rx, one higher Q and the other lower Q) perform better at longer range; Besides, we study the influence of cross-coupling in a 3-coil system and parasitic capacitance in both 2 and 3-coil system, and propose to detune the receiver antenna in order to compensate the frequency shift caused by those parasitic effects and obtain better power delivery efficiency given particular receiver load.

Finally, we simulate and analyze the wireless power and communication performance in both 2-coil and 3-coil systems which consist of a newly developed NFC-WISP hardware and a commodity NFC-enabled smartphone. Variations of load R_L between different NFC-WISP operating modes are simulated, and a switchable receiver coil design is proposed and proven to improve both power delivery and communication performance. Finally, the use of the proposed method enables the new NFC-WISP hardware be able to operated at a longer distance (improved from $0.5cm$ to $1.5cm$) while delivering higher power (improved energy transfer capability from $8mJ$ to $16mJ$).

In a nutshell, in near field system, the range between the wireless power source (here refers to the NFC reader) and the tag(here refers to NFC- WISP) is around a few cm. Traditional low Q 2-coil system with single receiver coil will result in higher PDL as the range r decreases. 3-coil system with one high Q and one lower Q receiver coils can be tuned to deliver more power at a longer distance. Both these systems suffer from frequency shifting introduced by parasitic capacitance and cross coupling effect as the decrease of r. The higher Q 3-coil system typically can provide higher PDL and is less sensitive to the change of receiver load impedance compared to the lower Q 2-coil system. The lower Q 2-coil system generally can provide better communication performance and is less sensitive to the change of relative antenna position compared to the higher Q 3-coil system. The power and communication optimization of NFC wireless power systems vary with different applications in practice. The Different application can limit the design of load impedance, source impedance and antenna Q. Adaptively switching between low Q 2-coil and high Q 3-coil configuration can change the system coupling Q for achieving high PDL and robust communication simultaneously during NFC-WISP operation in run-time. But in general the maximum power can be received by

any receiver will roughly drop at a rate of $\frac{1}{r^3}$ ($r = Range$) along with the increase of the range.

It is obvious that the frequency shifting results in a big challenge in the near-field wireless power system. Ideally, the future design of near-field wireless power system use adaptive matching network to compensate the change of the resonate frequency, load impedance and relative antenna position in order obtain maximize power and communication performance. In addition, the proper choice and design of the matching network are critical for the system optimization.

BIBLIOGRAPHY

[1] http://nfc-wisp.wikispaces.com/.

[2] http://nfc-wisp.wikispaces.com/.

[3] http://www.link-labs.com/zigbee-vs-bluetooth/.

[4] NFC Critical Link for Internet of Things. `https://nxp-rfid.com/products/ntag/ntag-i2c-benefits/`.

[5] Tire pressure and brake temperature systems smartstem.

[6] *WikipediaISO/IEC 14443*.

[7] Syed Ahson and Mohammad Ilyas. *RFID handbook : applications, technology, security, and privacy*. Boca Raton: CRC Press, 2008.

[8] AMS. *AS3953A: 14443 High Speed Passive Tag Interface*, June 2012.

[9] AMS. *AS3953A: 14443 High Speed Passive Tag Interface*, June 2012.

[10] Daniel Arnitz, Klaus Witrisal, and Ulrich Muehlmann. Multifrequency continuous-wave radar approach to ranging in passive uhf rfid. *Microwave Theory and Techniques, IEEE Transactions on*, 57(5):1398–1405, 2009.

[11] Daniel Arnitz, Klaus Witrisal, and Ulrich Muehlmann. Multifrequency continuous-wave radar approach to ranging in passive uhf rfid. *Microwave Theory and Techniques, IEEE Transactions on*, 57(5):1398–1405, 2009.

[12] Darmindra D Arumugam, Joshua D Griffin, and Daniel D Stancil. Experimental demonstration of complex image theory and application to position measurement. *Antennas and Wireless Propagation Letters, IEEE*, 10:282–285, 2011.

[13] Darmindra D Arumugam, Joshua D Griffin, and Daniel D Stancil. Experimental demonstration of complex image theory and application to position measurement. *Antennas and Wireless Propagation Letters, IEEE*, 10:282–285, 2011.

[14] CG Begley and L Ellis. Drug development: Raise standards for preclinical cancer research. *Nature*, 483:531533, 2012.

[15] Mathieu Bouet and Aldri L Dos Santos. Rfid tags: Positioning principles and localization techniques. In *Wireless Days, 2008. WD'08. 1st IFIP*, pages 1–5. IEEE, 2008.

[16] G. Broll, E. Rukzio, M. Paolucci, M. Wagner, A. Schmidt, and H. Hussmann. Perci: Pervasive service interaction with the internet of things. *Internet Computing, IEEE*, 13(6):74–81, Nov 2009.

[17] Michael Carter, Joseph Stetter, Joshua Smith, Aaron Parks, Y Zhao, Melvin Findlay, and Vinay Patel. Printed low power amperometric gas sensors employing rf energy harvesting. In *Meeting Abstracts*, number 44, pages 1602–1602. The Electrochemical Society, 2012.

[18] Byoung-Suk Choi, Joon-Woo Lee, Ju-Jang Lee, and Kyoung-Taik Park. A hierarchical algorithm for indoor mobile robot localization using rfid sensor fusion. *Industrial Electronics, IEEE Transactions on*, 58(6):2226–2235, 2011.

[19] Byoung-Suk Choi, Joon-Woo Lee, Ju-Jang Lee, and Kyoung-Taik Park. A hierarchical algorithm for indoor mobile robot localization using rfid sensor fusion. *Industrial Electronics, IEEE Transactions on*, 58(6):2226–2235, 2011.

[20] A. Christ, M.G. Douglas, J.M. Roman, E.B. Cooper, A.P. Sample, B.H. Waters, J.R. Smith, and N. Kuster. Evaluation of wireless resonant power transfer systems with human electromagnetic exposure limits. *Electromagnetic Compatibility, IEEE Transactions on*, 55(2):265–274, April 2013.

[21] A. Christ, M.G. Douglas, J.M. Roman, E.B. Cooper, A.P. Sample, B.H. Waters, J.R. Smith, and N. Kuster. Evaluation of wireless resonant power transfer systems with human electromagnetic exposure limits. *Electromagnetic Compatibility, IEEE Transactions on*, 55(2):265–274, April 2013.

[22] M. Darianian and M.P. Michael. Smart home mobile rfid-based internet-of-things systems and services. In *Advanced Computer Theory and Engineering, 2008. ICACTE '08. International Conference on*, pages 116–120, Dec 2008.

[23] A.D. Dehennis, M. Mailand, D. Grice, S. Getzlaff, and A.E. Colvin. A near-field-communication (nfc) enabled wireless fluorimeter for fully implantable biosensing applications. In *Solid-State Circuits Conference Digest of Technical Papers (ISSCC), 2013 IEEE International*, pages 298–299, Feb 2013.

[24] A.D. Dehennis, M. Mailand, D. Grice, S. Getzlaff, and A.E. Colvin. A near-field-communication (nfc) enabled wireless fluorimeter for fully implantable biosensing applications. In *Solid-State Circuits Conference Digest of Technical Papers (ISSCC), 2013 IEEE International*, pages 298–299, Feb 2013.

[25] Jean-Jacques DeLisle. NFC Prepares For Wide Adoption. `http://mwrf.com/active-components/nfc-prepares-wide-adoption`.

[26] Artem Dementyev, Jeremy Gummeson, Derek Thrasher, Aaron Parks, Deepak Ganesan, Joshua R Smith, and Alanson P Sample. Wirelessly powered bistable display tags. In *Proceedings of the 2013 ACM international joint conference on Pervasive and ubiquitous computing*, pages 383–386. ACM, 2013.

[27] Federal Communication Commission (FCC). Title 47: Telecommunication. January, 31 2011.

[28] Federal Communication Commission (FCC). Title 47: Telecommunication. January, 31 2011.

[29] Federal Communication Commission (FCC). Title 47: Telecommunication, part 15: Radio frequency devices. January, 31 2011.

[30] Federal Communication Commission (FCC). Title 47: Telecommunication, part 15: Radio frequency devices. January, 31 2011.

[31] Federal Communication Commission (FCC). Title 47: Telecommunication, part 18: Industrial, scientific, and medical equipment. January, 31 2011.

[32] Federal Communication Commission (FCC). Title 47: Telecommunication, part 18: Industrial, scientific, and medical equipment. January, 31 2011.

[33] E. Freudenthal, D. Herrera, F. Kautz, C. Natividad, A. Ogrey, J. Sipla, A. Sosa, C. Betancourt, and L. Estevez. Suitability of nfc for medical device communication and power delivery. In *Engineering in Medicine and Biology Workshop, 2007 IEEE Dallas*, pages 51–54, Nov 2007.

[34] E. Freudenthal, D. Herrera, F. Kautz, C. Natividad, A. Ogrey, J. Sipla, A. Sosa, C. Betancourt, and L. Estevez. Suitability of nfc for medical device communication and power delivery. In *Engineering in Medicine and Biology Workshop, 2007 IEEE Dallas*, pages 51–54, Nov 2007.

[35] Adnan Harb. Energy harvesting: State-of-the-art. *Renewable Energy*, 36(10):2641–2654, 2011.

[36] iki, January 2015.

[37] Morris Kesler. Highly resonant wireless power transfer: safe, efficient, and over distance. *WiTricity Corporation*, pages 1–32, 2013.

[38] Mehdi Kiani, Uei-Ming Jow, and Maysam Ghovanloo. Design and optimization of a 3-coil inductive link for efficient wireless power transmission. *Biomedical Circuits and Systems, IEEE Transactions on*, 5(6):579–591, 2011.

[39] Jin-Shyan Lee, Yu-Wei Su, and Chung-Chou Shen. A comparative study of wireless protocols: Bluetooth, uwb, zigbee, and wi-fi. In *Industrial Electronics Society, 2007. IECON 2007. 33rd Annual Conference of the IEEE*, pages 46–51. IEEE, 2007.

[40] Nicolai Marquardt, Alex S. Taylor, Nicolas Villar, and Saul Greenberg. Rethinking rfid: Awareness and control for interaction with rfid systems. In *Proceedings of the SIGCHI Conference on Human Factors in Computing Systems*, CHI '10, pages 2307–2316, New York, NY, USA, 2010. ACM.

[41] Saman Naderiparizi, Yi Zhao, James Youngquist, Alanson P Sample, and Joshua R Smith. Self-localizing battery-free cameras. In *Proceedings of the 2015 ACM International Joint Conference on Pervasive and Ubiquitous Computing*, pages 445–449. ACM, 2015.

[42] Lionel M Ni, Yunhao Liu, Yiu Cho Lau, and Abhishek P Patil. Landmarc: indoor location sensing using active rfid. *Wireless networks*, 10(6):701–710, 2004.

[43] Lionel M Ni, Yunhao Liu, Yiu Cho Lau, and Abhishek P Patil. Landmarc: indoor location sensing using active rfid. *Wireless networks*, 10(6):701–710, 2004.

[44] Pavel V Nikitin, Rene Martinez, Shashi Ramamurthy, Hunter Leland, Gary Spiess, and KVS Rao. Phase based spatial identification of uhf rfid tags. In *RFID, 2010 IEEE International Conference on*, pages 102–109. IEEE, 2010.

[45] Pavel V Nikitin, Rene Martinez, Shashi Ramamurthy, Hunter Leland, Gary Spiess, and KVS Rao. Phase based spatial identification of uhf rfid tags. In *RFID, 2010 IEEE International Conference on*, pages 102–109. IEEE, 2010.

[46] Aaron N Parks, Alanson P Sample, Yi Zhao, and Joshua R Smith. A wireless sensing platform utilizing ambient rf energy. In *Biomedical Wireless Technologies, Networks, and Sensing Systems (BioWireleSS), 2013 IEEE Topical Conference on*, pages 154–156. IEEE, 2013.

[47] Matthai Philipose, Joshua R Smith, Bing Jiang, Alexander Mamishev, Sumit Roy, and Kishore Sundara-Rajan. Battery-free wireless identification and sensing. *Pervasive Computing, IEEE*, 4(1):37–45, 2005.

[48] Nissanka B Priyantha, Anit Chakraborty, and Hari Balakrishnan. The cricket location-support system. In *Proceedings of the 6th annual international conference on Mobile computing and networking*, pages 32–43. ACM, 2000.

[49] Nissanka B Priyantha, Anit Chakraborty, and Hari Balakrishnan. The cricket location-support system. In *Proceedings of the 6th annual international conference on Mobile computing and networking*, pages 32–43. ACM, 2000.

[50] Mohammed Ziaur Rahman and Lindsay Kleeman. Paired measurement localization: a robust approach for wireless localization. *Mobile Computing, IEEE Transactions on*, 8(8):1087–1102, 2009.

[51] Ben Ransford. Python client for LLRP-based RFID readers. `https://github.com/ransford`.

[52] MM Saad, Chris J Bleakley, T Ballal, and Simon Dobson. High-accuracy reference-free ultrasonic location estimation. *Instrumentation and Measurement, IEEE Transactions on*, 61(6):1561–1570, 2012.

[53] MM Saad, Chris J Bleakley, T Ballal, and Simon Dobson. High-accuracy reference-free ultrasonic location estimation. *Instrumentation and Measurement, IEEE Transactions on*, 61(6):1561–1570, 2012.

[54] Alanson P Sample, Craig Macomber, Liang-Ting Jiang, and Joshua R Smith. Optical localization of passive uhf rfid tags with integrated leds. In *RFID (RFID), 2012 IEEE International Conference on*, pages 116–123. IEEE, 2012.

[55] Alanson P Sample, Craig Macomber, Liang-Ting Jiang, and Joshua R Smith. Optical localization of passive uhf rfid tags with integrated leds. In *RFID (RFID), 2012 IEEE International Conference on*, pages 116–123. IEEE, 2012.

[56] Alanson P Sample, David A Meyer, and Joshua R Smith. Analysis, experimental results, and range adaptation of magnetically coupled resonators for wireless power transfer. *Industrial Electronics, IEEE Transactions on*, 58(2):544–554, 2011.

[57] Alanson P Sample, David A Meyer, Joshua R Smith, et al. Analysis, experimental results, and range adaptation of magnetically coupled resonators for wireless power transfer. *IEEE Transactions on Industrial Electronics*, 58(2):544–554, 2011.

[58] Alanson P Sample, Daniel J Yeager, Pauline S Powledge, Alexander V Mamishev, and Joshua R Smith. Design of an rfid-based battery-free programmable sensing platform. *Instrumentation and Measurement, IEEE Transactions on*, 57(11):2608–2615, 2008.

[59] Alanson P Sample, Daniel J Yeager, Pauline S Powledge, Alexander V Mamishev, and Joshua R Smith. Design of an rfid-based battery-free programmable sensing platform. *Instrumentation and Measurement, IEEE Transactions on*, 57(11):2608–2615, 2008.

[60] Alanson P Sample, Daniel J Yeager, Pauline S Powledge, Alexander V Mamishev, and Joshua R Smith. Design of an rfid-based battery-free programmable sensing platform. *Instrumentation and Measurement, IEEE Transactions on*, 57(11):2608–2615, 2008.

[61] Alanson P Sample, Daniel J Yeager, and Joshua R Smith. A capacitive touch interface for passive rfid tags. In *RFID, 2009 IEEE International Conference on*, pages 103–109. IEEE, 2009.

[62] Alanson P Sample, Daniel J Yeager, and Joshua R Smith. A capacitive touch interface for passive rfid tags. In *RFID, 2009 IEEE International Conference on*, pages 103–109. IEEE, 2009.

[63] A.P. Sample, J. Braun, A. Parks, and J.R. Smith. Photovoltaic enhanced uhf rfid tag antennas for dual purpose energy harvesting. In *RFID (RFID), 2011 IEEE International Conference on*, pages 146–153, April 2011.

[64] A.P. Sample, D.A. Meyer, and J.R. Smith. Analysis, experimental results, and range adaptation of magnetically coupled resonators for wireless power transfer. *Industrial Electronics, IEEE Transactions on*, 58(2):544 –554, February 2011.

[65] A.P. Sample, B.H. Waters, S.T. Wisdom, and J.R. Smith. Enabling seamless wireless power delivery in dynamic environments. *Proceedings of the IEEE*, 101(6):1343–1358, June 2013.

[66] A.P. Sample, B.H. Waters, S.T. Wisdom, and J.R. Smith. Enabling seamless wireless power delivery in dynamic environments. *Proceedings of the IEEE*, 101(6):1343–1358, June 2013.

[67] A.P. Sample, D.J. Yeager, P.S. Powledge, A.V. Mamishev, and J.R. Smith. Design of an rfid-based battery-free programmable sensing platform. *Instrumentation and Measurement, IEEE Transactions on*, 57(11):2608–2615, Nov. 2008.

[68] T Sanpechuda and L Kovavisaruch. A review of rfid localization: Applications and techniques. In *Electrical Engineering/Electronics, Computer, Telecommunications and Information Technology, 2008. ECTI-CON 2008. 5th International Conference on*, volume 2, pages 769–772. IEEE, 2008.

[69] T Sanpechuda and L Kovavisaruch. A review of rfid localization: Applications and techniques. In *Electrical Engineering/Electronics, Computer, Telecommunications and Information Technology, 2008. ECTI-CON 2008. 5th International Conference on*, volume 2, pages 769–772. IEEE, 2008.

[70] STMicroelectronics. *M24LR04E-R: 4-Kbit Dynamic NFC/RFID tag with password protection, energy harvesting and RF status functions*, June 2013.

[71] STMicroelectronics. *M24LR04E-R: 4-Kbit Dynamic NFC/RFID tag with password protection, energy harvesting and RF status functions*, June 2013.

[72] STMicroelectronics. *M24LR64-R: 64-Kbit Dynamic NFC/RFID tag with password protection*, July 2013.

[73] STMicroelectronics. *M24LR64-R: 64-Kbit Dynamic NFC/RFID tag with password protection*, July 2013.

[74] STMicroelectronics. *M24SR04: 4-Kbit Dynamic NFC / RFID tag with NFC Forum Tag Type 4 and I2C interface*, November 2014.

[75] STMicroelectronics. *M24SR04: 4-Kbit Dynamic NFC / RFID tag with NFC Forum Tag Type 4 and I2C interface*, November 2014.

[76] Berndie Strassner and Kai Chang. Passive 5.8-ghz radio-frequency identification tag for monitoring oil drill pipe. *IEEE Transactions on Microwave Theory and Techniques*, 51(2):356–363, 2003.

[77] Vamsi Talla, Bryce Kellogg, Benjamin Ransford, Saman Naderiparizi, Shyamnath Gollakota, and Joshua R Smith. Powering the next billion devices with wi-fi. *arXiv preprint arXiv:1505.06815*, 2015.

[78] Vamsi Talla and Joshua R. Smith. Hybrid Analog-Digital backscatter: A new approach for Battery-Free sensing. In *2013 IEEE International Conference on RFID (IEEE RFID 2013)*, Orlando, Florida, USA, April 2013.

[79] Vamsi Talla and Joshua R. Smith. Hybrid Analog-Digital backscatter: A new approach for Battery-Free sensing. In *2013 IEEE International Conference on RFID (IEEE RFID 2013)*, Orlando, Florida, USA, April 2013.

[80] Jorge Torres-Solis, Tiago H Falk, and Tom Chau. A review of indoor localization technologies: towards navigational assistance for topographical disorientation. *Ambient Intelligence*, pages 51–84, 2010.

[81] F Viani, P Rocca, G Oliveri, Daniele Trinchero, and A Massa. Localization, tracking, and imaging of targets in wireless sensor networks: An invited review. *Radio Science*, 46(5), 2011.

[82] Paul Viola and Michael Jones. Rapid object detection using a boosted cascade of simple features. In *Computer Vision and Pattern Recognition, 2001. CVPR 2001. Proceedings of the 2001 IEEE Computer Society Conference on*, volume 1, pages I–511. IEEE, 2001.

[83] Jue Wang and Dina Katabi. Dude, where's my card?: Rfid positioning that works with multipath and non-line of sight. In *ACM SIGCOMM Computer Communication Review*, volume 43, pages 51–62. ACM, 2013.

[84] Roy Want. An introduction to rfid technology. *IEEE Pervasive Computing*, 5(1):25–33, 2006.

[85] Roy Want, Andy Hopper, Veronica Falcao, and Jonathan Gibbons. The active badge location system. *ACM Transactions on Information Systems (TOIS)*, 10(1):91–102, 1992.

[86] Benjamin H Waters, Peter R Fidelman, Jeffrey D Raines, and Joshua R Smith. Simultaneously tuning and powering multiple wirelessly powered devices. In *Wireless Power Transfer Conference (WPTC), 2015 IEEE*, pages 1–4. IEEE, 2015.

[87] Benjamin H Waters, Peter R Fidelman, Jeffrey D Raines, and Joshua R Smith. Simultaneously tuning and powering multiple wirelessly powered devices. In *Wireless Power Transfer Conference (WPTC), 2015 IEEE*, pages 1–4. IEEE, 2015.

[88] Benjamin H Waters, Alanson P Sample, and Joshua R Smith. Adaptive impedance matching for magnetically coupled resonators. In *Proceedings of the PIERS*, pages 694–701. Citeseer, 2012.

[89] Wikipedia. Internet of things — wikipedia, the free encyclopedia, 2015. [Online; accessed 28-April-2015].

[90] Wikipedia. Near field communication — wikipedia, the free encyclopedia, 2015. [Online; accessed 11-May-2015].

[91] Wikipedia. Radio-frequency identification — wikipedia, the free encyclopedia, 2015. [Online; accessed 11-May-2015].

[92] Daniel J Yeager, Alanson P Sample, Joshua R Smith, and Joshua R Smith. Wisp: A passively powered uhf rfid tag with sensing and computation. *RFID Handbook: Applications, Technology, Security, and Privacy*, pages 261–278, 2008.

[93] D.J. Yeager, P.S. Powledge, R. Prasad, D. Wetherall, and J.R. Smith. Wirelessly-charged uhf tags for sensor data collection. In *RFID, 2008 IEEE International Conference on*, pages 320 –327, april 2008.

[94] Alper Yilmaz, Omar Javed, and Mubarak Shah. Object tracking: A survey. *Acm computing surveys (CSUR)*, 38(4):13, 2006.

[95] Da Zhang, Feng Xia, Zhuo Yang, Lin Yao, and Wenhong Zhao. Localization technologies for indoor human tracking. In *Future Information Technology (FutureTech), 2010 5th International Conference on*, pages 1–6. IEEE, 2010.

[96] Da Zhang, Feng Xia, Zhuo Yang, Lin Yao, and Wenhong Zhao. Localization technologies for indoor human tracking. In *Future Information Technology (FutureTech), 2010 5th International Conference on*, pages 1–6. IEEE, 2010.

[97] Yi Zhao, Anthony LaMarca, and Joshua R Smith. A battery-free object localization and motion sensing platform. In *Proceedings of the 2014 ACM International Joint Conference on Pervasive and Ubiquitous Computing*, pages 255–259. ACM, 2014.

[98] Yi Zhao, Brody Mahoney, and Joshua R Smith. Analysis of a near field communication wireless power system. In *Wireless Power Transfer Conference (WPTC), 2016 IEEE*, pages 1–4. IEEE, 2016.

[99] Yi Zhao and Joshua R Smith. A battery-free rfid-based indoor acoustic localization platform. In *RFID (RFID), 2013 IEEE International Conference on*, pages 110–117. IEEE, 2013.

[100] Yi Zhao and Joshua R Smith. A battery-free rfid-based indoor acoustic localization platform. In *RFID (RFID), 2013 IEEE International Conference on*, pages 110–117. IEEE, 2013.

[101] Yi Zhao, Joshua R Smith, and Alanson Sample. Nfc-wisp: A sensing and computationally enhanced near-field rfid platform. In *RFID (RFID), 2015 IEEE International Conference on*, pages 174–181. IEEE, 2015.

[102] Yi Zhao, Joshua R Smith, and Alanson Sample. Nfc-wisp: an open source software defined near field rfid sensing platform. In *Proceedings of the 2015 ACM International Joint Conference on Pervasive and Ubiquitous Computing and Proceedings of the 2015 ACM International Symposium on Wearable Computers*, pages 369–372. ACM, 2015.

[103] Yu Zhou. A closed-form algorithm for the least-squares trilateration problem. *Robotica*, 29(3):375–389, 2011.